Wave propagation in photonic crystals and metamaterials: surface waves, nonlinearity and chirality

by

Bingnan Wang

A dissertation submitted to the graduate faculty

in partial fulfillment of the requirements for the degree of

DOCTOR OF PHILOSOPHY

Major: Condensed Matter Physics

Program of Study Committee:
Costas M. Soukoulis, Major Professor
Rana Biswas
Marshall Luban
Gary Tuttle
Marzia Rosati

Iowa State University

Ames, Iowa

2009

Copyright © Bingnan Wang, 2009. All rights reserved.

TABLE OF CONTENTS

LIST OF FIGURES iv

ACKNOWLEDGEMENTS xii

ABSTRACT xiii

CHAPTER 1. Overview 1

1.1 Photonic crystals and metamaterials 1

1.2 Introduction to photonic crystals 2

1.2.1 A brief review 2

1.2.2 Wave propagation in photonic crystals 4

1.2.3 Band structure of our photonic crystal 7

1.3 Introduction to Metamaterials 8

1.3.1 Wave propagation in double-negative metamaterials 9

1.3.2 A brief review of metamaterials 11

1.4 Outline of the thesis 13

CHAPTER 2. Surface modes and waveguiding of photonic crystals 15

2.1 Introduction 15

2.1.1 Surface waves in photonic crystals 15

2.1.2 Line defects and waveguides in photonic crystals 18

2.2 The excitation of surface modes 19

2.2.1 ATR method 20

2.2.2 Experimental results 23

2.3 Beaming and enhance transmission through photonic crystal waveguide 25

2.3.1 Coupling to subwavelength apertures 26
2.3.2 The experimental setup 29
2.3.3 Enhanced transmission 31
2.3.4 Directed emission 34
2.4 Experimental verification of quantized optical conductance in photonic crystal waveguides 38
2.4.1 Introduction to quantized conductance 38
2.4.2 Experimental design 40
2.4.3 Results and discussion 41
2.5 Conclusion 44
CHAPTER 3. Study of nonlinear split-ring resonators 45
3.1 Introduction 45
3.2 Varactor diodes 46
3.3 Self-tuning of SRR with varactor 48
3.4 The simplified driven nonlinear resonator model 52
3.5 Nonlinear SRR with back-to-back varactors 55
3.6 Coupling between nonlinear SRRs 56
3.7 Conclusions 58
CHAPTER 4. Chiral metamaterials 59
4.1 Introduction 59
4.2 Wave propagation in chiral media 61
4.3 Effective parameter retrieval of chiral media 63
4.4 Review of work on chiral metamaterials 65
4.4.1 Theoretical studies 65
4.4.2 Experimental realizations 68
4.5 Nonplanar chiral metamaterial based on chiral SRRs 71
4.5.1 The chiral SRR design 71
4.5.2 Experimental method 73

4.5.3 Results and discussion 74
4.6 A microwave absorber made from chiral metamaterial 77
4.6.1 Loss problem and metamaterial absorbers 77
4.6.2 The chiral metamaterial absorber 79
4.6.3 Results and discussion 81
4.7 Conclusion 83
CHAPTER 5. Conclusions 85
BIBLIOGRAPHY 87

LIST OF FIGURES

Figure 1.1 The 2D photonic crystal composed of periodically arranged alumina rods. The alumina rods have square cross sections and are infinitely long in z direction. The array extends infinitely in x and y directions. . 7

Figure 1.2 The band structure of the 2D photonic crystal is shown in the main figure. The solid lines show the bands of TM polarization and the dashed lines show the bands of TE polarization. The gray area indicates the bandgap of TM polarization. The primitive cell of the reciprocal lattice is shown in the inset. Left figures indicate TM and TE polarizations and the photonic crystal structure in xy plane. 8

Figure 1.3 (a) The split-ring resonator structure. (b) The first metamaterial with negative index demonstrated by experiments [1]. 12

Figure 2.1 (a) The projected band structure of the photonic crystal. Below the figure shows the supercell and the arrow indicates that the supercell is periodic in that direction. Please see text for the parameters. (b) The projected band structure of the photonic crystal with surface modifications. The surface layer is composed of circular rods with diameter of 1.83 mm. Below the figure shows the supercell and the arrow indicates that the supercell is periodic in that direction. 17

Figure 2.2 (a) The projected band structure of the photonic crystal calculated with the supercell indicated in the inset. The arrow indicates that the supercell is periodic in that direction. (b) The projected band structure of the photonic crystal with line defect, calculated with the supercell shown in the inset. The arrow indicates that the supercell is periodic in that direction. 19

Figure 2.3 Experimental setup of the ATR measurement. The HP8510 network analyzer and a pair of horn antennas are used to measure the reflection spectrum of the prism. The photonic crystal is put behind the prism. . 20

Figure 2.4 The experiment (solid lines) and simulation (circles) results of reflection at incident angle 53° for the photonic crystal with corrugation layer of circular rods with $D = 2.44\,mm$. From top to bottom shows the reflection when the distance g of the air gap between the prism and the surface of the structure increases. 22

Figure 2.5 Experimental surface band structure of a 2D photonic crystal. Between the light gray areas exist the band gap of photonic crystal. Solid lines and square dots with error bars are supercell band structure calculation and experimental results of the surface band for (a) photonic crystal with a corrugation layer of circular rods with $D = 1.83\,mm$, (b) photonic crystal with a corrugation layer of circular rods with $D = 2.44\,mm$, (c) a single layer of rods with $D = 1.83\,mm$ and (d) a single layer of rods with $D = 2.44\,mm$. 24

Figure 2.6 The simulated electric field distribution with (a) a regular photonic crystal waveguide formed by a line defect, (b) the same waveguide as in (a) with a modified layer added and (c) the same waveguide as in (b) with a grating layer added. The dashed lines in the figures show the position of the structures. The structures are shown under the corresponding field distributions. 28

Figure 2.7 (a) The structure's details and definition of the different boundaries used. bnd0, bnd1, bnd2, bnd3 are the boundaries in the channel, at the end of the photonic crystal, in the middle of the air part and at the end of the air part respectively.(b) The shape of the surface layers in each of the fifth different structures. 30

Figure 2.8 Simulated power flow versus frequency measured at boundary bnd0 for the four structures which are only waveguide inside the photonic crystal (structure1), the waveguide with the grating layers (structure2), the waveguide with the modified layers (structure3), and the waveguide with both the modified and the grating layers (structure4). 32

Figure 2.9 Simulation and experimental power flow versus frequency for structure4, which possesses both the gratings and the modified layers. 32

Figure 2.10 Power flow versus frequency for structure4 (simulation only) and structure5 (simulation and experiment). Notice that structure5 is similar to structure4 except for the one grating missing in front and the end of the waveguide. 33

Figure 2.11 A 2d plot of the strength of the outgoing electric field for the case of structure4. (a) and (b) are the experimental and the simulation results respectively at frequency $f = 11.85$ GHz. (c) and (d) are the experimental and the simulation results respectively at frequency $f = 12.47$ GHz. 34

Figure 2.12 The line plots of field intensity for structure4 at 11.85 GHz, corresponds to the 2D distribution shown in Fig. 2.11. for (a) The field intensity along the central line of the waveguide exit (horizontal direction in Fig. 2.11(a)) for structure4 at 11.85 GHz. (b) The field intensity along the interface of the waveguide end (vertical direction in Fig. 2.11(b)), at the horizontal position indicated by the arrow in (a). The solid lines are numerical results and dashed lines are experimental results. 35

Figure 2.13 A 2d plot of the strength of the electric field for structure5. (a) and (b) are the experimental and the simulation results respectively at frequency $f = 11.85$ GHz. (c) and (d) are the experimental and the simulation results respectively at frequency $f = 12.47$ GHz. 36

Figure 2.14 Simulated 2d plot of the strength of the electric field of structure3 at (a) $f = 11.97$ GHz and (b) $f = 11.33$ GHz. 37

Figure 2.15 An illustration of the experimental setup. 41

Figure 2.16 The experimental (circles) and numerical (solid line) results of optical conductance of a photonic crystal waveguide at 10 GHz. 42

Figure 2.17 The experimental (circles) and numerical (solid line) results of optical conductance of a metal channel for TM case (E field perpendicular to the plane). 43

Figure 3.1 The schematic symbol of a varactor (left) and the equivalent circuit model of a varactor (right). 46

Figure 3.2 Characteristic curves of the varactor Skyworks SMV1231-079. (a) The capacitance of the varactor vs. the applied voltage. (b) The dissipative current vs. the applied voltage. 47

Figure 3.3 (a) The fabricated SRR is shown on left and the SRR with a varactor mounted into the gap is shown on right. (b) The loop antenna is positioned on top of the SRR and connected to the network analyzer (not shown). The reflected signal is measured by the network analyzer. . . . 48

Figure 3.4 The reflection of the SRR loaded with one varactor, measured by a loop antenna. The curves show the measurement results at input power from -15 dBm to 9 dBm in 3 dBm steps. 50

Figure 3.5 The hysteresis effect at high input power levels. The blue curves are measured for forward sweep (the source frequency of the network analyzer is scanned from low to high) and the red dashed curves are measured for reverse sweep (frequency is scanned from high to low). 51

Figure 3.6 The circuit model of the coupling between the driven loop antenna and the SRR loaded with one varactor. 52

Figure 3.7 The oscillation amplitude vs. source frequency calculated from the simplified nonlinear oscillator model. The curves from bottom to top correspond to excitation power from low to high. The blue arrow shows the jump for forward sweep of the top curve and the red arrow shows the jump for reverse sweep of the top curve. 54

Figure 3.8 The reflection of the SRR loaded with two back-to-back varactors, measured by a loop antenna. The curves show the measurement results at power levels from -14 dBm to 2 dBm, in 2 dBm steps. The inset shows the sample. 56

Figure 3.9 The reflection of (a) two linear SRRs and (b) two nonlinear SRRs at input power of -15 dBm. The legend shows the distance between the two SRRs. The distance between the first SRR and the antenna is fixed. 57

Figure 3.10 The 2d plot of the reflection of two coupled nonlinear SRRs. The x-axis shows the distance between the two SRRs and the y-axis shows the frequency. The four figures from left to right display the result at input power from -15 dBm to 0 dBm. The SRRs and the antenna are arranged such that they have the same axis and the planes of the rings are parallel to each other. The distance between the loop antenna and the first SRR is fixed and the second SRR is movable along its axis, as seen from the inset. 58

Figure 4.1 The transmission and reflection coefficients of a plane wave incident upon a chiral slab from left. 64

Figure 4.2 Different designs of chiral metamaterials. (a) The twisted “swiss roll” [2]; (b) The canonical helix [3]; (c) The chiral SRR [4]; (d) The bi-layer “swastika” [5]; (e) Dual strips with tilted bridge [6]; (f) Bi-layer rosettes [7] 66

Figure 4.3 (a) Schematic representation of one unit cell of the cross-wire structure. (b) Photograph of one side of a fabricated microwave-scale cross-wire sample. The geometry parameters are given by $a_x = a_y = 15$mm, $l = 14$ mm, $w = 1$ mm, $s = 1.6$ mm, $\phi_0 = 45°$, $\phi = 30°$. (Adapted from Ref. [8]) 70

Figure 4.4 The simulated current density distribution for the right circularly polarized EM wave at 6.5 GHz (a) and for the left circularly polarized EM wave at 7.5 GHz (b). (Adapted from Ref. [8]) 70

Figure 4.5 (a) The structure of the chiral SRR. (b) A unit cell of the 2D chiral metamaterial used in simulation. (c) The chiral SRRs are fabricated on PCBs and cut into strips (d) The strips are interlocked to form the chiral metamaterial slab. 72

Figure 4.6 The surface current distribution of the SRR near resonance. The circulating current forms a magnetic dipole, causes the opposite charge accumulation on the bottom SRR (+) and the top SRR (-) and forms an extra electric dipole (see green straight arrow). 73

Figure 4.7 The transmission and reflection coefficients of the chiral metamaterial slab is measured by a pair of horn antennas served as transmitter and receiver. The cables on the horn antennas are connected to a vector network analyzer (not shown). 74

Figure 4.8 From top to bottom, the transmission and reflection amplitudes for LCP and RCP waves, the azimuth rotation angle for linearly polarized waves, and the ellipticity. Simulation results are shown on left and experiment results are shown on right. 75

Figure 4.9 The retrieved effective parameters of the chiral metamaterial. The figures from top to bottom are the index of refraction for the two circularly polarized waves n_+ and n_-, the effective index of refraction n together with the chiral parameter κ, the effective relative permittivity ϵ and relative permeability μ. Simulation results are shown on left and experiment results are shown on right. 76

Figure 4.10 (a) The chiral metamaterial slab. (b) The fabricated microwave absorber. 80

Figure 4.11 The simulation results of absorption at different angles θ for (a) TE polarization and (b) TM polarization. Insets illustrate the two polarizations and the angle θ. 80

Figure 4.12 The experimental results of absorption at different angles θ for (a) TE polarization and (b) TM polarization. Insets illustrate the two polarizations and the angle θ. 82

ACKNOWLEDGEMENTS

I would like to take this opportunity to thank the people that helped me or inspired me through my graduate studies at Iowa State. It would be difficult to list all the great people I met here and all the details of their help to me. They made my experience at Iowa state enjoyable and I am grateful to all of them.

First of all I would like to express my gratitude to Prof. Costas M. Soukoulis. I want to thank him for advising my Ph.D. study at Iowa State University, for directing me to the field of photonic crystals and metamaterials, for guiding me through my research projects, for helping me with publications and this thesis, for the financial support through all my years at Iowa State University.

Thank Prof. Rana Biswas, Prof. Marshall Luban, Prof. Gary Tuttle and Prof. Marzia Rosati for serving in my program of study committee. The courses I have taken with Prof. Marshall Luban and Prof. Rana Biswas are very helpful to my research. Thank Prof. Gary Tuttle for offering me the opportunity to do experiments in microelectronic research center and all the help.

I thank Dr. Thomas Koschny very much for the help through out my studies, for patiently answering all my stupid questions, for all the guidance and suggestions on my research projects. I learned a lot from him. I would like to thank the peer members in our group. Thank Dr. Jiangfeng Zhou , Dr. Lei Zhang, Anan Fang and Weitao Dai for all the helpful discussions and suggestions. I wish them the best in their career.

Most importantly, I would like to thank my parents for their consistent support and love. Also I would like to express my gratitude to my fiancee Wenhong Liu. You made my years at Iowa State unforgettable.

ABSTRACT

Photonic crystals and metamaterials, both composed of artificial structures, are two interesting areas in electromagnetism and optics. New phenomena in photonic crystals and metamaterials are being discovered, including some not found in natural materials. This thesis presents my research work in the two areas.

Photonic crystals are periodically arranged artificial structures, mostly made from dielectric materials, with period on the same order of the wavelength of the working electromagnetic wave. The wave propagation in photonic crystals is determined by the Bragg scattering of the periodic structure. Photonic band-gaps can be present for a properly designed photonic crystal. Electromagnetic waves with frequency within the range of the band-gap are suppressed from propagating in the photonic crystal. With surface defects, a photonic crystal could support surface modes that are localized on the surface of the crystal, with mode frequencies within the band-gap. With line defects, a photonic crystal could allow the propagation of electromagnetic waves along the channels. The study of surface modes and waveguiding properties of a 2D photonic crystal will be presented in Chapter 1.

Metamaterials are generally composed of artificial structures with sizes one order smaller than the wavelength and can be approximated as effective media. Effective macroscopic parameters such as electric permittivity ϵ, magnetic permeability μ are used to characterize the wave propagation in metamaterials. The fundamental structures of the metamaterials affect strongly their macroscopic properties. By designing the fundamental structures of the metamaterials, the effective parameters can be tuned and different electromagnetic properties can be achieved. One important aspect of metamaterial research is to get artificial magnetism. Metallic split-ring resonators (SRRs) and variants are widely used to build magnetic meta-

materials with effective $\mu < 1$ or even $\mu < 0$. Varactor based nonlinear SRRs are built and modeled to study the nonlinearity in magnetic metamaterials and the results will be presented in Chapter 3.

Negative refractive index n is one of the major target in the research of metamaterials. Negative n can be obtained with a metamaterial with both ϵ and μ negative. As an alternative, negative index for one of the circularly polarized waves could be achieved with metamaterials having a strong chirality κ. In this case neither ϵ nor μ negative is required. My work on chiral metamaterials will be presented in Chapter 4.

CHAPTER 1. Overview

1.1 Photonic crystals and metamaterials

The discoveries in photonic crystals and metamaterials have largely broadened the vision of electromagnetism and optics. Photonic crystals and metamaterials are both composed of periodic structures and can mold the flow of electromagnetic (EM) waves in ways cannot be achieved in natural materials. New phenomena, including but not limited to negative refraction, artificial magnetism, near-field lensing and focusing, optical cloaking, have been discovered and studied.

For homogeneous materials, the elemental structures (molecules for instance) are much smaller than the propagating wavelength so that the propagating waves do not "feel" them. On the contrary, both photonic crystals and metamaterials are composed of artificial structures that are not negligible in size compared with the propagating wavelength. They are both spatially dispersive media in this sense.

Photonic crystals are generally composed of periodic arrangements of structures with different permittivity. The period of the structures a is on the same order with the wavelength of the propagating waves λ. Since the period of the structures is comparable with the wavelength, EM waves will be diffracted. Thus photonic crystals generally are not considered as effective media. Bloch waves and band structures are used to characterize the wave propagating properties. When designed properly, stop bands can exist in the band structure of a photonic crystal. EM waves within the frequency range of the stop bands become evanescent inside the photonic crystal.

Metamaterials are generally composed of artificial structures with sizes one order smaller than the wavelength ($\lambda/a \sim 10$). Although the ratio λ/a is not as large as natural materials, the

metamaterials can already be considered as effective media. The wave propagating properties of metamaterials can be characterized by effective macroscopic parameters and averaged fields. The fundamental structures of the metamaterials affect strongly the macroscopic properties. By designing the fundamental structures of the metamaterials, the effective parameters such as electric permittivity ϵ, magnetic permeability μ and chirality κ can be tuned and different EM properties can be achieved.

1.2 Introduction to photonic crystals

1.2.1 A brief review

The boost of research on photonic crystals starts from 1987, when Yablonovitch [9] and John [10] independently introduced the concept of photonic band-gap materials. Long before that, one-dimensional (1D) periodic structures have been studied. It has been discovered more than 100 year ago that 1D periodic dielectric stacks have a stop band, which is a spectral range that has high reflectivity. This feature is used to make distributed Bragg reflectors (DBRs). The term "photonic crystal" is generally referring to two-dimensional (2D) or three-dimensional (3D) periodic structures, although DBRs are sometimes called 1D photonic crystals.

Since the work of Yablonivitch [9] and John [10], more and more efforts have been put into photonic crystals by many researchers. The primary goal is to design and characterize photonic crystals with a total band-gap in 3D, where the propagation of electromagnetic wave is prohibited in all directions. In 1990, Ho *et.al.* demonstrated the existence of a full band-gap in 3D with a diamond-like periodic structure, by numerical calculations [11]. In 1991, the band-gap in 3D structures were proved by experiments in microwave regime [12]. The same phenomenon is expected to happen in optical regime for the same structure scaled down in geometry, due to the scaling law [13]. However, the diamond-like structure is too complicated for microfabrication. Later on, the Iowa State group proposed a layer-by-layer "woodpile" structure that give a 3D band-gap [14]. This structure is easier to fabricated and works over a wide range of structural parameters.

Due to the existence of band-gap in properly designed photonic crystals, many interesting

applications can be realized to manipulate the flow of electromagnetic waves and light [15]. For example, by introducing point defects in photonic crystals, high-Q cavities can be fabricated. By introducing line defects in photonic crystals, waveguides can be realized, where light is guided along the line defects. The guiding mechanism of photonic crystal waveguides is different than dielectric planar waveguides. For a dielectric waveguide, the dielectric constant of the waveguide is higher than its surrounding materials, and light is guided in the dielectric due to total internal reflection. For a photonic crystal waveguide, light is confined in the waveguide due to the fact that there exists a band-gap and light can not penetrate into the photonic crystal. The dielectric constant of the waveguide does not have to be larger than the surroundings. Actually, the waveguiding region can be lower-indexed materials including air. This is an important advantage of photonic crystal waveguides since that the propagation loss can be significantly reduced. Also, photonic crystal waveguides can bend light at sharp angles with lower loss. Photonic crystal waveguides have found applications in photonic crystal fibers and telecommunications [16]. We will discuss photonic crystal waveguides in more details in the next chapter.

Other than band-gaps, there are other intriguing features of photonic crystals that can be used to control the flow of light. Photonic crystals have rich dispersion relations, i.e., the relation between angular frequency ω of allowed modes and wavevector $\vec{k}$ is not a straight line. The equal-frequency surfaces (EFSs) of a photonic crystal are rather complicated. By definition, the group velocity of light inside a photonic crystal, $\vec{v}_g = \nabla_{\vec{k}}\omega(\vec{k})$, is perpendicular to the EFS of the photonic crystal. Depending on the dispersion relation, the direction of group velocity can be very different than the phase velocity, which is determined by wavevector $\vec{k}$. Since the group velocity governs the energy flow of light, peculiar refraction phenomena can occur at the interface between the photonic crystal and its surrounding. Negative refraction, where the energy flow is refracted to the "wrong" direction, can be realized in photonic crystals [17]. Due to the different diffraction behavior at different frequencies, superprism effect has been demonstrated, where extremely large angular dispersion can be achieved for light with different frequencies [18].

1.2.2 Wave propagation in photonic crystals

The wave propagation properties of a photonic crystal are determined by the Bragg scattering of the periodic structures and described by its photonic band structure. Starting from Maxwell's equations, the photonic band structure can be obtained by solving the eigenvalue problem.

The source-free Maxwell's equations are

$$\nabla \times \mathbf{E}(\mathbf{r}, t) = -\frac{\partial \mathbf{B}(\mathbf{r}, t)}{\partial t}, \tag{1.1}$$

$$\nabla \times \mathbf{H}(\mathbf{r}, t) = \frac{\partial \mathbf{D}(\mathbf{r}, t)}{\partial t}, \tag{1.2}$$

$$\nabla \cdot \mathbf{D}(\mathbf{r}, t) = 0, \tag{1.3}$$

$$\nabla \cdot \mathbf{B}(\mathbf{r}, t) = 0, \tag{1.4}$$

where $\mathbf{E}$ and $\mathbf{H}$ are the macroscopic electric and magnetic fields, respectively; $\mathbf{D}$ and $\mathbf{B}$ are the displacement and magnetic induction fields, respectively. All the above four field vectors are functions of both space $\mathbf{r}$ and time t.

Consider isotropic (ϵ and μ are scalars), linear (higher order responses to external fields are negligible) and non-dispersive (ϵ and μ are not functions of frequency) media, the constitutive relations can be written as

$$\mathbf{D}(\mathbf{r}, t) = \epsilon_0 \epsilon(\mathbf{r}) \mathbf{E}(\mathbf{r}, t), \tag{1.5}$$

$$\mathbf{B}(\mathbf{r}, t) = \mu_0 \mu(\mathbf{r}) \mathbf{H}(\mathbf{r}, t), \tag{1.6}$$

where ϵ_0 and μ_0 are the vacuum permittivity and permeability, respectively; $\epsilon(\mathbf{r})$ and $\mu(\mathbf{r})$ are the relative permittivity and permeability of the medium, respectively. Most materials are non-magnetic and the relative permeability $\mu(\mathbf{r}) = 1$.

Adopt the time-harmonic convention, the solutions of the electric and magnetic fields can be constructed as follows

$$\mathbf{E}(\mathbf{r}, t) = \mathbf{E}(\mathbf{r}) e^{-i\omega t}, \tag{1.7}$$

$$\mathbf{H}(\mathbf{r}, t) = \mathbf{H}(\mathbf{r}) e^{-i\omega t}, \tag{1.8}$$

where ω is the angular frequency. Then the two curl equations in the Maxwell's equations can be rewritten as

$$\nabla \times \mathbf{E}(\mathbf{r}) = i\omega\mu_0 \mathbf{H}(\mathbf{r}), \tag{1.9}$$

$$\nabla \times \mathbf{H}(\mathbf{r}) = -i\omega\epsilon_0\epsilon(\mathbf{r}).\mathbf{E}(\mathbf{r}) \tag{1.10}$$

Combining the above two equations, we can get a wave equation in the frequency domain for the magnetic field

$$\frac{1}{\epsilon(\mathbf{r})}\nabla \times \nabla \times \mathbf{E}(\mathbf{r}) = \frac{\omega^2}{c^2}\mathbf{E}(\mathbf{r}), \tag{1.11}$$

$$\nabla \times \left(\frac{1}{\epsilon(\mathbf{r})}\nabla \times \mathbf{H}(\mathbf{r})\right) = \frac{\omega^2}{c^2}\mathbf{H}(\mathbf{r}). \tag{1.12}$$

where $c = 1/\sqrt{\epsilon_0\mu_0}$ is the speed of light in vacuum. When the permittivity $\epsilon(\mathbf{r})$ is known, one of the above wave equations can be solved to obtain the electric field or the magnetic field. Then the other field vector is solved accordingly with the relations determined by the Maxwell's equations.

$$\mathbf{E}(\mathbf{r}) = \frac{i}{\omega\epsilon_0\epsilon(\mathbf{r})}\nabla \times \mathbf{H}(\mathbf{r}), \tag{1.13}$$

$$\mathbf{H}(\mathbf{r}) = -\frac{i}{\omega\mu_0}\nabla \times \mathbf{E}(\mathbf{r}). \tag{1.14}$$

For photonic crystals, the permittivity is a periodic function of space,

$$\epsilon(\mathbf{r}) = \epsilon(\mathbf{r} + \mathbf{R}), \tag{1.15}$$

where lattice vector $\mathbf{R} = \sum_{i=1}^{d} m_i \mathbf{a}_i$ is a combination of primitive lattice vectors $\mathbf{a}_i$, where $i = 1, \ldots, d$ describes the dimension. Consider an indefinitely extended photonic crystal, the lattice vector extends in d-dimensional space and m_i can be any integers.

From the Floquet-Bloch theorem, the solution of the wave equation (1.12) is of the form of a periodically modulated plane wave

$$\mathbf{H}_{n,\mathbf{k}}(\mathbf{r}) = \mathbf{u}_{n,\mathbf{k}}(\mathbf{r})e^{i\mathbf{k}\cdot\mathbf{r}}, \tag{1.16}$$

$$\mathbf{u}_{n,\mathbf{k}}(\mathbf{r}) = \mathbf{u}_{n,\mathbf{k}}(\mathbf{r} + \mathbf{R}), \tag{1.17}$$

where the subscript n is the index of the discrete solutions, $\mathbf{k}$ is the corresponding wave vector and $\mathbf{u}_{n,\mathbf{k}}(\mathbf{r})$ satisfies

$$(\nabla + i\mathbf{k}) \times \left(\frac{1}{\epsilon(\mathbf{r})} (\nabla + i\mathbf{k}) \times \mathbf{u}_{n,\mathbf{k}}(\mathbf{r}) \right) = \frac{\omega^2}{c^2} \mathbf{u}_{n,\mathbf{k}}(\mathbf{r}). \tag{1.18}$$

The corresponding eigen-frequency of the n-th eigenmodes wave vector $\mathbf{k}$ is $\omega_n(\mathbf{k})$ and is a continuous function of $\mathbf{k}$. A discrete band is the formed if we plot $\omega_n(\mathbf{k})$ versus $\mathbf{k}$. If we plot all n-th bands, a full band structure of the photonic crystal is formed and all possible eigenmodes are casted in band structure.

More importantly, we do not need to calculate the eigen-solutions of all possible wave vectors, thanks to the periodicity of structure. Denote the reciprocal lattice vector associated with the given Bravias lattice as $\mathbf{G}$, then we have $\mathbf{G} \cdot \mathbf{R} = 2m\pi$, where m is an integer. The reciprocal lattice vector $\mathbf{G}$ is a Bravias lattice too and is further described by combination of the primitive vectors $\mathbf{b}_j$ in the j-th dimension in the reciprocal space, $\mathbf{G} = \sum_{j=1}^{d} n_j \mathbf{b}_j$. The primitive vectors in the reciprocal space is connected to the primitive vectors in the real space by $\mathbf{a}_i \mathbf{b}_j = 2\pi\delta_{ij}$. The solution at $\mathbf{k}$ is identical to the solution at $\mathbf{k} + \mathbf{G}$.

$$\mathbf{H}_{n,\mathbf{k}}(\mathbf{r}) = \mathbf{H}_{n,\mathbf{k}+\mathbf{G}}(\mathbf{r}), \tag{1.19}$$

$$\omega_{n,\mathbf{k}} = \omega_{n,\mathbf{k}+\mathbf{G}}. \tag{1.20}$$

The primitive cell of the reciprocal lattice is called the first Brillouin zone. Given the above information, we then only need to calculate the eigen-solutions of $\mathbf{k}$ in the first Brillouin zone.

For simple 1D photonic crystals, the band structure can be obtained analytically. However, for 2D and 3D photonic crystals, the computation of band structures must rely on numerical tools, due to the complex photonic crystal structure. There are a number of well-developed computational methods to calculate the band structure and wave propagation in photonic crystals, including plane-wave expansion method, finite-difference time-domain method, finite-element method.

1.2.3 Band structure of our photonic crystal

Our focus will be on the surface modes and wave guiding properties of 2D photonic crystals. A 2D photonic crystal is considered to be translation invariant in the third dimension. Although 2D photonic crystals do not have a full bandgap in all directions, they have found many applications in light confinement, such as waveguides, microlasers and integrated photonic circuits [13]. The 2D photonic crystal in our study is composed of alumina rods (permittivity $\epsilon = 9.8$) of square cross section (with side length of 3.18 mm), and arranged in a square lattice (with lattice constant $a = 11$ mm). We assume the square array extends infinitely into x and y directions and the rods are infinitely long in z direction (see Fig. 1.1). The numerically computed band structure of the 2D photonic crystal is shown in Fig. 1.2. It is shown that the 2D photonic crystal has a band-gap between 9.43 and 12.78 GHz for TM polarization (electric field along the rods). In the following chapter, we study the surface modes and the wave guiding properties of the 2D photonic crystal, both for TM polarization.

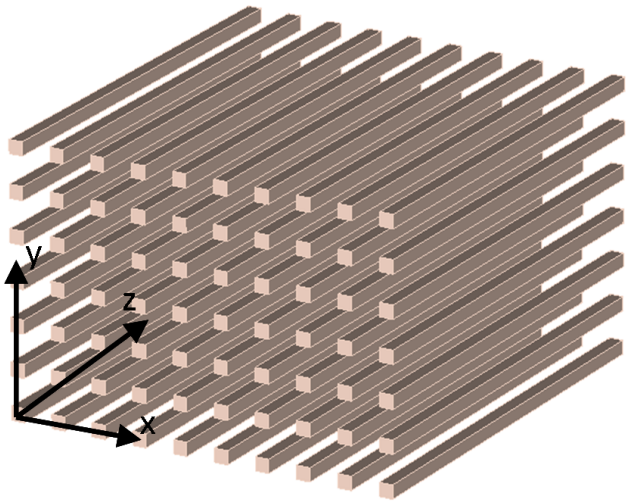

Figure 1.1 The 2D photonic crystal composed of periodically arranged alumina rods. The alumina rods have square cross sections and are infinitely long in z direction. The array extends infinitely in x and y directions.

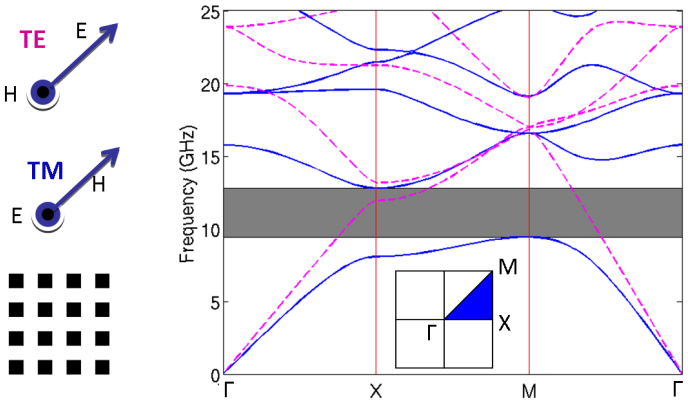

Figure 1.2 The band structure of the 2D photonic crystal is shown in the main figure. The solid lines show the bands of TM polarization and the dashed lines show the bands of TE polarization. The gray area indicates the bandgap of TM polarization. The primitive cell of the reciprocal lattice is shown in the inset. Left figures indicate TM and TE polarizations and the photonic crystal structure in xy plane.

1.3 Introduction to Metamaterials

Electromagnetic metamaterials are usually periodically arranged artificial structures that show peculiar properties, such as negative refraction, which are not seen in natural materials (for reviews of the metamaterial field, see [1,19,20]). The elemental structures of the metamaterials are typically much smaller in size relative to the wavelength such that the metamaterials can be approximated as homogeneous. Macroscopic effective parameters such as electric permittivity ϵ and magnetic permeability μ can then be used to describe the electromagnetic (EM) properties of the metamaterials [21]. The fascinating, but challenging work of scientists and engineers in this area is to design new structures, or the photonic atoms, to achieve the EM properties of metamaterials for specific applications. There are different types of metamaterials, depending on their effective parameters. When both ϵ and μ are negative, the metamaterial is called "double-negative" In this case, the effective index of refraction n is negative. When either ϵ or μ is negative but the other parameter is positive, the metamaterial is called "single-

negative". Metamaterials with small or even close to zero ϵ or μ are also interesting. When both ϵ and μ are close to zero, the metamaterial has an effective index close to zero [22].

1.3.1 Wave propagation in double-negative metamaterials

The first and the most extensively studied type of metamaterials is "double-negative" metamaterial. The work of Veselago [23] in 1958 is generally recognized as the first in this field. In his pioneer work, Veselago discussed the exotic properties of a material with both ϵ and μ negative. A "double-negative" media is interesting at first glance. Indeed, when both ϵ and μ are negative, $\epsilon\mu$ still gives a positive value. From $k^2 = \omega^2\epsilon\mu$, the wavevector k is real in this case. Thus wave propagation is permitted in a double-negative medium. It is then desirable to examine more rigorously if wave propagation in double-negative media is allowed by physics laws. It is also interesting to find the differences of EM waves in a double-negative medium and a regular (double-positive) medium.

Consider a monochromatic plane wave of the form

$$\mathbf{E}(\mathbf{r}, t) = \mathbf{E}_0 e^{i(\mathbf{k}\cdot\mathbf{r}-\omega t)} \tag{1.21}$$

$$\mathbf{H}(\mathbf{r}, t) = \mathbf{H}_0 e^{i(\mathbf{k}\cdot\mathbf{r}-\omega t)} \tag{1.22}$$

where $\mathbf{E}_0$ and $\mathbf{H}_0$ are the amplitudes of the electric and magnetic field respectively. Fit the plane wave into the Maxwell's equations (1.1)-(1.4), together with the constitutive relations (1.5)-(1.6), we come to the following relations

$$\mathbf{k} \times \mathbf{E} = \omega\mu_0\mu\mathbf{H} \tag{1.23}$$

$$\mathbf{k} \times \mathbf{H} = -\omega\epsilon_0\epsilon\mathbf{E} \tag{1.24}$$

For regular materials, $\epsilon > 0$ and $\mu > 0$, thus the triplet $\mathbf{E}$, $\mathbf{H}$ and $\mathbf{k}$ form a right-handed triad. However, for a double-negative medium, $\epsilon < 0$ and $\mu < 0$, the above relations can be rewritten as

$$\mathbf{k} \times \mathbf{E} = -\omega\mu_0|\mu|\mathbf{H} \tag{1.25}$$

$$\mathbf{k} \times \mathbf{H} = \omega\epsilon_0|\epsilon|\mathbf{E} \tag{1.26}$$

and the triplet **E**, **H** and **k** new form a left-handed triad. For this reason, Veselago [23] called a medium with both ϵ and μ negative a "left-handed" medium.

Meanwhile, the direction energy flux, is determined by the Poynting vector

$$\mathbf{S} = \mathbf{E} \times \mathbf{H} \tag{1.27}$$

and is not affected by the values of ϵ and μ. The triplet **E**, **H** and **S** always form a right-handed triad. Thus for double-negative media, the energy flux (determined by **S**) and the wavefronts (determined by **k**) move in opposite directions. The index of refraction in a double-negative medium is given by $n = -\sqrt{\epsilon\mu}$ and and has a negative value. Thus a double-negative medium is also called "negative-index" medium.

EM waves in double-negative media must not break the energy conservation law. Consider the time-averaged energy density in a non-dispersive medium is given by [24]

$$U = \frac{1}{4}\epsilon_0\epsilon|\mathbf{E}|^2 + \frac{1}{4}\mu_0\mu|\mathbf{H}|^2 \tag{1.28}$$

If a double-negative medium is non-dispersive, the energy density would be negative and is unphysical. Thus the medium must be dispersive, i.e., ϵ and μ are both functions of ω. For a quasi-monochromatic wave packet in a dispersive medium, the time-averaged energy density is given by

$$U = \frac{1}{4}\epsilon_0\frac{\partial(\epsilon\omega)}{\partial\epsilon}|\mathbf{E}|^2 + \frac{1}{4}\mu_0\frac{\partial(\mu\omega)}{\partial\mu}|\mathbf{H}|^2 \tag{1.29}$$

and the conditions $\partial(\epsilon\omega)/\partial\epsilon > 0$, and $\partial(\mu\omega)/\partial\mu > 0$, must be both satisfied. Actually when $\epsilon < 0$ and $\mu < 0$ the medium must be highly dispersive, i.e., $\partial\epsilon/\partial\omega > |\epsilon|/\omega$ and $\partial\mu/\partial\omega > |\mu|/\omega$ [25].

Most current realizations of double-negative metamaterials rely on highly resonant structures, where negative ϵ and negative μ are obtained around the corresponding resonances [19, 21]. Propagation losses of EM waves in metamaterials are inevitable. For passive media, it is required by energy conservation that the imaginary parts Im $\epsilon > 0$ and Im $\mu > 0$. Also, the values of ϵ and μ are not randomly chosen but are both limited by Kramers-Krönig relations [24].

1.3.2 A brief review of metamaterials

Veselago's left-handed medium [23] was not realized until more than three decades later, due to the lack of natural materials satisfying the parameter requirements. Negative ϵ can occur in plasmas and plasmonic materials such as noble metals for frequencies below the plasma frequency. For bulk noble metals, the plasma frequency is typically in the infrared regime. For a medium composed of thin metallic wires, the effective plasma frequency can be tuned down to microwave frequencies [26]. However, negative μ is more difficult to achieve. In natural materials, diamagnetic responses are usually weak and μ can only be slightly smaller than unity. In 1999, Pendry [21] proposed a way to achieve negative μ with a kind of artificial structures called split-ring resonators (SRRs). The SRRs are composed of metallic rings with gaps (see Fig. 1.3(a)) to behave as resonators. Although made of non-magnetic materials, the SRRs are magnetically active and can give strong responses to magnetic fields around the resonance frequency. By tuning the geometric parameters of SRRs, a band of negative μ can be obtained at the desired frequency range. If designed properly, the combination of these two sets of resonators can give both negative ϵ and negative μ in the same frequency band. This was realized with microwave experiments by Smith *et.al.* [27] in 2000. The same group further demonstrated negative refraction by measuring the output signal of EM waves refracted by a metamaterial in a wedge shape [28]. Fig. 1.3(b) shows the fabricated metamaterial composed of SRRs and metallic wires. Since then, the SRR and metallic wire structures were studied extensively by research groups all over the world, both theoretically and experimentally. Applications of metamaterials, such as super-lens [1, 29], and invisible cloak [30, 31], were proposed and studied.

By scaling down the SRR size and simplifying the structure, magnetic metamaterials were fabricated to show magnetic responses from THz to infrared region [32–35]. However, for the SRR structures, the magnetic field needs to have a component perpendicular to the plane to obtain the magnetic resonance. Normal incidence of EM waves to the planar SRR structures does not excite directly the magnetic resonance. Plus, the SRR and wire combination is too complicated to fabricate in nanoscale, especially when three-dimensional (3D) medium is

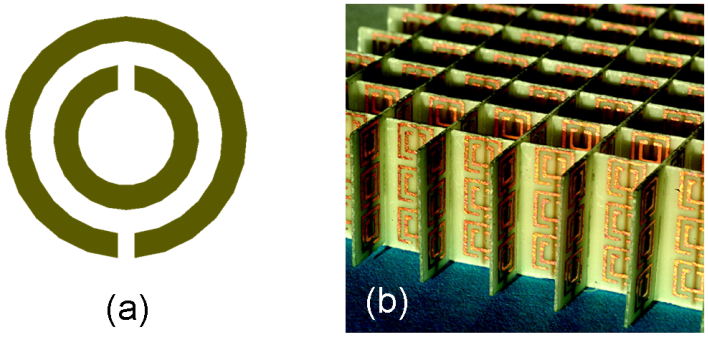

Figure 1.3 (a) The split-ring resonator structure. (b) The first metamaterial with negative index demonstrated by experiments [1].

needed.

New designs were proposed to achieve negative refraction towards the optical regime [36–39]. Unlike the SRRs, these new designs are typically double-layered metallic structures, with a dielectric substrate in the middle. The two metal layers on each side of the substrate are identical and composed of short wires, metal plates, or fishnet-like structures. While the parallel dipole resonance in each metal structure gives negative ϵ, the negative μ is provided by the anti-parallel resonance in the metal structure pairs separated by the substrate. So normal incidence of EM waves is supported. Bulk media can be fabricated by stacking the layered structures. Recently, negative refraction was demonstrated at optical frequencies with stacked fishnet-like structures [40, 41].

On the other hand, another type of metamaterials, the so-called indefinite metamaterials, has also been studied. In contrast to isotropic metamaterials, whose ϵ and μ are the same in all directions, an indefinite medium has anisotropic ϵ and μ tensors, with some components having an opposite sign to the rest. In 2001, Lindell *et.al.* [42] showed that some indefinite media can support backward waves. Smith and colleagues [43, 44] then analyzed the EM wave propagating properties of indefinite media in detail [43] and showed that some types of indefinite media can have the similar negative refraction effect as isotropic metamaterials.

Partial focusing of a point source by an indefinite medium slab was also described. The wire medium, which is composed of metal wire arrays in one direction only, is an important medium of this kind. The wire medium is anisotropic and has a negative ϵ along the direction of the wires below plasma frequency. The optical response of such a wire medium is not limited to resonances, so that the medium has a higher tolerance to fabrication defects and the loss is smaller than strongly resonant structures [45, 46]. Moreover, the wire array does not even has to be periodic. Subwavelength imaging and negative refraction of the wire medium in infrared and optical frequencies were studied theoretically and numerically [45, 46]. Recently, optical negative refraction has been demonstrated experimentally with silver nanowires [47].

1.4 Outline of the thesis

In Chapter 2, the surface waves and waveguiding properties of a 2D photonic crystal will be studied. The surface modes can be detected by attenuated total reflection (ATR) technique. The surface mode dispersion of photonic crystals with different surface defect layers will be studied experimentally. Then the photonic crystal waveguides are studied. By making use of surface modes, the waveguiding properties of photonic crystal waveguides can be improved. Enhanced transmission and directed emission can be achieved through photonic crystal waveguides of subwavelength aperture. The experimental work on optical conductance of photonic crystal waveguides will also be presented. The experimental results show that the optical conductance of photonic crystal waveguides are quantized.

The next two chapters are studies on metamaterials. In the introductions above, we have assumed that the responses of the metamaterial to EM waves are linear, i.e., effective ϵ and μ of the metamaterial do not change with the intensity of EM fields. On the other hand, it is interesting to study the transmission properties of metamaterials in nonlinear regime. One interesting idea is that, if the responses of metamaterials depends on the intensity of EM fields, the parameters ϵ/μ can then be tuned by external fields [48]. It is possible, for example, to switch μ from negative to positive in a particular frequency band thus make a double-negative metamaterial single-negative. Other phenomena in nonlinear metamaterials such as higher

harmonics generation [49], discrete breathers [50] have also been studied by other research groups. SRRs are key building blocks of metamaterials and it is thus important to study the nonlinear responses of SRRs. In Chapter 3, our study on nonlinear SRRs will be presented.

Other than double-negative metamaterials, chirality as another route to negative index of refraction has also been proposed and studied. Proposed by Pendry [2], chiral metamaterials have been shown to possess negative index for one of the circularly polarized waves. Instead of requiring both $\epsilon < 0$ and $\mu < 0$ in conventional metamaterials, chiral metamaterials need neither ϵ nor μ to be negative to get negative refractive index. The negative index in chiral metamateirals is due to the strong chirality parameter, which comes from the cross coupling between electric and magnetic fields. In Chapter 4, we will discuss the mechanism of chiral metamaterials in details. Our study on chiral metamaterials, including designs, simulations and experiments, will also be presented in Chapter 4.

CHAPTER 2. Surface modes and waveguiding of photonic crystals

Due to the existence of photonic band gaps, EM wave localization in photonic crystals can be achieved by introducing defects. Photonic crystals with proper surface defects have been shown to support surface waves, which are confined at the interfaces between photonic crystals and their surroundings. Photonic crystal waveguides can be formed by introducing line defects in photonic crystals. In this chapter, we will study the surface mode dispersion of photonic crystals with different surface defect layers. We will show that the dispersion curve of the surface modes can be traced experimentally. Then we will show that, by making use of surface modes, the waveguiding properties of photonic crystal waveguides can be modified drastically. Enhanced transmission and directed beaming can be achieved through photonic crystal waveguides of subwavelength aperture. Next we will present our experimental work on optical conductance of photonic crystal waveguides. We will show that the optical conductance of photonic crystal waveguides are quantized.

2.1 Introduction

2.1.1 Surface waves in photonic crystals

The most well-known feature of Photonic crystals (PCs) is the photonic band gap (PBG), inside which the electromagnetic waves are prohibited to propagate in all directions [15, 51]. However, when appropriately terminated, photonic crystals can support surface modes with frequencies lying inside the PBG [13]. Surface modes are easily obtained for 1D photonic crystals (stacks of alternating continuous layers) and their dispersion relation has been obtained experimentally and theoretically [52].

For a 2D photonic crystal the existence of surface waves has been shown theoretically (in

band structure calculations for semi-infinite photonic crystal) [53, 54] and experimentally by attenuated total reflection (ATR) measurements [55]. Further numerical work has shown that the existence and dispersion of surface waves at a 2D photonic crystal are very sensitive to the surface termination [54,56]. When terminated improperly, both the poor impedance matching and the interaction with surface modes can disrupt the electromagnetic wave propagation and are bad to the performance of photonic devices such as PC waveguides and PC cavities [56].

Surface waves can be helpful for certain applications when designed properly. For example, photonic crystals have been used to fabricate subwavelength imaging devices. The excitation of surface waves in this case is the key to get subwavelength resolution [57]. Recent studies also show that when the photonic crystal is appropriately periodically corrugated at the surface, enhanced transmission and beaming of light can be achieved through a photonic crystal waveguide with a subwavelength width [58–60] . This effect is due to the excitation of surface modes and constructive interference at the axis of the waveguide. It is thus important to study the dispersion relation of surface modes. In the following, we will study the surface dispersion with numerical simulations, and trace the surface band experimentally by attenuated total reflection (ATR) method.

The 2D photonic crystal we study is a square array of square alumina rods, 21 layers in x direction and 15 layers in y direction. The parameters of the rods are given in Chapter 1. With the help of the supercell technique, the band structure of the finite-size photonic crystal can be calculated using the plane wave expansion method [61]. We studied TM (electric field along the rods) modes through out the work since only TM modes can give a full band gap for a 2D photonic crystal [13]. As shown, for example, in Fig.2.1(a), the PC has a band gap indicated by the gray area. There are no modes inside the band gap and below the light line.

The uncorrugated photonic crystal does not support surface waves (in the lowest total band gap); to observe surface modes we have to corrugate the surface layer of the photonic crystal, rendering it different from the air on one side and the photonic crystal bulk on the other side. The actual shape of the corrugation layer elements is not very important. We use cylindrical rods of different diameters, but also cut semi-cylinders [55], rectangular cross-

section rods different from the ones comprising the bulk photonic crystal [62] or geometrically identical rods with different dielectric constant might be used. However, there is no guarantee to obtain surface modes for a particular surface termination; the surface layer parameters have to be chosen carefully for the corrugated PC to support surface modes in the band gap of the bulk photonic crystal. In order to support surface modes, we add a new layer at the surface

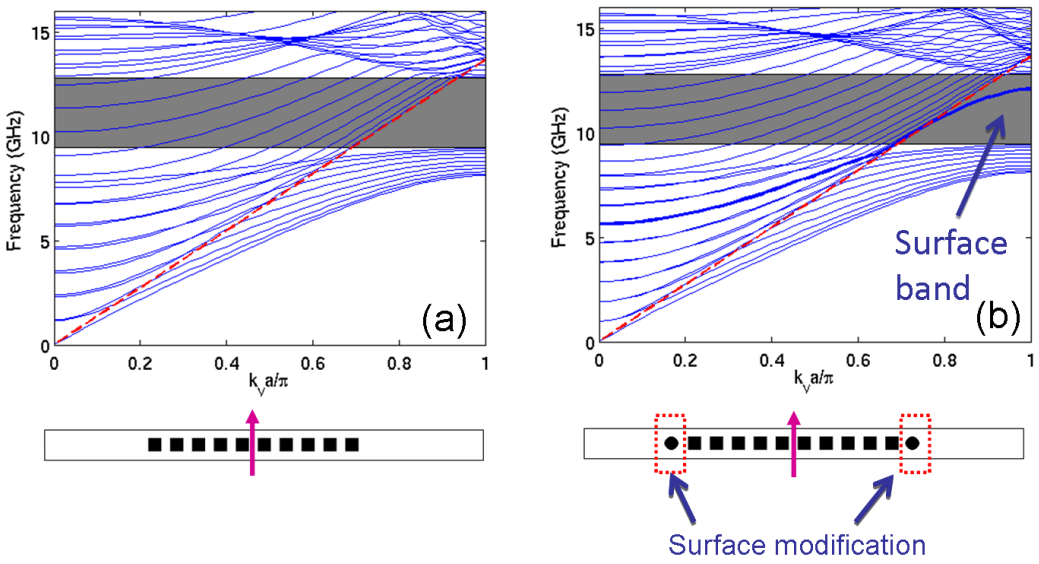

Figure 2.1 (a) The projected band structure of the photonic crystal. Below the figure shows the supercell and the arrow indicates that the supercell is periodic in that direction. Please see text for the parameters. (b) The projected band structure of the photonic crystal with surface modifications. The surface layer is composed of circular rods with diameter of 1.83 mm. Below the figure shows the supercell and the arrow indicates that the supercell is periodic in that direction.

of the photonic crystal with circular alumina rods as a periodic corrugation (Fig. 2.3). The band structure of the corrugated PC was calculated using the plane wave expansion and the supercell technique. Fig. 2.1(b) shows the calculated band structure of the photonic crystal with surface rods of diameter 1.83 mm. It is clearly shown in the figure that a new band is enabled, which lies inside the bandgap and under the light line. Modes in this band can neither

penetrate into the photonic crystal nor propagate into the air. Thus these modes are bounded to the surface region of the photonic crystal and are called surface modes.

2.1.2 Line defects and waveguides in photonic crystals

A line defect in a photonic crystal can be created for example by changing the geometry or remove one row of the structures. In this case, a defect in an otherwise perfect periodicity is created and the translational symmetry is destroyed. Eigenmodes can be created in the frequency range of the bandgap. These new eigenmodes allow the propagation of EM waves inside the defect region. Meanwhile, the EM waves are still prohibited from propagating inside the bulk photonic crystal, since the frequencies are inside the bandgap. Thus the EM waves are confined in the defect region. So a waveguide is created in this way.

Photonic crystal waveguides guide EM waves in a mechanism different than traditional dielectric waveguides and have certain advantages over the latter [13]. Traditional dielectric waveguides guide EM waves based on total internal reflection. The dielectric constant of the waveguide must be higher than the surroundings. Propagation loss is inevitable since the EM waves are propagating inside the higher dielectric region. Also, there will be significant loss when the waveguide is bent since the waveguiding mechanism requires a large incident angle to get total internal reflection. It is difficult to bend the EM wave in a sharp angle by a dielectric waveguide. Photonic crystal waveguides on the other hand guide EM waves based on photonic bandgaps. The EM waves are confined in the defect region and higher dielectric constant is not required. It is thus possible to guide the EM waves inside a lower dielectric region or even air. Lower propagation loss can thus be achieved with photonic crystal waveguides. Another merit of photonic crystal waveguides is that sharp bending can be created with relatively high transmission and low scattering loss. Photonic crystal waveguides have found applications in photonic crystal fibers and integrated photonic circuits [16]. The dispersion of the waveguide modes depends on how the defect is constructed. There could also be single-mode and multi-mode waveguides. In our 2D photonic crystal, a waveguide is created by removing one row of the dielectric rods. The dispersion of the waveguide modes can be computed by numerical

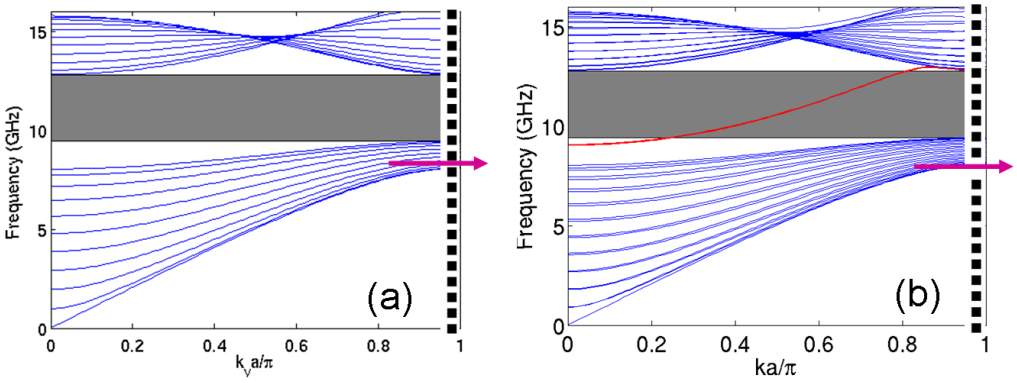

Figure 2.2 (a) The projected band structure of the photonic crystal calculated with the supercell indicated in the inset. The arrow indicates that the supercell is periodic in that direction. (b) The projected band structure of the photonic crystal with line defect, calculated with the supercell shown in the inset. The arrow indicates that the supercell is periodic in that direction.

tools. For comparison, Fig. 2.2(a) shows the projected band structure of the photonic crystal calculated with the supercell indicated in the inset. The photonic crystal is finite in the vertical direction but extends infinitely in the horizontal direction, indicated by the arrow in Fig. 2.2(a). It is clear that no mode is allowed in the bandgap region. Fig. 2.2(b) shows the band structure of the photonic crystal with the central row of rods removed, as shown in the inset. It is seen that a new band is allowed, which is located inside the bandgap. Modes in this band can not penetrate into the bulk photonic crystal since their frequencies are within the bandgap. Thus these modes are confined in the line defect region and are called waveguide modes.

2.2 The excitation of surface modes

In this section, we study experimentally and numerically the dispersion relation of surface modes for different surface corrugations that support surface waves. In contrast to previous work, we determine experimentally the complete dispersion relation of the surface modes within the photonic band gap of the photonic crystal [63].

2.2.1 ATR method

Since surface modes lies to the right of the light line, they cannot be excited by propagating waves directly. To observe a surface mode experimentally, we use the ATR method (Otto configuration) [64].

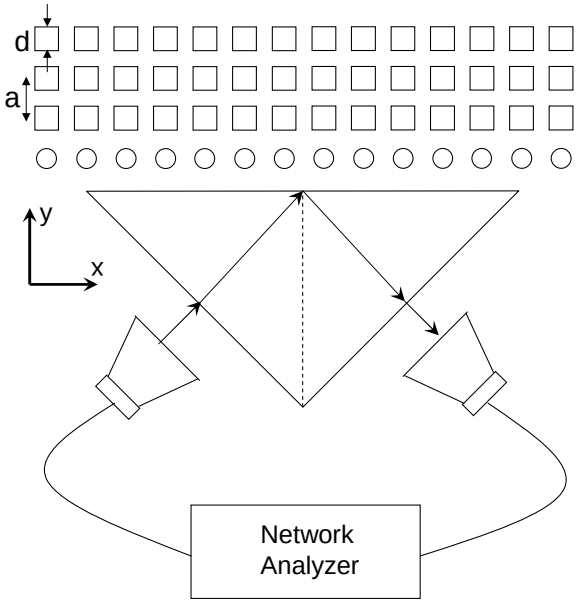

Figure 2.3 Experimental setup of the ATR measurement. The HP8510 network analyzer and a pair of horn antennas are used to measure the reflection spectrum of the prism. The photonic crystal is put behind the prism.

Consider a dielectric prism with index of refraction n. If the incident angle θ at the reflecting surface is larger than the critical angle θ_C, $\theta > \theta_C = \sin^{-1}(1/n)$, total internal reflection occurs at the outgoing interface. When there is nothing behind, the incident wave would be totally reflected. However, apart from the reflected wave, total reflection also involves a transmitted evanescent wave which travels along the interface and decays exponentially away from the surface. That is because the wavevector component parallel to the interface,

$$k_x = k \sin\theta = n\omega \sin\theta / c > \omega / c, \tag{2.1}$$

is conserved across the interface. So outside the prism, the wavevector component perpendicular to surface, k_y, is imaginary. When we put the corrugated photonic crystal close to the prism, the tail of this evanescent wave may couple to a surface mode at the surface of the photonic crystal. By changing the incident angle, we can change the value of k_x and get coupling with different surface modes. When the evanescent wave is coupled to a surface mode, there is strong field at the surface and the energy is dissipated through the coupling. Thus the reflected field intensity is smaller when the coupling happens. If the reflection spectrum is plotted, there would be a dip at the coupling frequency. The excited surface mode is then identified. By changing the incident angle, the wavevector of the evanescent wave is changed and a new surface mode could be excited if the wavevector is matched. By plotting the experimental results at different incident angles, the surface band can be obtained.

The first ATR experiment on surface modes of photonic crystal was reported more than 10 years ago [55]. However, it was not straightforward to see the coupling of surface waves from the experimental data and a dispersion relation was not obtained experimentally. In our experiment, an HP-8510 network analyzer was used to measure the S parameters so that the reflection spectrum can be immediately seen. A pair of horn antennas serves as transmitter and receiver (Fig. 2.3). The dielectric prism used in our experiments is an isosceles-right-triangle-shaped wedge with side length of $15\,cm$ and with index of refraction $n = 1.61$. The horn antennas were placed in such a way that the E field is polarized along the dielectric rods. For a given incident angle, Snell's law was used to identify the angle and position of the horn antennas such that the setup is symmetric along the dashed line.

The ATR method requires the structure to be set close to the prism to get good coupling effect because the evanescent waves decay fast; however, while we are making use of the prism, the prism itself modifies the surface modes especially when it is very close to the structure. To get a satisfying experimental result, we need to optimize the airgap size to be able to record the mode while keeping the structure as far away from the prism as possible. In Fig. 2.4 the solid curves show the coupling effect at different air gap sizes at incident angle 53° for the photonic crystal with corrugation layer of circular rods with diameter $D = 2.44\,mm$. You can

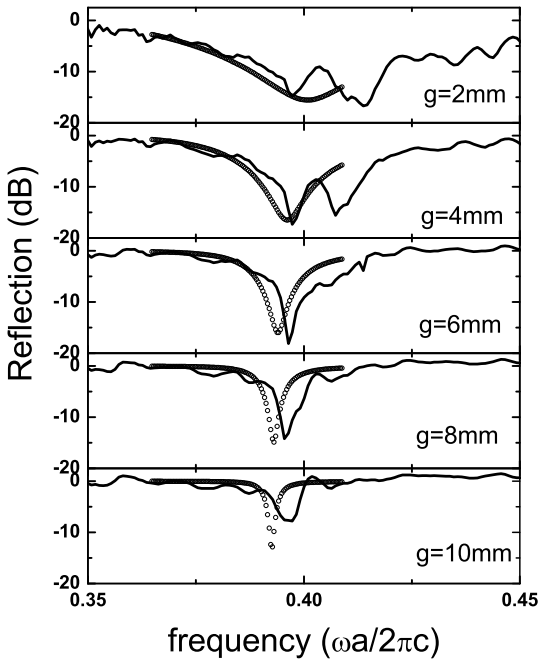

Figure 2.4 The experiment (solid lines) and simulation (circles) results of reflection at incident angle 53° for the photonic crystal with corrugation layer of circular rods with $D = 2.44\,mm$. From top to bottom shows the reflection when the distance g of the air gap between the prism and the surface of the structure increases.

see clearly in Fig. 2.4 that when the surface waves are excited, there is a very well defined dip in the reflection data. This is well shown for the distance of $g = 10\,mm$. The prism disturbs the coupling and the observed reflection dip position when the air gap is small; the dip converges to a constant frequency as the air gap increases. At larger incident angles, the coupling of the evanescent waves to surface waves is smaller and the dip position converges faster. This is because larger incident angle provides larger k_x and thus larger absolute value of imaginary k_y; so the evanescent wave decays faster. For the surface corrugated photonic crystal, the ATR dip is still strong enough to be observed when the air gap between the prism and the surface of the structure is $10\,mm$ and is already converged except at incident angles near the critical angle. For a single layer of corrugation rods, the coupling is not as strong as for the full structure (photonic crystal and corrugation layer) case. To get good coupling, for the single corrugation layer, the air gap size is chosen to be $7\,mm$.

2.2.2 Experimental results

We studied the surface band of the 2D photonic crystal with different surface modifications. The diameter of the corrugation rods needs to be chosen properly so that the surface dispersion lies within the band gap. When the surface mode goes out of the band gap, the mode can extend into the photonic crystal and is no longer a surface mode. The solid lines in Figures 2.5(a) and 2.5(b) show the dispersion relation of the surface modes when the diameter of the surface rods is $D = 1.83\,mm$ and $D = 2.44\,mm$, respectively. Actually, a single layer of only dielectric rods surrounded by air can support surface modes. The solid line in Fig. 2.5 (c) and (d) shows the surface band of a single layer of circular alumina rods with diameter $D = 1.83\,mm$ and $D = 2.44\,mm$, respectively. These two surface dispersion curves shown in Figures 2.5(c) and 2.5(d) are different from the two (shown in Fig. 2.5(a) and (b)) which also involve the photonic crystal. This can be explained from the fact that the presence of the photonic crystal modifies the surface mode of a single layer.

Fig. 2.5 shows the experimental results of the surface bands together with the calculation results for two different corrugation layers with and without photonic crystal. The solid points

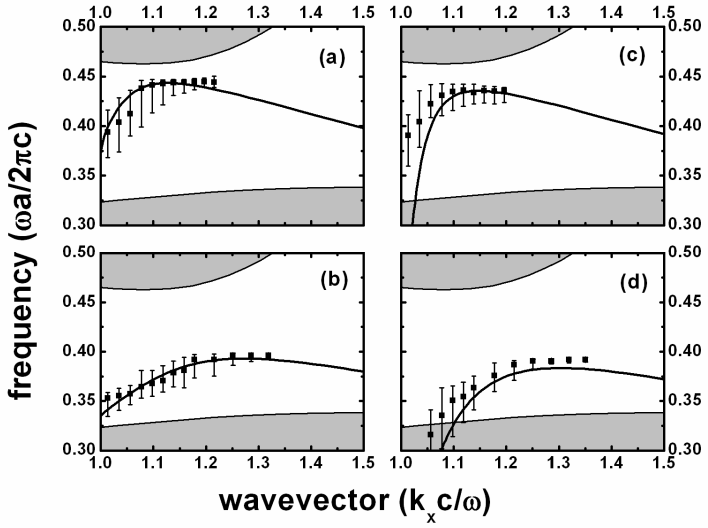

Figure 2.5 Experimental surface band structure of a 2D photonic crystal. Between the light gray areas exist the band gap of photonic crystal. Solid lines and square dots with error bars are supercell band structure calculation and experimental results of the surface band for (a) photonic crystal with a corrugation layer of circular rods with $D = 1.83\,mm$, (b) photonic crystal with a corrugation layer of circular rods with $D = 2.44\,mm$, (c) a single layer of rods with $D = 1.83\,mm$ and (d) a single layer of rods with $D = 2.44\,mm$.

are the averaged dip frequencies over three measurements while the error bar on each point comes from the half width of the reflection dip, averaged over three different measurements. We can see that the experimental results are in good agreement with the calculated surface bands. However, at smaller incident angles, especially close to the critical angle, relatively large error bars are obtained. This is because the finite-width incident beam might not be fully reflected; some plane wave components propagate through the interface and change the coupling to the surface mode. Instead of a nice and sharp coupling dip, the coupling now is over a larger frequency range. That makes the half width of the dip larger. Also the evanescent wave decays slower at smaller k_x and the coupling may not have converged yet at the largest air gap. So the overall experimental error is larger.

Simulations with a similar setup were done in FEMLAB. In the simulations, the source is a Gaussian beam normally incident at one side of a right-angled dielectric wedge. The rod array is set behind the hypotenuse of the wedge. The reflected power is obtained by integrating over the other side of the wedge. To get a coupling at different angles, the two acute angles of the wedge are changed so that the Gaussian beam is always normally incident on the wedge. Compared with experiments (Fig. 2.4), the reflection spectrum in simulations is always smoother. Also, the coupling can still be seen when the air gap is several centimeters large.

2.3 Beaming and enhance transmission through photonic crystal waveguide

In the previous section, we showed that photonic crystals can support surface waves with proper surface modifications. The surface mode dispersion can be traced by numerical tools as well as experiments. In this section, we demonstrate one important application of surface modes. We will show that by exciting the corresponding surface modes, enhanced transmission and directed beaming can be obtained through photonic crystal waveguides of subwavelength width [65].

The effect of the corrugation and grating layers on the beaming of the electromagnetic (EM)

waves from a photonic crystal are presented experimentally. The role of the two components of the beaming, the transmission of the channel and the directionality, are explicitly analyzed. It is demonstrated that a small change, which consists of taking away one grating from the grating layers, can improve the beaming by 20% and opens up a new widow of frequencies with a second beaming in our photonic crystal. These experimental observations can be explained by the derived dispersion relation of the surface waves.

2.3.1 Coupling to subwavelength apertures

As we have discussed, a photonic crystal waveguide can be created by introducing a line defect in the bulk photonic crystal. EM waves can be guided along the waveguide and will not escape into the bulk photonic crystal due to the existence of the bandgap. The waveguide is essentially a local disturbance that breaks the translational symmetry at the interface between the photonic crystal and its surrounding. Consequently, it couples different wavevectors components and allows an incoming normally incident propagating wave with a wavevector $k_{\|} = 0$ to couple to the surface modes with $k_{\|} > \frac{\omega}{c}$ where ω is the frequency and c is the vacuum speed of light. Many waveguide structures based on photonic crystal have been proposed [58, 59, 66]. Qualitative [60] and quantitative [67, 68] explanation of the physics behind the phenomena have been reported. However, in most cases, the apertures of the waveguide openings are smaller than the working wavelength. The problem of a poor coupling between the incident wave and the waveguide, which is not specific to the photonic crystal structures, lead to a low transmission efficiency. Moreover, the outgoing wave from a subwavelength waveguide diffracts in all directions and do not form a directed beam.

It is desirable to get better coupling into and out of the photonic crystal waveguides. For example in optical telecommunications, it is important to get good coupling between photonic crystal waveguides and dielectric waveguides and optical fibers. Due to the different waveguiding mechanism of photonic crystal waveguides and conventional dielectric waveguides, significant reflection and diffraction are expected at the interfaces. A relatively straightforward way is to use tapered structures. Either the photonic crystal waveguide opening, or the dielectric

waveguide end, or both, can be designed to be tapered [69]. It shown in Ref. [70] that, when a self-collimation photonic crystal is added to the photonic crystal waveguide opening, a better directed outgoing beam from the waveguide can be obtained. Directional emission from photonic crystal waveguides are also demonstrated using defected-mode coupling [71, 72]. Defects are introduced near the waveguide opening which serve as scatterers and the directed emission comes from the diffraction from the scatterers.

In parallel to the research on photonic crystals, a lot of discoveries has been made on subwavelength apertures on metals. In 1998, Ebbesen et. al. [73] observed an extraordinary optical transmission through subwavelength hole arrays in optically opaque metal films. It has been shown that this enhancement of transmission is due to the excitation of surface plasmons on the metal-dielectric interfaces [74]. Later on, several experimental works [75, 76] have shown the possibility of enhancing and channeling a beam through metallic structures. The key feature was to corrugate the surface surrounding the aperture allowing the excited surface plasmons at the metallic interface to couple to the outgoing beam (propagating modes) leading to a well directed beam. The potential of applications of such kind of structures has been mentioned in several publications [77–79].

Inspired by the work on metals, people started to apply the idea of exciting surface waves on photonic crystals [58–60, 66–68]. As we have discussed, photonic crystals can support surface waves if their operational frequency is within the photonic band gap. In contrast to metallic surfaces that easily excite surface modes, photonic crystals do not support surface waves unless they are appropriately terminated [63]. Similar to the metallic counterpart, once the surface waves are excited, a grating-like structure can be applied to couple them into the outgoing propagating waves. Under specific conditions, the grating layer destructively interfere the waves everywhere except about the axis of the waveguide resulting to a beaming of the propagating modes in the forward direction. Compare to metallic structures, photonic crystal structures can be advantageous in terms of performance. The Ohmic losses in metallic structures limit their performance in exciting surface plasmons, which is the key feature for the enhanced transmission and the high directionality of the beam. The photonic crystal

structures on the other hand are composed of dielectric materials and generally have lower loss, particularly at higher frequencies.

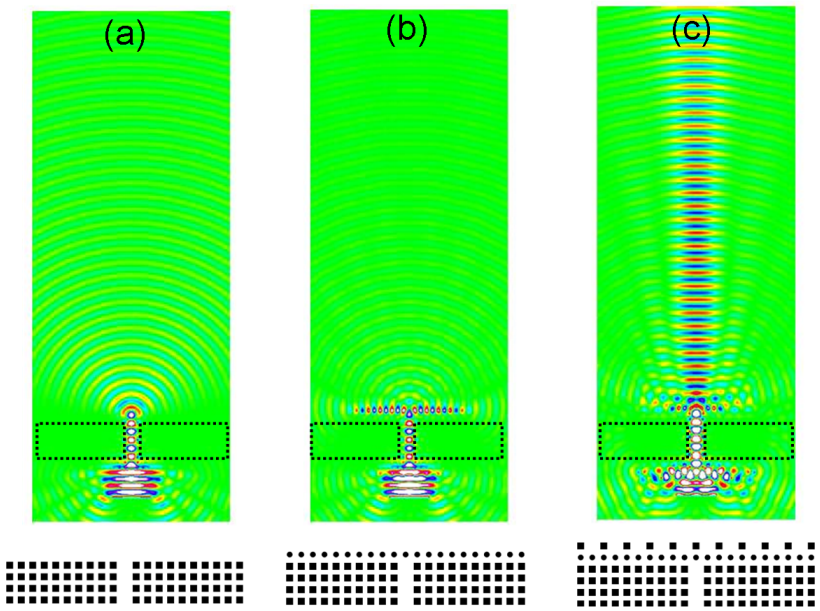

Figure 2.6 The simulated electric field distribution with (a) a regular photonic crystal waveguide formed by a line defect, (b) the same waveguide as in (a) with a modified layer added and (c) the same waveguide as in (b) with a grating layer added. The dashed lines in the figures show the position of the structures. The structures are shown under the corresponding field distributions.

In the following we call the layer on the surface of the bulk photonic crystal used to support surface waves *modified layer* and the extra layer which acts like a grating to couple the surface waves into outgoing beam *grating layer*. Fig. 2.6 is an illustration of the principle. In Fig. 2.6(a), we see clearly that the field propagates inside the waveguide and diffracts at the subwavelength waveguide opening. In Fig. 2.6(b), a modified layer is added to the waveguide. we see that strong field is localized at the surface layer of the waveguide, due to the excitation of a surface mode. However, the field does not couple into propagating wave due to the wavevector mismatch. The outgoing beam still diffracts in all directions. In Fig. 2.6(c), an extra grating

layer is added to the surface-modified waveguide. The grating layer couples the surface mode into propagating wave and interference destructively except in the normal direction. Thus we see a strong main beam along the direction of the waveguide in Fig. 2.6(c). Next we will study the effect of the modified and the grating layers added to the photonic crystal on the surface waves and their coupling to the outgoing modes. By studying the dispersion of surface modes, we are able to predict which conditions lead to higher exited surface waves and consequently to a better beaming.

2.3.2 The experimental setup

The 2D photonic crystal consists of a 2D square array of square alumina rods in air, with parameters of the rods same as before. The dimensions of the structure is 21 layers in the lateral direction and 10 layers in the propagation direction. A schematic picture of the photonic crystal structure and the arrangement for both experiments and simulations is shown in Fig. 2.7. In order to create a waveguide, we omit the ten rods forming the middle row in the structure to channel the beam through it. The actual aperture's width of the waveguide is approximately 1.9 cm measured from the outer-part rods of the photonic crystal. Therefore, for all the frequencies of the incident plane wave (between 10 and 13 GHz), the aperture is smaller than the wavelength of the incident beam. Consequently, we expect the aperture to transmit very poorly and diffract light in all directions. For the modified layer, we add a row of circular rods of diameter 1.83 mm at the beginning and the end of the photonic crystal. As a grating layer a row of square rods of width 3.18 mm is added to the structure with a lattice constant twice the lattice constant of the photonic crystal (see Fig. 2.7).

A finite plane wave source with width of 7.85 cm is placed at a distance 3 cm from the outer interface of the structure. A commercial finite element method software Femlab (COMSOL) was used to calculate the field distribution of the different structures under study. In all the simulations we performed, perfect matched layer (PML) [80,81] boundary conditions were used to surround the computational domain. For both experimental and numerical results a TM polarization (the electric field E is parallel to the axis of the rods) is used. Transmission

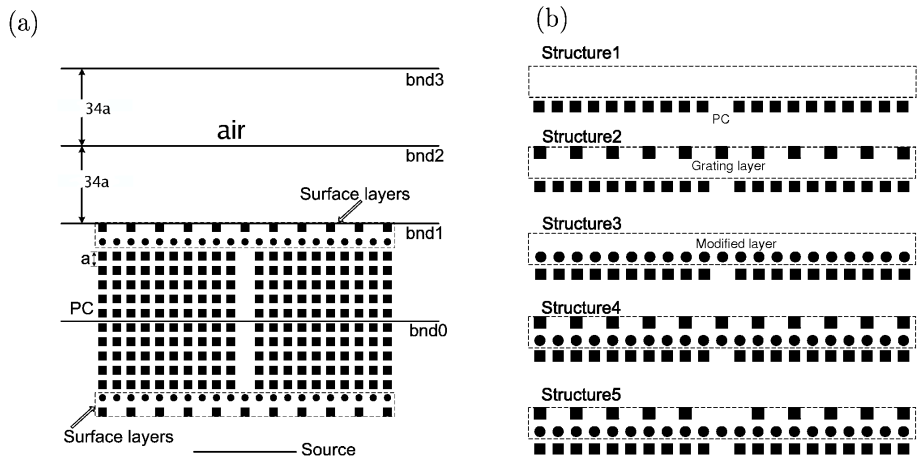

Figure 2.7 (a) The structure's details and definition of the different boundaries used. bnd0, bnd1, bnd2, bnd3 are the boundaries in the channel, at the end of the photonic crystal, in the middle of the air part and at the end of the air part respectively.(b) The shape of the surface layers in each of the fifth different structures.

measurements were performed to verify and test the enhancement as well as the beaming.

The experimental set-up consists of an HP 8510C network analyzer, a horn antenna as the transmitter, and a monopole antenna as the receiver. The monopole antenna is mounted on a motor-controlled 2D table and the position can be controlled by the computer. Each time the position of the monopole antenna is changed, the new transmission data is measured by the network analyzer and recorded to the computer. The field distribution can then be obtained by scanning the area after the photonic crystal aperture.

To differentiate between the portion of the beaming coming from the transmission of the channel and the one coming from the directionality, the following forms of structures have been studied: the waveguide by itself is referred as *structure1*, the waveguide with the grating layers is referred as *structure2*, the waveguide with the modified layers is referred as *structure3*, and the waveguide with both the modified and grating layers is referred as *structure4* (see Fig. 2.7(b)). The power flow which is the time-average of the Pointing vector for each of these structures is examined in different boundaries in the propagation direction in numerical

simulations, as shown in Fig. 2.7(a). The first, second and third boundaries located at the end of the photonic crystal, the middle of the air part and the end of the air part are referred as bnd1, bnd2, bnd3 respectively. The boundary, bnd0, located in the middle of the photonic crystal is the boundary used for normalization.

2.3.3 Enhanced transmission

We will first examine the transmission of the channel, Fig. 2.8 displays the power flow versus the frequency for the four cases measured at boundary (bnd0). The simulated power flow is frequency dependent as it is clearly shown from Fig. 2.8. This figure shows that the transmission of the waveguide depends on the frequency and especially for the structures that grating and both grating and modified layers are added. Second, depending on the termination of the basic structure (structure1), the transmission of the channel is very sensitive to what is at its ends or termination. Notice that for case of structure1, i.e., only the waveguide without modified and grating layers, the transmission for all the range of frequencies is very low. The addition of the grating layer changes waveguide termination and the coupling of EM waves and thus the transmission spectrum (structure2, dashed line in Fig. 2.8). In some frequency region the transmission is increased compare to structure1. However the enhancement is difficult to control and is not what we are looking for. For structure3 (dash-dotted line in Fig. 2.8), a modified layer is added to the waveguide, the transmission does not change much compared to structure1. This is because the surface waves are bounded to the surface region and can not coupling into propagating waves. However, when the grating and the modified layers are added (structure4, dotted line in Fig. 2.8), the power flow is more than five times higher and reaches its maximum of 50% at the frequency of 11.85 GHz that correspond to the beaming frequency. We experimentally checked the transmission of structure4 and the result is plotted in Fig. 2.9. A very good agreement is found between the simulation results shown as solid line and the experimental results shown as dashed line. For both the simulation and the experiment the peak of enhanced transmission in the forward direction occurs at 11.85 GHz.

To show how the transmission of the waveguide depends strongly on the channel termi-

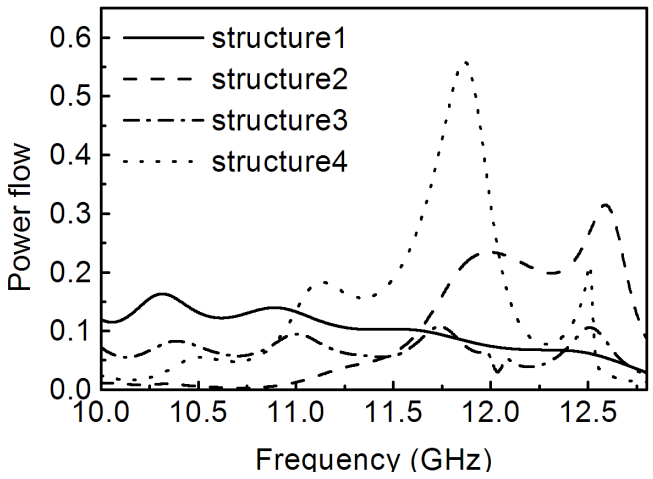

Figure 2.8 Simulated power flow versus frequency measured at boundary bnd0 for the four structures which are only waveguide inside the photonic crystal (structure1), the waveguide with the grating layers (structure2), the waveguide with the modified layers (structure3), and the waveguide with both the modified and the grating layers (structure4).

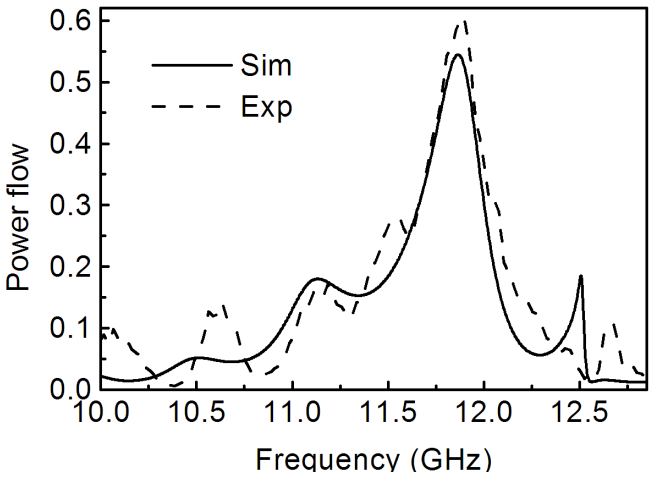

Figure 2.9 Simulation and experimental power flow versus frequency for structure4, which possesses both the gratings and the modified layers.

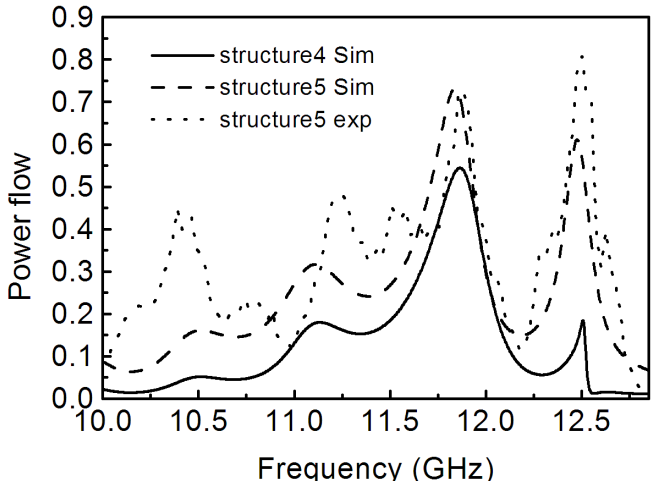

Figure 2.10 Power flow versus frequency for structure4 (simulation only) and structure5 (simulation and experiment). Notice that structure5 is similar to structure4 except for the one grating missing in front and the end of the waveguide.

nation. The forth structure is slightly modified by taking away one grating at the middle of both grating layers. This modified structure will be referred to as structure5 (see Fig. 2.7). Fig. 2.10 displays the simulation and the experimental results of the power flow for structure5 in comparison with those of structure4. First, the most striking change is that the transmission enhancement by almost 20% at 11.85 GHz by just removing only one grating in front of the channel. Second, a very strong transmission peak (more than 80%) is observed at 12.5 GHz making this structure a good candidate to have two strong transmission at two different frequencies. It can be inferred that the back and forth reflection inside the waveguide is very sensitive to any small changes introduced into the structure. Consequently, it plays a major factor in determining the strength of the transmission and therefore the quality of the beaming if it is achieved together with a high directionality. The agreement between the experiment and the simulation is quite good except at low frequency where the experimental results show some structure that can be attributed to the normalization procedures used in the experiment.

2.3.4 Directed emission

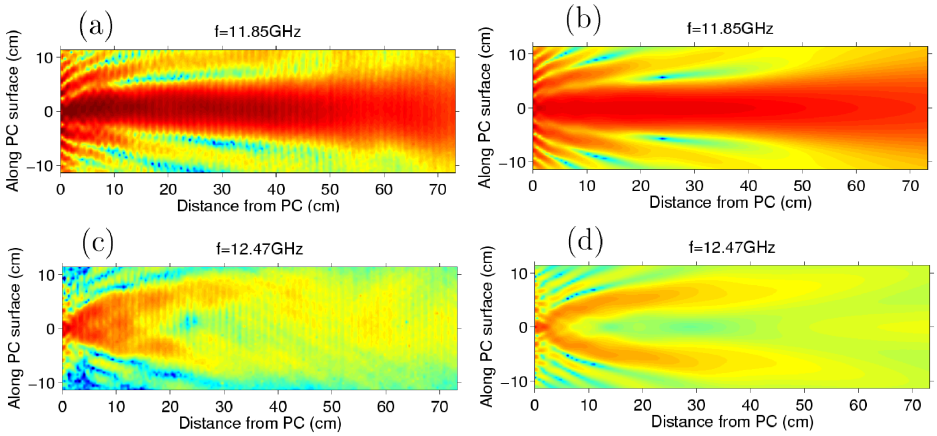

Figure 2.11 A 2d plot of the strength of the outgoing electric field for the case of structure4. (a) and (b) are the experimental and the simulation results respectively at frequency $f = 11.85$ GHz. (c) and (d) are the experimental and the simulation results respectively at frequency $f = 12.47$ GHz.

We next studied the field distribution for different structures both in numerical simulation and experimental measurements. This is a straightforward way to see how the outgoing beam is directed. For further insight on the strength of the field at both beaming and non-beaming frequencies, we plot in Fig. 2.11 the experimental and the simulation results for structure4. The figure is a 2d plot of the strength of the electric field for both experimental (Fig. 2.11(a) and Fig. 2.11(c)) and simulation result (Fig. 2.11(b) and Fig. 2.11(d)). At the beaming frequency (i.e. 11.85 GHz, with experimental result shown in Fig. 2.11(a) and simulation result shown in Fig. 2.11(b)) structure4 generates a very nice beaming that goes further away from the photonic crystal with a noticeable intensity. However, at the non beaming frequency (i.e. 12.47 GHz, with experimental result shown in Fig. 2.11(c) and simulation result shown in Fig. 2.11(d)), the beaming effect disappears, and both experimental and simulation result show a non pronounced field outside the photonic crystal that split in two directions and vanishes afterward. The directed beam is characterized by the line plots shown in Fig. 2.12 for the beaming frequency 11.85 GHz, corresponding to the 2D plots shown in Figs. 2.11(a)

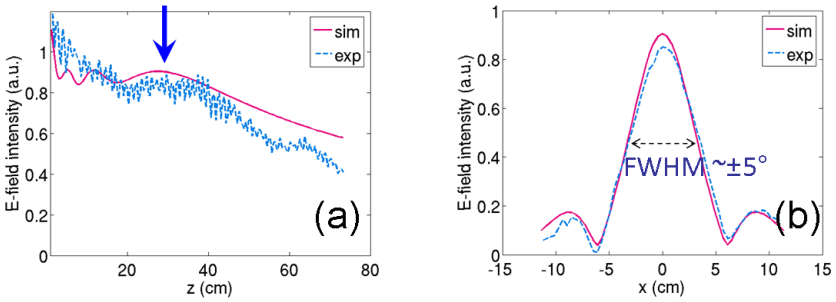

Figure 2.12 The line plots of field intensity for structure4 at 11.85 GHz, corresponds to the 2D distribution shown in Fig. 2.11. for (a) The field intensity along the central line of the waveguide exit (horizontal direction in Fig. 2.11(a)) for structure4 at 11.85 GHz. (b) The field intensity along the interface of the waveguide end (vertical direction in Fig. 2.11(b)), at the horizontal position indicated by the arrow in (a). The solid lines are numerical results and dashed lines are experimental results.

and 2.11(b). Fig. 2.12(a) shows the field intensity along the central line of the waveguide axis, starting from the waveguide exit. The small oscillations close to the waveguide exit are the Fresnel oscillations due to the diffraction effect at the interface. The smooth peak indicated by the arrow is the intermediate field pattern that form the directed beam shown in the 2D plots. At the position of the peak indicated by the arrow in Fig. 2.12(a), the line plot along the waveguide end (vertical direction in Fig. 2.11(b)) is plotted in Fig. 2.12(b). This shows the profile of the main beam. The full width at half maximum (FWHM) is about ±5°. Again the simulation and experimental results agree very well with each other. The directed beam is because a surface mode is excited and coupled to the propagating wave. The grating layer help to build constructive interference along the central line of the waveguide.

In Fig. 2.13, we examine structure5 as we did with structure4 in Fig. 2.11. The field pattern at 11.85 GHz is shown in Figs. 2.13(a) and (b). We see that a well directed beam is formed and is almost identical to the pattern of structure4 (shown in Figs. 2.11(a) and (b)). This is

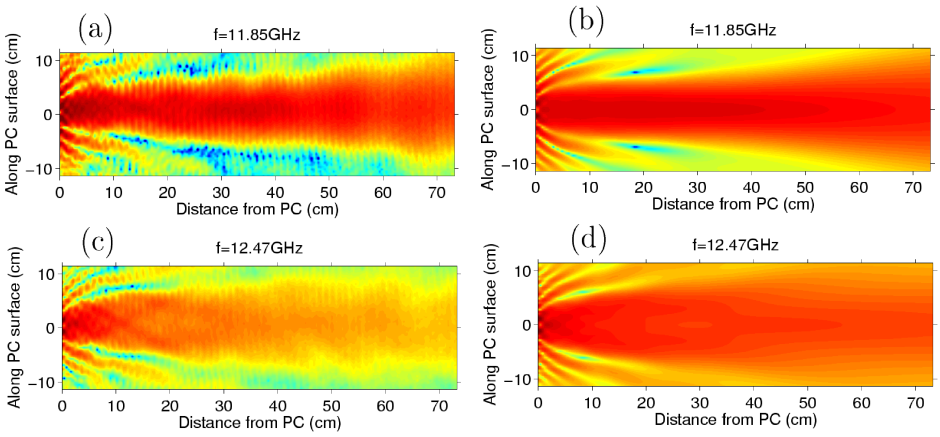

Figure 2.13 A 2d plot of the strength of the electric field for structure5. (a) and (b) are the experimental and the simulation results respectively at frequency $f = 11.85$ GHz. (c) and (d) are the experimental and the simulation results respectively at frequency $f = 12.47$ GHz.

because the same surface mode is excited as in structure4. The result at 12.47 GHz is shown in Figs. 2.13(c) and (d) and looks different than the structure4 results (Figs. 2.11(c) and (d)). The outgoing beam from structure5 is stronger than structure4. This is because the modification of the waveguide termination changes the transmission property, as we have discussed. However, compared to the 11.85 GHz case, the beam at 12.47 decays and diffracts faster when it is away from the waveguide. Again the simulation and experimental results agree well.

We have noticed that at 11.85 GHz, the transmission from the waveguide has a peak value and a nice beam is formed. This is not a coincidence but both because of the excitation of the surface mode. We can find the corresponding surface modes from the surface mode dispersion relation. The band structure of the photonic crystal with modified layer which extends to infinity in the lateral direction is shown in Fig. 2.1, where a surface band can be seen inside the band gap and under the light line. Since the waves coming out from the photonic crystal waveguide tend to diffract in all directions, they have all $k_{//}$ components. Thus for any frequency in the range of the surface band, there exists some $k_{//}$ that satisfies the dispersion relation of the surface band. So, the surface wave excitation should be continuous

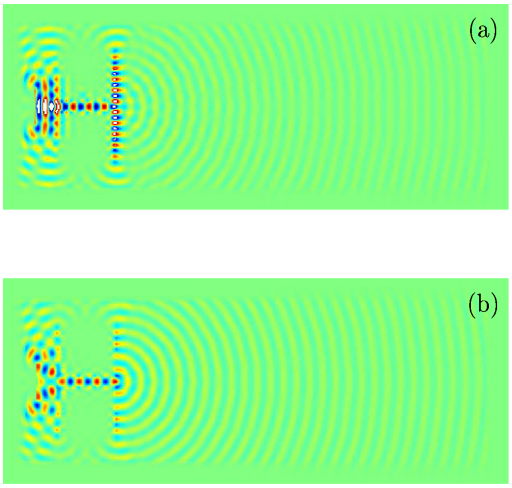

Figure 2.14 Simulated 2d plot of the strength of the electric field of structure3 at (a) $f = 11.97$ GHz and (b) $f = 11.33$ GHz.

over the spectrum for the infinite photonic crystal. However, in our study the photonic crystal has a finite size with 21 rods in the lateral direction. The surface wave excitation in this case is discrete, rather than continuous. This is because at this finite and discrete surface layer, the possible values of $k_{//}$ are discrete. In the first Brillouin zone, $k_{//}$ can be $\frac{2\pi}{Na}m$, where $N = 21$ is the total number of unit cells along the surface and m is any integer between -10 and 10. From the dispersion curve, when $m = 10$, the first surface mode is excited at $f = 11.97$ GHz (Fig. 2.14(a)); when $m = 9$, the second surface mode is excited at $f = 11.33$ GHz (Fig. 2.14(b)). The first mode is expected to be the strongest since it has the largest $k_{//}$ so, the electromagnetic energy is most confined in the surface layer. However, in Fig. 2.14(b) in which $k_{//}$ is smaller, the surface waves are not as strong as for the case of Fig. 2.14(a). Also, the grating has a period of $2a$, which corresponds to the strongest surface mode at 11.97 GHz. Thus the surface mode at 11.97 GHz can be coupled to the propagating wave and a higher transmission and directed beam can be obtained. The actually peak frequency 11.85 GHz differs a little from 11.97 GHz because the addition of the grating layer disturbs the surface mode dispersion and shifts the surface mode frequency.

2.4 Experimental verification of quantized optical conductance in photonic crystal waveguides

Electron conductance has been proved and verified to be quantized in low-dimensional structures. The optical conductance can be defined in a similar way as electron conductance. It has also been shown by experiment in infrared regime that the optical conductance of a metal waveguide is also quantized. It is interesting to observe this effect in photonic crystal waveguides, which have more complicated guiding mechanism than metal waveguides. It is also interesting to observe the classical analog of the quantization effect in microwave regime. In this work, we measure the optical conductance of a photonic crystal waveguide in microwave frequencies and verify that the conductance is indeed quantized [82].

2.4.1 Introduction to quantized conductance

One of the interesting phenomena in science is the quantization of different physical quantities. Quantization occurs because of the wave nature of particles. The quantization effects are getting stronger when the size of the system is getting smaller. One quantity that gives strong quantization is the conductance G. Conductance is the inverse of the resistance $R = \rho L/A$, where ρ is the resistivity, L is the length of the sample and A is the area of the cross section. It is very difficult to calculate analytically the transport properties of small devices. Landauer was the first one to make the connection between the conductance and the transmission coefficient [83, 84]. In particular, Landauer showed that $G = (e^2/\hbar\pi)T/(1-T)$, where T is the transmission coefficient. If one has a perfect metal $T = 1$, and then $G \to \infty$ and therefore $R \to 0$ as expected for a perfect metal. In 1981, Soukoulis and Economou [85] proved, by using the Kubo-Greenwood formula, that for 1D system $G = (e^2/\hbar\pi)T$. There was a big controversy in 1980's which formula was correct (for a historical account of the controversy from two different perspectives, see [86, 87]), since the Economou-Soukoulis formula gave a finite value for the resistance for the perfect metal. The experiments [88–90] resolved this issue and indeed it was found that $G = (e^2/\hbar\pi)T$. Extensions to higher dimension G [91, 92] were achieved and it

was shown that for a multichannel wire

$$G = \frac{e^2}{\hbar\pi} \sum_{n,m=1}^{N_c} |t_{nm}|^2 \tag{2.2}$$

where $|t_{nm}|^2$ is the transmission coefficient between incident mode n and output mode m. If $|t_{nm}|^2 = \delta_{nm}$, the the conductance $G = N_c e^2/\hbar\pi$ is quantized in units of $e^2/\hbar\pi$. Since the conductance quantum $e^2/\hbar\pi$ contains only fundamental constants, the conductance quantization must occur not only in metals, but in semiconductors and superconductors.

The key idea of Landauer was to relate the conduction of electrons with its transmission. So all the idea of quantization of conductance can be also obeyed by all the waves, electromagnetic waves, acoustic and elastic waves. It is amazing that the only experiment [93] that has been done with waves is the transmission of a slit of variable width for a given wavelength of $\lambda = 1.55\mu m$. Transmission steps of equal height occur whenever the slit width W equals half the wavelength. Similar to its electronic counterpart, the optical conductance of a structure is described as the total light transmitted through the structure from a normalized diffuse illumination. In the experiment of Montie *et al.* [93] a two dimensional (2D) diffuser was used to achieve diffuse illumination. The diffuser was essentially a 2D random array of scatterers through which the normally incident plane wave scatters diffusively and isotropically in plane. The diffused light passed through a metal slit and the transmitted light was collected. The result showed that the optical conductance increases in a staircase fashion with a step of $\lambda/2$ in slit width. A new stair occurs when the slit width $W = n\lambda/2$ $(n = 1, 2, 3, ...)$ *i.e.*, a new mode is enabled in the slit.

Photonic crystals can be designed to have a bandgap that prohibits wave propagation in a certain frequency range. Line defects of photonic crystals can confine light with frequencies within the bandgap inside the channel and act as waveguides. photonic crystal waveguides have been studied extensively and many applications in industry have been proposed and realized. However, the concept of optical conductance was not applied to photonic crystal waveguides until recently [94,95] and no experimental work has been reported to our knowledge. We study the optical conductance of photonic crystal waveguides, both numerically and experimentally. We will show that the optical conductance of a 2D photonic crystal waveguide has the similar

staircase effect as the metal slit.

2.4.2 Experimental design

We design the working frequency of the waveguide at microwave region, which makes the photonic crystal easy to fabricate. One of the main difficulties to observe the quantization of the conductance for microwaves frequencies is the need of diffusive waves. This is easy to achieved at optical wavelengths through a diffusor consisting of a random array of particles. For microwaves, a large enough random array of scatters are needed to act as a diffusor to get isotropically diffusive illumination out of a plane source. Since the wavelength is now of the order of centimeters, the diffusor must be really big in size and the intensity of the transmitted waves will be very weak to be used efficiently in microwave experiments. So our idea is to apply Equ. (2.2) to experiments on the conductance of EM waves. We will measure the transmitted power for each particular incident plane wave (wavevector k) with different incident angle separately and sum them up to obtain the conductance of EM waves. The plane wave is provided by a horn antenna and the incident angle can be changed to get different k components.

The photonic crystal we study is a 2D square array of square alumina rods. The lattice constant is $a = 11$ mm and the square rods are of dimension $d = 3.18$ mm with relative permittivity 9.8 and height $h = 15$ cm. Band structure of the photonic crystal shows a bandgap between 9.43 GHz and 12.78 GHz for TM modes (Electric field parallel to the rods). The waveguide is formed by two closely separated pieces of photonic crystal slabs with a size of $25a \times 4a$ each. The width of the waveguide can be varied by changing the distance between the two photonic crystal slabs. In experiments, the two photonic crystal slabs are fixed on two motorized linear stages and the position can be precisely controlled. HP8510B network analyzer and a pair of horn antennas are used to measure the transmission through the waveguide. Both the transmitter antenna and the receiver antenna are mounted on motorized rotational stages such that both the incident and outgoing angle can be controlled. The antennas can move along a semicircle with a radius of 30 cm which is centered at the middle of the near end of

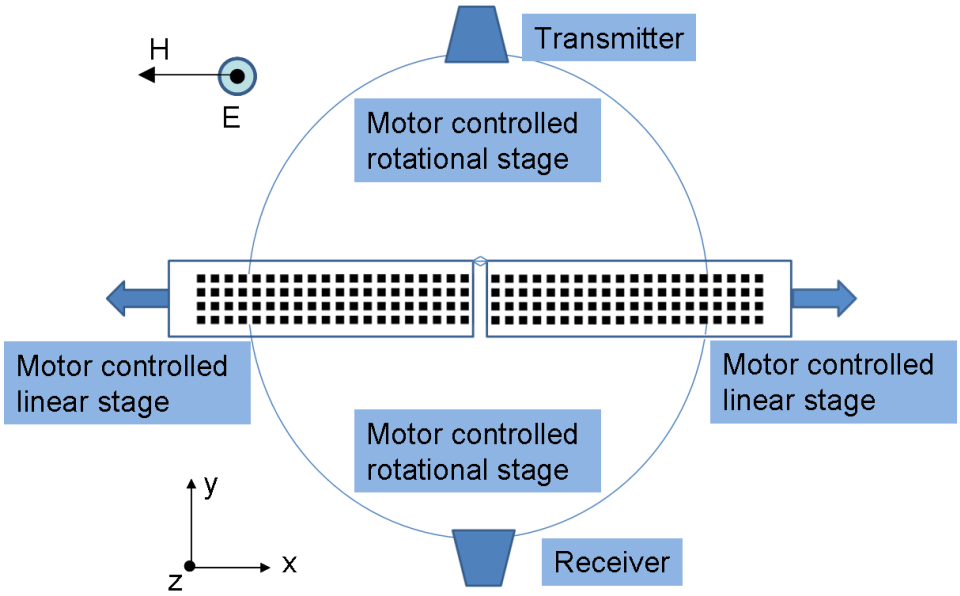

Figure 2.15 An illustration of the experimental setup.

the waveguide (See Fig. 2.15 for details).

2.4.3 Results and discussion

The experimental result of the optical conductance of the photonic crystal waveguide is shown together with numerical simulations in Fig. 2.16. We see that the optical conductance increases in a staircase manner, in both experiments and simulations, with the increase of the waveguide width. The stairs has basically the same height and a new stair appears every $\lambda/2$ when a new mode is introduced in the waveguide. The first waveguide mode is enabled at the onset of the first stair and this position is determined by the band structure of the photonic crystal waveguide. From Fig. 2.16 we can see that the onset of the stairs in experiments and simulations are in good agreement. However, the oscillations at the onset of stairs in simulations, which are proved to be Fabry-Pérot resonances, are missing in the experiments. The major reason is that, while in simulations the model is perfectly 2D and all the transmitted power can be collected without scattering into z direction, we do not have an ideal 2D system. The source we get from a radiating horn antenna is a confined beam. When the antenna is

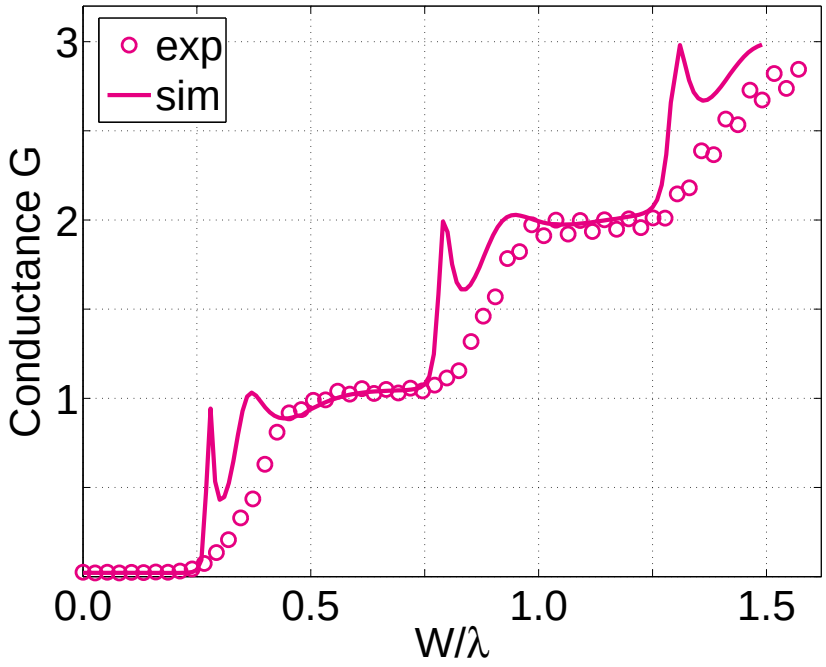

Figure 2.16 The experimental (circles) and numerical (solid line) results of optical conductance of a photonic crystal waveguide at 10 GHz.

far away from the waveguide and the waveguide width is small, the beam can be considered to be uniform in x direction over the waveguide entrance. However in z direction, the incident beam is confined but not uniform. When it encounters the photonic crystal structure, while the main part is propagating in xy plane the beam also scatters out of the plane. Since the receiving antenna only collects the transmitted power in the xy plane where it sits, not all the transmitted power is obtained due to the out of plane scattering. At the onset of the stairs, more power is lost due to the multiple reflection. So the experimental curve is lower than the one obtained by simulations and the Fabry-Pérot resonances are missing.

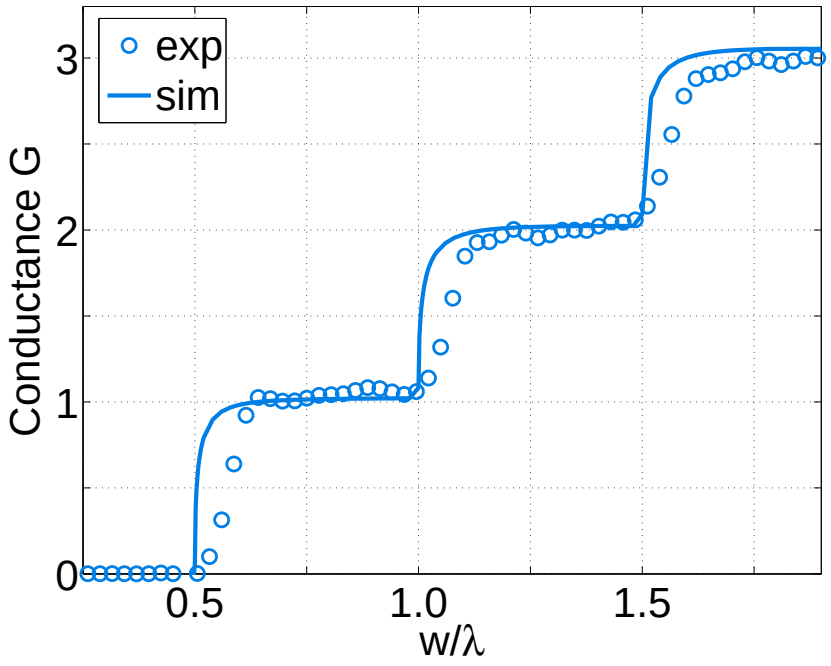

Figure 2.17 The experimental (circles) and numerical (solid line) results of optical conductance of a metal channel for TM case (E field perpendicular to the plane).

We also studied the optical conductance of a metal channel, which serves as a simplified model of the optical waveguides. Analytical calculations starting from Maxwell's equations are performed to understand the mechanism behind the stairs. Neglect the reflections at the two ends of the metal channel, a smooth curve of optical conductance is obtained without the

Fabry-Pérot resonances. Numerical simulations are also executed in which the reflections are also removed by applying a PML layer. The result is in good agreement with the analytical curve. Experimental measurements have also been done and the results are shown together with the numerical results in Fig. 2.17 for TM (E in z direction) case.

2.5 Conclusion

In conclusion, we studied the surface modes and wave guiding properties of 2D photonic crystals. Photonic crystals with proper surface defects can support surface modes and the dispersion relation of the surface modes can be obtained by numerical calculations and experimental techniques. Attenuated total reflection experiments were done to trace the surface mode dispersion of the photonic crystal and the results agree with numerical calculations. We then studied how the surface modes can improve the transmission properties of photonic crystal waveguides. With surface modes excited and coupled to propagating waves, the transmission through the photonic crystal waveguide, which is a subwavelength aperture, can be largely enhanced. Meanwhile, the outgoing beam is shown to be focused and directed to a small angular range, instead of diffracting in all directions. The photonic crystal waveguide is further studied in terms of optical conductance, which is, shown by experimental measurements, to be quantized. The quantization effect is due to the discrete waveguide modes that are allowed to propagate inside the waveguide.

CHAPTER 3. Study of nonlinear split-ring resonators

3.1 Introduction

While most of the research in metamaterials is in the linear regime, where the electromagnetic responses are independent of the external fields, some effort has been made to study the nonlinear effects of the metamaterials, especially the nonlinear tunability of the split-ring resonators (SRRs) [48, 96–99]. The SRRs are essentially LC resonators and the resonance frequency is determined by the geometry of the rings. To tune the magnetic responses of the SRRs, extra components or materials need to be introduced into the SRRs.

In Ref. [100], ferroelectric films are added to the substrate of the SRRs and the magnetic tunability is achieved by controlling the electric permittivity of the ferroelectric films with the change of temperature. In Ref. [101], low-doped semiconductors are photo-doped within the slits of the SRRs and the magnetic response is tuned by varying the conductivity of the semiconductors with an external light source. In Ref. [102], ferrite rods are introduced to ambient the SRR unit cells and the magnetic resonance is modulated by magnetically tuning the inductance of the ferrite rods by an external magnetic field. Compared to these methods, the use of varactors is more feasible in microwave applications in that the tunability can either be realized by a small DC bias voltage [96, 98, 103] or self-tuned by the intensity of the applied electromagnetic fields without biasing [97, 104]. Tunable metamaterials, based on the nonlinear SRRs with varactors, have been tested experimentally in both transmission line form [98, 99] and bulk form [103].

To study the properties of nonlinear metamaterials, it is important to learn the behaviors of a single SRR and the mutual coupling between SRRs. In this chapter, experiments are completed to analyze the properties of the SRRs loaded with linear and nonlinear elements.

The bistable resonance [97,99] of nonlinear SRRs with one varactor is analyzed. The nonlinear properties of SRRs with one varactor and two varactors are compared. The coupling effect of two nonlinear SRRs are also discussed.

3.2 Varactor diodes

A varactor is a special kind of diode whose capacitance is a variable of the voltage applied to its terminals. The variable capacitance is due to the change of the depletion layer thickness at the p-n junction inside the varactor diode. When there is no external voltage applied, the depletion layer is formed and eventually stabilized due to the balance of electron-hole recombination and the build-in potential across the junction. The capacitance of the varactor is then determined by the thickness of the depletion layer. When the varactor is reverse biased, the applied voltage has the same polarity as the build-in potential and the increased potential makes the depletion layer even wider, thus the capacitance gets smaller. When the varactor is forward biased, the applied voltage is opposite to the build-in potential. The depletion layer gets thinner and the capacitance gets larger. When the forward voltage gets larger, the significant electron-hole recombination process causes current through the diode. The basic working mechanism of a varactor diode is the same as a regular diode. A regular diode makes use of the on/off switching behavior and people tries to fabricate diodes with the voltage-dependence effect of the capacitance as small as possible. On the other hand, a varactor diode is fabricated to exploit the voltage-dependence effect and increase the capacitance tunability.

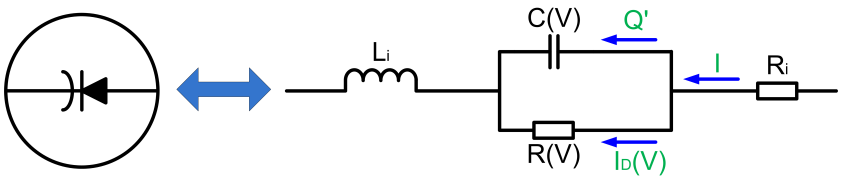

Figure 3.1 The schematic symbol of a varactor (left) and the equivalent circuit model of a varactor (right).

The schematic symbol of a varactor and its equivalent circuit model are shown in Fig. 3.1.

$C(V)$ is the voltage-dependent depletion layer capacitance, $I_D(V)$ is the dissipative current through the p-n junction and $R(V)$ is the effective nonlinear resistance due to the dissipation, which is also voltage-dependent. L_i and R_i are the intrinsic linear inductance and resistance of the diode, respectively.

Thus the current through the diode I is the sum of the change rate of the accumulated charge on the depletion layer capacitance dQ/dt, and the dissipative current $I_D(V)$.

For the Skyworks SMV1231-079 varactor used in our study, the following equations, with the parameters V_D, V_p, I_0 and M provided by the manufacturer, can be used to describe its performance.

$$C(V_D) = C_0 \left(1 - V_D/V_p\right)^{-M}, \tag{3.1}$$

$$I_D(V_D) = I_0 \left(e^{(V_D/V_T)} - 1\right), \tag{3.2}$$

where $C_0 = 2.2$ pF is the DC rest capacitance, $V_p = 1.5$ V is the intrinsic potential and $M = 0.8$. $V_T = k_B T/e$ is the thermal voltage, where k_B is the Boltzmann constant, T is the temperature, and e is the electron charge. Fig. 3.2 shows the voltage-dependent capacitance and the dissipative current plotted with the above equations.

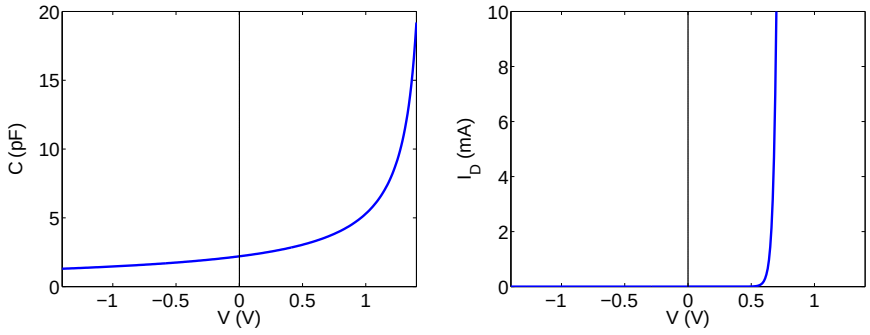

(a) (b)

Figure 3.2 Characteristic curves of the varactor Skyworks SMV1231-079. (a) The capacitance of the varactor vs. the applied voltage. (b) The dissipative current vs. the applied voltage.

3.3 Self-tuning of SRR with varactor

Varactors are most commonly used as voltage-controlled capacitors under reverse biasing. The magnetic metamaterials with varactors have also been studied by other groups [96,98,103]. They use external DC bias to tune the capacitance of the varactor, and the resonance frequency of the SRRs. Since an SRR is essentially an LC resonator, the tunability of its resonance with a tunable capacitor is expected. However, this tunability by DC biasing is different from the nonlinear effect we want to study. For a nonlinear metamaterial, the response is a function of the applied electromagnetic field. In other words, the response of a nonlinear metamaterial is self-tuned by the applied electromagnetic field. In general, the nonlinear response of an SRR is negligible unless the field intensity is very strong. It is not

In this chapter, as a model system, we study the self-tuning of nonlinear SRR with the help of varactors. The study of the response of individual SRRs and the coupling between SRRs would be helpful in the design of nonlinear metamaterials.

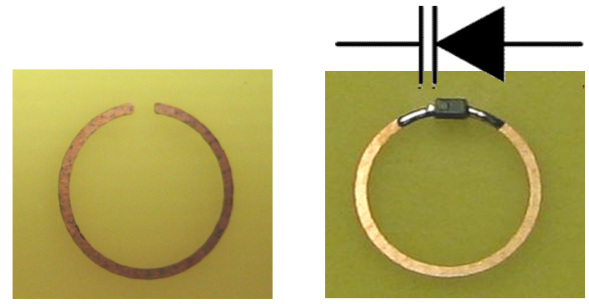

(a)

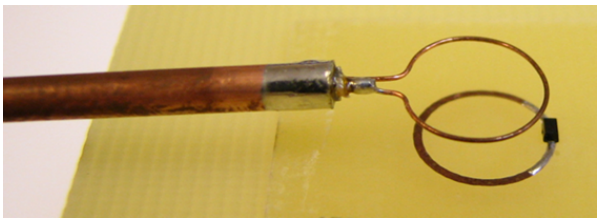

(b)

Figure 3.3 (a) The fabricated SRR is shown on left and the SRR with a varactor mounted into the gap is shown on right. (b) The loop antenna is positioned on top of the SRR and connected to the network analyzer (not shown). The reflected signal is measured by the network analyzer.

In our study, single-ring SRR with a single gap is used for simplication. The ring has an outer diameter of 7 mm, an inner diameter of 6 mm and a slit of width 0.7 mm The SRR is fabricated on a PC board substrate of 0.8 mm thick, with a picture shown in Fig. 3.3(a). The magnetic resonance frequency of the SRR is around 4 GHz. To tune the resonance of the SRR, a varactor is mounted across the gap of the ring, the picture of the tunable SRR is also shown in Fig. 3.3(a). The resonance of the SRR is captured by a loop antenna, as shown in Fig. 3.3(b). The loop antenna is made by a semi-rigid coaxial cable and connected to the port of the network analyzer. The loop antenna has a diameter of 8 mm and is not resonant over the frequency region we are measuring. Most of the power is reflected back to the cable unless the loop antenna is coupled to the resonance of the SRR. In the reflection spectrum, the resonance is shown as a dip in the flat background. By changing the input power, we can see the resoance change of the SRR by looking at the reflection spectrum of the loop antenna.

For comparison, an SRR with a high-Q capacitor ($2pF$) mounted in the gap is also studied as the corresponding linear system. The capacitance of the capacitor is chosen so that it is approximately the same as the rest capacitance of the varactor diode used in this study. With the capacitor or diode, the capacitance of the SRR is greatly increased and the resonance frequency is moved down to 0.9 GHz. The resonance of the SRR with high-Q capacitor does not shift with input power levels, as expected. Note that the insertion of the capacitor boosts the ratio of wavelength and structure size to about 50. This can be useful to miniaturize the size of potential microwave devices [105].

The measured reflection with the SRR loaded with a varactor at different input power levels is shown in Fig. 3.4. When the SRR is off resonance, the reflection spectrum is flat, which means the signal of the loop antenna is not affected by the SRR. At the resonance of the SRR, the loop antenna is coupled to the SRR and energy from the antenna is dissipated during the process. So we observe a dip on the reflection spectrum. When the incident power is low, the reflection dip is sharp and narrow, which means the loss at resonance is relatively low. When the incident power is increased, the resonance frequency is shifted to lower frequencies. Meanwhile, the reflection dip gets shallower and wider, which means the loss is higher. When

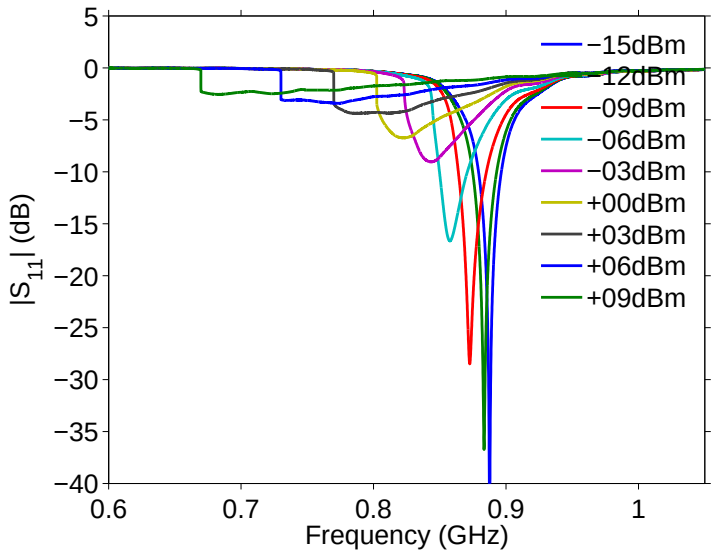

Figure 3.4 The reflection of the SRR loaded with one varactor, measured by a loop antenna. The curves show the measurement results at input power from -15 dBm to 9 dBm in 3 dBm steps.

the incident power gets even larger, the response of the reflection starts to show discontinuous jumps. Also, at lower power, the frequency shift is relatively small; at higher power, the frequency shifts drastically.

When the input power gets higher, the capacitance gets larger. Thus the resonance frequency, determined by $1/\sqrt{LC}$, is smaller. The different behaviors at low power and higher power is because the sources of the nonlinearity are different. At lower power, the induced voltage on the varactor diode is relatively small and the only source of nonlinearity is the depletion layer capacitance. In this case the dissipative current is not involved yet so that the loss during the process is relatively small. Also the capacitance change due to the change of power is small so that the frequency shift is not so obvious. At higher power, the induced voltage on the varactor diode gets higher and the dissipative current sets in. The nonlinearity is now from the combined effect of the nonlinear capacitance and the nonlinear current. Thus the loss during the resonance is higher and the reflection dip gets shallower and wider. Also the nonlinearity is much stronger and the frequency shift due to the change of incident power

is much larger.

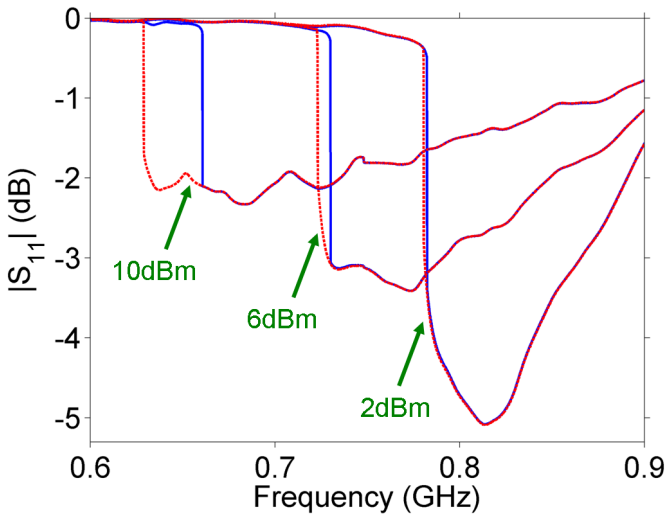

Figure 3.5 The hysteresis effect at high input power levels. The blue curves are measured for forward sweep (the source frequency of the network analyzer is scanned from low to high) and the red dashed curves are measured for reverse sweep (frequency is scanned from high to low).

We now take a closer look at the reflection spectrum at high incident powers. To get the reflection spectrum, the reflection of the loop antenna at different excitation frequencies is recorded. The network analyzer records the reflection at one frequency and then move to the next frequency until all the frequencies are recorded. The frequencies can be swept in two ways: from low frequency to high frequency, or from high frequency to low frequency. We call the sweep from low frequency to high frequency forward sweep, and the sweep from high frequency to low frequency reverse sweep. The two sweep methods are both obtained and plotted for higher input powers, as shown in Fig. 3.5. We see discontinuous jumps in both forward sweep and reverse sweep. Moreover, the reflection curve jumps at different frequencies for forward sweep and reverse sweep. The higher the input power, the larger the discrepancy. This is the behavior of a bistable resonance. The resonance frequency is multivalued and which value it chooses depends on the history of the coupling between the antenna and the

SRR. The discrepancy between forward sweep and reverse sweep curves is because they pick different branches. When the input power is higher, the multivalued frequency region gets larger thus the discrepancy between the forward sweep and reverse sweep gets larger. The above experimental results can be explained by a nonlinear resonator model shown below.

3.4 The simplified driven nonlinear resonator model

Below, we present some analytical arguments to explain the tunability and the hysteresis effects of the nonlinear SRRs observed experimentally.

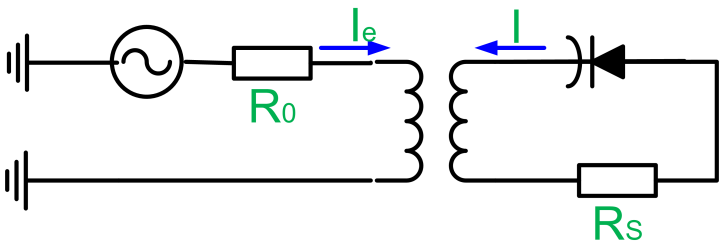

Figure 3.6 The circuit model of the coupling between the driven loop antenna and the SRR loaded with one varactor.

The system of the driven loop antenna and the nonlinear SRR can be modeled by an equivalent circuit, as shown in Fig. 3.6. The signal source, shown on the left side, is connected to the loop antenna; the antenna is coupled to the nonlinear SRR via mutual inductance. I_e and I represent the current in the loop antenna and the SRR; R_0 and R_S are the resistance of the antenna and the SRR, respectively. Then the driven RLC circuit can be expressed by the following voltage equation

$$-L\frac{dI}{dt} - R_S - V_D = \varepsilon(t), \tag{3.3}$$

where L is the inductance of the resonator determined by the ring geometry, and ε is the driven term provided by the loop antenna.

As we mentioned before, both the depletion layer capacitance and the dissipative current are voltage dependent, which makes the analysis of the system complicated. However, from

Fig. 3.2, we can see that the dissipative current can be neglected for small signal excitations. For simplication, the following analysis assumes small signal excitation and considers the nonlinear capacitance only. The current through the diode is then determined only by the change rate of the accumulated charge.

For small excitations, I_D can be neglected so the current can be estimated by $I \approx dQ_D/dt$. From $C(V_D) = \frac{dQ_D}{dV_D}$, we can determine the time-dependent charge,

$$Q_D = \frac{C_0 V_p}{1-M}\left[1 - (1 - V_D/V_p)^{1-M}\right]. \tag{3.4}$$

Assume $V_D < V_p$, then the voltage across the diode can be expressed by the charge

$$V_D(q) = V_p\left[1 - \left(1 - q\frac{1-M}{V_p}\right)^{\frac{1}{1-M}}\right], \tag{3.5}$$

where the renormalized voltage is defined as $q = Q_D/C_0$.

The equation of motion is now

$$\frac{d^2q}{dt^2} + \gamma\frac{dq}{dt} + \omega_0^2 V_D = -\omega_0^2\varepsilon(t), \tag{3.6}$$

where $\omega_0^2 = 1/(LC_0)$ and $\gamma = \omega_0^2 R_S C_0$.

Expand the restoring term V_D by the Taylor series for small oscillations (the oscillation amplitude satisfies $(1-M)|q| < V_p$) and omit the higher order terms,

$$V_D(q) \approx q - \frac{M}{2V_p}q^2 + \frac{M(2M-1)}{6V_p^2}q^3. \tag{3.7}$$

Assume harmonic excitation so that $\varepsilon(t) = f\cos(\omega t)$, where f is the excitation amplitude and ω is the excitation frequency, the equation of motion is further estimated by

$$\frac{d^2q}{dt^2} + \gamma\frac{dq}{dt} + \omega_0^2 q + \alpha q^2 + \beta q^3 = -\omega_0^2 f\cos(\omega t), \tag{3.8}$$

where $\alpha = -\frac{\omega_0^2 M}{2V_p}$, $\beta = \frac{\omega_0^2 M(2M-1)}{6V_p^2}$. This is now a nonlinear driven oscillator problem [106].

The driven frequency can be written as $\omega = \omega_0 + \delta$. When δ is small, the driven frequency is close to the resonance frequency. Without the q^2 and q^3 term, the oscillator is linear and the amplitude of oscillation, b, is given by

$$b^2\left(\delta^2 + \gamma^2/4\right) = \omega_0^2 f^2/4. \tag{3.9}$$

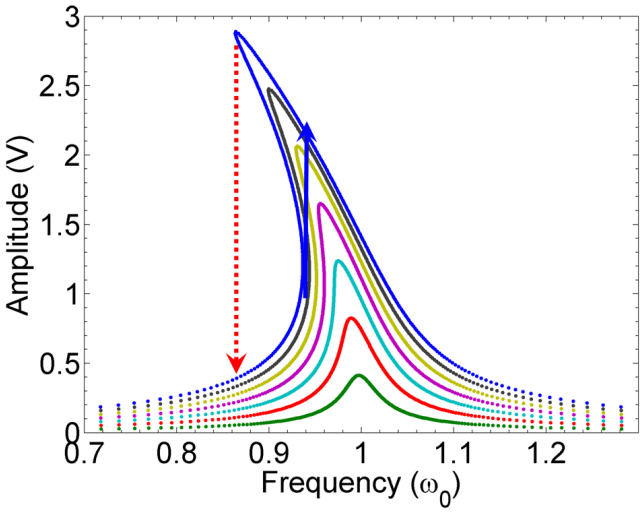

Figure 3.7 The oscillation amplitude vs. source frequency calculated from the simplified nonlinear oscillator model. The curves from bottom to top correspond to excitation power from low to high. The blue arrow shows the jump for forward sweep of the top curve and the red arrow shows the jump for reverse sweep of the top curve.

The nonlinear q^2 and q^3 terms make the eigen-frequency amplitude dependent, $\omega_0 \to \omega_0 + \kappa b^2$, where $\kappa = \frac{3\beta}{8\omega_0} - \frac{5\alpha^2}{12\omega_0^3}$. Then $\delta \to \delta - \kappa b^2$, and the oscillation amplitude satisfies the equation

$$b^2 \left[\left(\delta - \kappa b^2\right)^2 + \gamma^2/4 \right] = \omega_0^2 f^2/4. \tag{3.10}$$

This is a cubic equation about b^2 and the real roots give the amplitude of oscillations. When the external excitation is small, the oscillation amplitude is also small and the higher orders of b may be neglected and the oscillation can be considered to be linear. When the excitation power is larger, the curve is distorted and the resonance shifts to a lower frequency, since, in our case, κ is negative. When the excitation power is large enough, there are three real roots of b^2 and the curve is folded over, see Fig. 3.5. The branch in the middle is unstable and the oscillation tends to go to the other two branches. In experiment, the oscillation follows the lower branch until it jumps to the higher branch for forward sweep, and follows the higher branch until it jumps to the lower branch. So, the hysteresis effect is observed in our experimental measurements. Note, when the voltage on the varactor is larger than 0.5 V, the nonlinear DC dissipative current sets in and this increases the loss on the SRR and the reflection dip measured is not as strong as the small oscillation case. See Fig. 3.4, the reflection minimum increases from around -40 dB to -3 dB when the input power is increased from -15 dBm to 9 dBm. This is not covered in the simplified model of the nonlinear oscillator model.

3.5 Nonlinear SRR with back-to-back varactors

To remove the nonlinear DC current and obtain a better self-tuning effect, a new SRR is fabricated. The SRR ring is of the same geometry, but with another identical cut on the other side of the ring and a varactor is mounted onto each of the cuts, see inset in Fig. 3.8. The varactors are arranged back-to-back such that no DC current can circulate in the SRR and the effective capacitance characteristics $C(V)$ of the two varactors is now symmetric. This configuration has similar effect of one heterostructure barrier varator (HBV) diode [104]. The two varactors can now be regarded as two tunable capacitors connected in a series. The total capacitance is smaller than a single varactor at the same power level, so that the resonance

frequency shifts to a higher region (see Fig. 3.8). When the input power increases, the effective capacitance decreases and the resonance frequency increases. When the input power is changed from -14 dBm to 2dBm, the resonance frequency is shifted upward by 20%. Also see from Fig. 3.8 that the resonance strength and the quality factor are almost the same for different input power levels. These nice features make this configuration a perfect candidate for nonlinear tuning in metamaterials. The only problem with this configuration is that the varactors discharge very slowly, due to the lack of a circulating current.

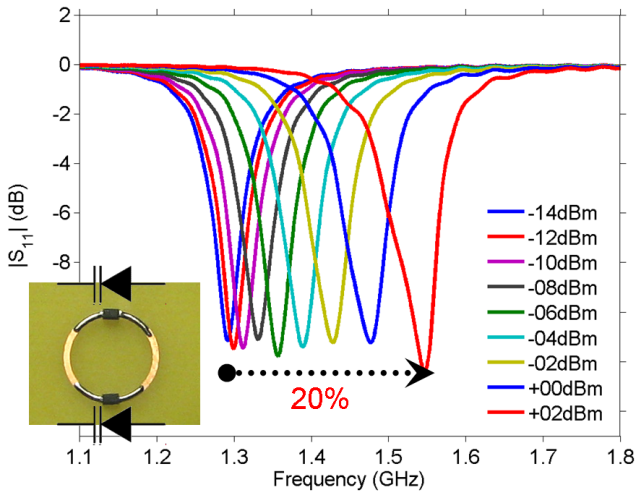

Figure 3.8 The reflection of the SRR loaded with two back-to-back varactors, measured by a loop antenna. The curves show the measurement results at power levels from -14 dBm to 2 dBm, in 2 dBm steps. The inset shows the sample.

3.6 Coupling between nonlinear SRRs

To make nonlinear metamaterials out of the nonlinear SRRs, the mutual coupling of the varactor loaded SRRs must to be studied. Since the mutual coupling of two coplane SRRs are very weak, we studied the case of two parallel SRRs with the same axis (solenoid case). The loop antenna is also parallel to the two SRRs and has the same axis. The distance of the antenna and the first SRR is fixed, and the second SRR is moved away from the first SRR.

Reflection is measured by the loop antenna for different distances between the two SRRs. In Fig. 3.9(a), we present the frequency-dependence of the reflection coefficient for two linear SRRs, as the distance between the two SRRs increases. As one can see from Fig. 3.9(a), if the distance between the SRRs is large, only one reflection resonance is observed and as the two SRRs move closer, the mutual coupling becomes stronger and the reflection splits. The closer the two SRRs, the wider the split. For two linear SRRs, the mutual coupling can be calculated analytically with a simple LC model.

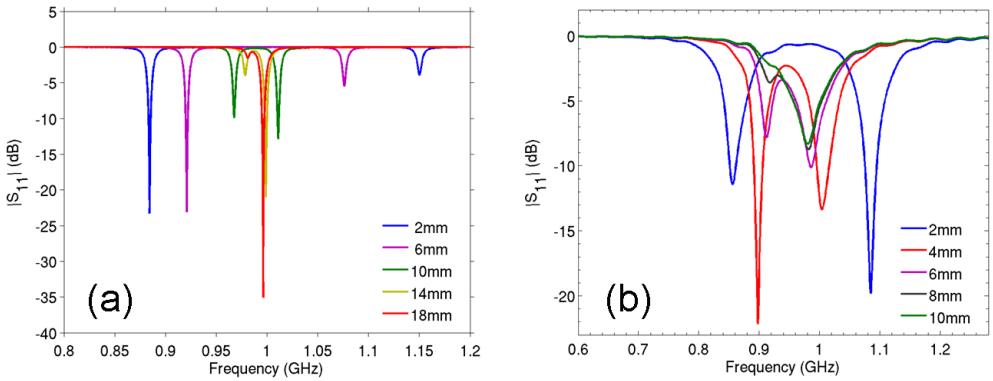

Figure 3.9 The reflection of (a) two linear SRRs and (b) two nonlinear SRRs at input power of −15 dBm. The legend shows the distance between the two SRRs. The distance between the first SRR and the antenna is fixed.

In Fig. 3.9(b), we present the frequency-dependence of the reflection coefficient for two nonlinear SRRs, as the distance between the two SRRs increases. The incident power is −15 dBm, which is relatively low and the results presented in Fig. 3.9(b) are almost equivalent to the linear SRRs presented in Fig. 3.9(a), except that the reflection dip is not as deep as the linear case, due to a higher loss in the varactor than the high-Q capacitor. When the input power is low, the nonlinear SRRs behaves like the linear ones and the splitting is nicely seen in the -15 dBm case of the 2d plot in Fig. 3.10. When the input power gets higher, the resonance of the SRR gets broadened, due to higher loss and the splitting becomes worse, as seen in Fig. 3.10. One can clearly see from Fig. 3.10 that the hybridization gets very weak as the

incident power increases.

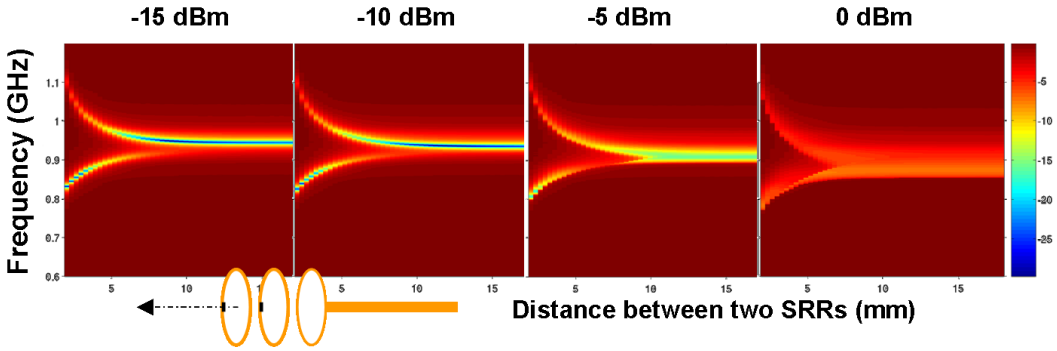

Figure 3.10 The 2d plot of the reflection of two coupled nonlinear SRRs. The x-axis shows the distance between the two SRRs and the y-axis shows the frequency. The four figures from left to right display the result at input power from -15 dBm to 0 dBm. The SRRs and the antenna are arranged such that they have the same axis and the planes of the rings are parallel to each other. The distance between the loop antenna and the first SRR is fixed and the second SRR is movable along its axis, as seen from the inset.

3.7 Conclusions

In conclusion, we have demonstrated experimentally dynamic tunability, hysteresis, and bistable behavior in nonlinear SRRs. The nonlinear SRR has a typical SRR design and we have soldered in the gap of the SRR a commercial varactor diode. Tunability of the resonance frequency was completed dynamically by increasing the incident power of the vector network analyzer. We have introduced different nonlinear designs and observed experimentally that the resonance frequency can decrease or increase by increasing the incident power. This way, we are able to change the sign of the nonlinearity. A theoretical model was given that explained the observed nonlinear effects. Finally, we study the hybridization effects of the linear and nonlinear SRR.

CHAPTER 4. Chiral metamaterials

Conventional metamaterials require both negative ϵ and negative μ to achieve negative index of refraction. Chiral metamaterial is a new class of metamaterials offering a simpler route to negative index and consequently negative refraction. In this chapter, we briefly review the history of metamaterials and the developments on chiral metamaterials. We study the wave propagation properties in chiral metamaterials and show that negative index can be realized in chiral metamaterials with a strong chirality, with neither ϵ nor μ negative required. We have developed a retrieval procedure, adopting uniaxial bi-isotropic model to calculate the effective parameters $n_{\pm}$, κ, ϵ and μ of the chiral metamaterials. Our work on the design, numerical calculations and experimental measurements of chiral metamaterials, will be introduced. Strong chiral behaviors such as optical activity and circular dichroism are observed and negative refraction is obtained for circularly polarized waves in these chiral metamaterials. The potential applications of chiral metamaterials, including resonant absorbers, will be discussed.

4.1 Introduction

A chiral medium is composed of particles that can not be superimposed on their mirror images [107]. A chiral medium has different responses for a left circularly polarized (LCP) wave and a right circularly polarized (RCP) wave due to the intrinsic chiral asymmetry of the medium. Also, there is cross-coupling between electric field and magnetic field going through a chiral medium. A dimensionless chirality parameter κ is used to describe this cross-coupling effect. The refractive indices of RCP and LCP waves become different due to the existence of non-zero κ. These will be explained in detail in the following sections.

There is a long history in the study of chiral media. In the early 19th century, the optical

rotation in quartz crystals as well as some liquids and gases has already been discovered by Biot and others [108]. Biot also suggested that the phenomenon has a root in the molecules. The handedness nature of the molecules in optically active materials is confirmed by Pasteur in the 1840's [107]. The discoveries turned out to be useful in areas such as analytical chemistry and pharmaceutics. In 1873, Lord Kelvin first used the word "chirality" to describe the handedness in his lectures [109]. In 1910's Lindeman managed to bring optical activity phenomenon in visible lights to radio waves, with a collection of helical coils served as artificial chiral "molecules" [107]. The studies of chiral media in microwave region have found applications in many areas such as antennas, polarizators, and waveguides [110].

In 2003, Tretyakov *et.al.* [111] discussed the possibility to realize negative refraction by chiral nihility. The authors first proposed the idea to fabricate a metamaterial composed of chiral particles, such as helical wires. To get negative refraction for one of the circular polarizations, κ needs to be larger than $\sqrt{\epsilon\mu}$. In natural materials such as quartz and sugar solutions, κ is generally much smaller than 1, while $\sqrt{\epsilon\mu}$ is generally larger than 1. So negative refraction is not possible in natural chiral materials. However, with chiral metamaterials, the macroscopic parameters can be designed. The idea of chiral nihility is that, when ϵ and μ of a chiral medium are small and very close to zero, the chirality can make the refractive index for one circular polarization to become negative, even when κ is small.

The metamaterial based on chiral nihility is a special case of chiral metamaterials. In 2004, Pendry [2] discussed in general the possibility to achieve negative refraction in chiral metamaterials. He analyzed the conditions to realize negative refraction in chiral metamaterials and showed that they are simpler than regular metamaterials, which require both electric and magnetic resonances to get negative ϵ and negative μ. In chiral metamaterials, neither ϵ nor μ needs to be negative. As long as the chiral parameter κ is large enough, negative refraction can be obtained in chiral metamaterials.

4.2 Wave propagation in chiral media

Chiral media belong to a wider range of bi-isotropic (BI) media. BI media [107] are characterized by the following constitutive relations

$$\mathbf{D} = \epsilon_0\epsilon\mathbf{E} + (\chi + i\kappa)\sqrt{\mu_0\epsilon_0}\mathbf{H} \tag{4.1}$$

$$\mathbf{B} = \mu_0\mu\mathbf{H} + (\chi - i\kappa)\sqrt{\mu_0\epsilon_0}\mathbf{E} \tag{4.2}$$

where ϵ is the relative permittivity of the medium, ϵ_0 is the permittivity of vacuum, μ is the relative permeability of the medium and μ_0 is the permeability of vacuum. The difference between BI media and regular isotropic media lies in the extra terms of the constitutive relations. χ is the dimensionless magneto-electric parameter, and describes the reciprocity of the material. Materials with $\chi \neq 0$ are non-reciprocal. κ is the dimensionless chirality parameter of the material. Materials with $\kappa \neq 0$ are chiral. The imaginary unit i in the formula is from the time-harmonic convention $e^{-i\omega t}$.

Depending on the values of χ and κ, the BI media can be classified as

- General BI medium: non-reciprocal ($\chi \neq 0$), chiral ($\kappa \neq 0$);
- Tellegen medium: non-reciprocal ($\chi \neq 0$), non-chiral ($\kappa = 0$);
- Pasteur medium: reciprocal ($\chi = 0$), chiral ($\kappa \neq 0$).

We are interested in the Pasteur medium, or the reciprocal chiral medium.

Consider the plane wave propagation in an isotropic chiral medium. Combine the above constitutive relations with $\chi = 0$ and the frequency-domain source-free Maxwell's equations, the following wave equation can be obtained for the electric field $\mathbf{E}$:

$$\mathbf{k} \times (\mathbf{k} \times \mathbf{E}) = -k_0^2 \left(\epsilon\mu - \kappa^2\right) \mathbf{E} - 2i\kappa k_0 \left(\mathbf{k} \times \mathbf{E}\right) \tag{4.3}$$

where $\mathbf{k}$ is the wave vector in the chiral medium, $k_0 = \omega/c$ is the free-space wave vector and $c = \sqrt{\epsilon_0\mu_0}$ is the speed of light in vacuum.

For simplicity, and without loss of generality, we assume $\mathbf{k} = k\hat{z}$. Then the wave equation is simplified and k is solved:

$$k_\pm = k_0(n \pm \kappa) \tag{4.4}$$

where $n = \sqrt{\epsilon\mu}$ is the index of refraction of the medium without chirality. From this equation we can write the chiral parameter κ as $\kappa = \frac{k_+ - k_-}{2k_0}$.

The eigen-vectors, or the allowed solutions of plane waves in the chiral medium can then be obtained from $\mathbf{E}(\mathbf{r}) = (E_{0x}\hat{x} + E_{0y}\hat{y})\, e^{ikz}$. Then we get the following relations:

$$\frac{E_{0y}}{E_{0x}} = \frac{k_0^2(n^2 - \kappa^2) - k_\pm^2}{2ik_0\kappa k_\pm} = \pm i \tag{4.5}$$

So, the wave vector solution k_+ corresponds to the eigen-vector of RCP wave and k_- corresponds to the eigen-vector of LCP wave. Here the handedness is defined as seen from source, or as looking in the direction of propagation. Define the index of refraction of RCP/LCP waves as $n_\pm$, from the relation $k_\pm = n_\pm k_0$, we can get

$$n_\pm = n \pm \kappa \tag{4.6}$$

The polarization plane of a linearly polarized light will rotate when it passed through a chiral medium. This polarization effect is called optical activity and is characterized by the polarization azimuth rotation angle of elliptically polarized light

$$\theta = \frac{1}{2}\delta = \frac{1}{2}\left[\arg(T_{++}) - \arg(T_{--})\right] \tag{4.7}$$

The first subscript in T_{++} and T_{--} indicates the initial polarization and the second subscript indicates the transmitted polarization. So T_{++} and T_{--} are the transmission coefficients for RCP and LCP waves, respectively.

Due to the chiral nature of the medium and the circularly polarized waves, the LCP and RCP light interacts with the particles of the chiral medium differently. This causes the difference in absorption and distortion of the two polarizations going through the medium, which is called circular dichroism. Since the impedance of the chiral medium is the same for the two different polarizations, the reflections of the two polarizations are the same. Then the circular dichroism is characterized by the ellipticity, which is defined from the difference in transmitted power of the two polarizations.

$$\eta = \frac{1}{2}\sin^{-1}\left(\frac{|T_{++}|^2 - |T_{--}|^2}{|T_{++}|^2 + |T_{--}|^2}\right) \tag{4.8}$$

4.3 Effective parameter retrieval of chiral media

In the study of metamaterials, effective parameter retrieval is an important technique to characterize the EM properties of the effective media and is used extensively by researchers, with both numerical and experimental methods to guide the design of new metamaterials and identify the negative refractive behavior of metamaterials.

Effective parameter retrieval is the procedure of obtaining the macroscopic parameters of a medium based on the transmission and reflection coefficients (S parameters) from a planar slab of this medium. For a homogeneous material, ϵ, μ and the refractive index n are intrinsic properties of the material and are independent of the thickness of the slab. Thus one can choose a slab as thin as possible to do the measurements, and thus obtain the parameters without ambiguity. However for a metamaterial slab, the structures are inhomogeneous and the smallest slab thickness is limited by the unit cell size of the metamaterial [112–114]. The retrieval solution in this case is generally multi-branched. The branches need to be chosen carefully to obey energy conservation rules.

For a chiral slab, the retrieval process is analog to that for regular metamaterials, but a little more complicated. The refractive indices for the two eigen-solutions (RCP and LCP waves) need to be calculated [115]. Consider a circularly polarized plane wave normally incident upon a homogeneous one-dimensional (1D) chiral slab of thickness d in vacuum, with refractive index $n_\pm$ and impedance Z for RCP/LCP waves (see Fig. 4.1). The incident wavevector k_0 is in z-direction and the wavevector in the chiral slab for RCP/LCP wave is $k_\pm$. The electric and magnetic field vectors are all tangential to the interfaces in this scenario.

Suppose the incident RCP/LCP electric field has unit amplitude, the reflection coefficient is given by $R_\pm$ and the transmission coefficient after the second interface is given by $T_\pm$. Multireflection happens inside the chiral slab and the transmitting and reflecting waves inside the chiral slab are represented by coefficients $T'_\pm$ and $R'_\pm$ for RCP and LCP waves (see Fig. 4.1). Note that the polarization state is reversed after reflection. Define normalized impedance of the chiral slab as $z = Z/Z_0$, where $Z_0 = \sqrt{\mu_0/\epsilon_0}$ is the free space impedance.

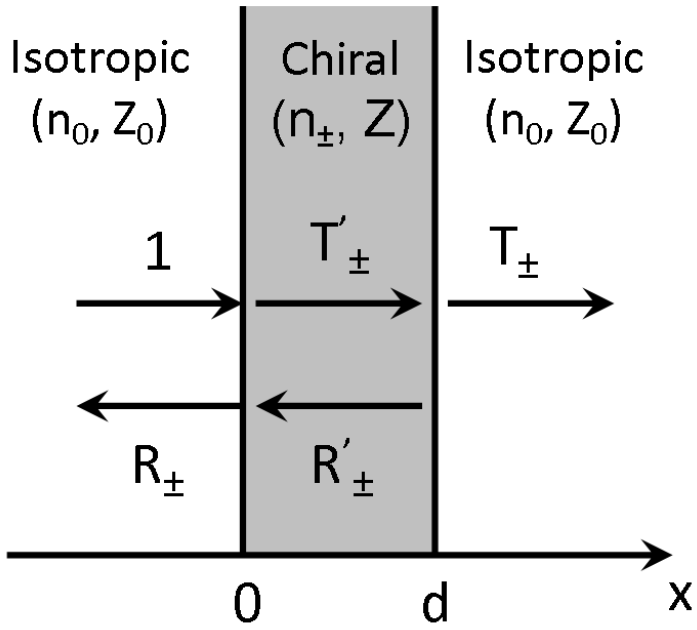

Figure 4.1 The transmission and reflection coefficients of a plane wave incident upon a chiral slab from left.

The tangential electric field and magnetic field are continuous at the first interface ($x = 0$).

$$1 + R_{\pm} = T'_{\pm} + R'_{\pm} \tag{4.9}$$

$$1 - R_{\pm} = \frac{T'_{\pm} - R'_{\pm}}{z} \tag{4.10}$$

Similarly at the second interface ($x = d$),

$$T'_{\pm} e^{ik_{\pm}d} + R'_{\pm} e^{-ik_{\mp}d} = T_{\pm} \tag{4.11}$$

$$\frac{T'_{\pm} e^{ik_{\pm}d} - R'_{\pm} e^{-ik_{\mp}d}}{z} = T_{\pm} \tag{4.12}$$

Note that $k_+ + k_- = 2nk_0$, we can get the transmission and reflection coefficients from the above equations.

$$T_{\pm} = \frac{4ze^{ik_{\pm}d}}{(1+z)^2 - (1-z)^2 e^{2ink_0 d}} \tag{4.13}$$

$$R_{\pm} = \frac{(1-z^2)(e^{2ink_0 d} - 1)}{(1+z)^2 - (1-z)^2 e^{2ink_0 d}} \tag{4.14}$$

R_+ and R_- are equal since the impedance for RCP and LCP waves is the same. If we denote T and R as the transmission and reflection coefficients for the $\kappa = 0$ medium, we have

$$R_\pm = R \tag{4.15}$$

$$T_\pm = Te^{\pm i\kappa k_0 d} \tag{4.16}$$

The impedance and refractive index can be calculated from the above coefficients.

$$z = \pm\sqrt{\frac{(1+R)^2 - T_+T_-}{(1-R)^2 - T_+T_-}} \tag{4.17}$$

$$n_\pm = \frac{i}{k_0 d}\left\{\log\left[\frac{1}{T_\pm}\left(1 - \frac{z-1}{z+1}R\right)\right] \pm 2m\pi\right\} \tag{4.18}$$

where m can be any integer.

The sign of the square root in Eq. 4.17 and the multi-branches in Eq. 4.18 need to be chosen carefully according to the energy conservation principle, i.e. the real part of impedance z must be positive, as well as the imaginary part of n.

Once z and $n_\pm$ are fixed, the other parameters can be identified subsequently. $\kappa = (n_+ - n_-)/2$, $n = (n_+ + n_-)/2$, $\mu = nz$ and $\epsilon = n/z$.

4.4 Review of work on chiral metamaterials

Since the idea was first proposed [2,111], a lot of work has been devoted toward the theoretical understanding, numerical modeling and experimental realization of chiral metamaterials.

4.4.1 Theoretical studies

In Pendry's pioneering work [2], he proposed a design to realize strong chiral metamaterials. The design is a twisted version of the "swiss roll" structure, as shown in Fig. 4.2(a). Realistic parameters of the structure were estimated by theoretical calculations. Very recently, this design has been shown by experiments to have strong chirality and negative refractive index in microwave regime [116].

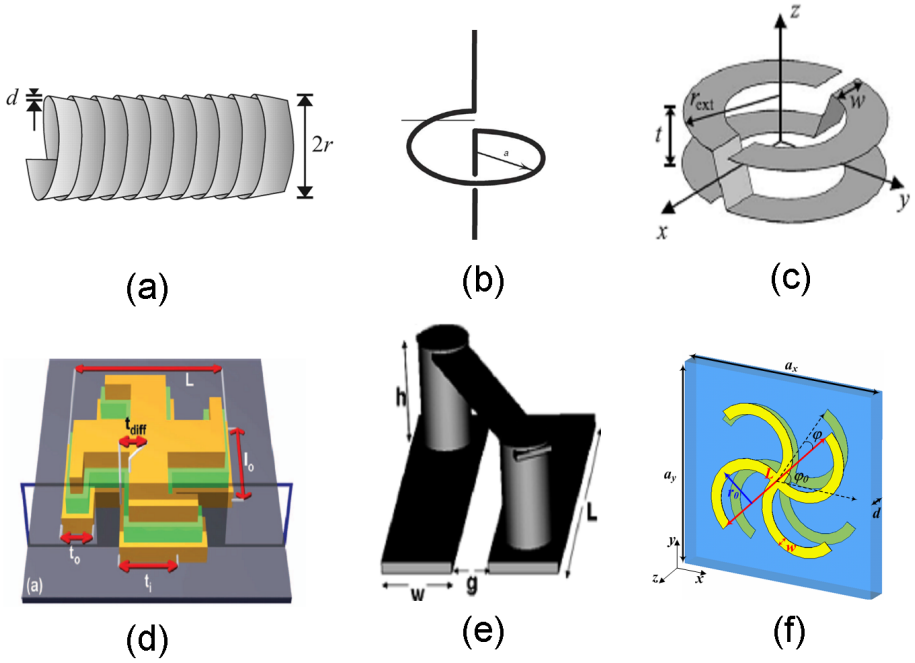

Figure 4.2 Different designs of chiral metamaterials. (a) The twisted "swiss roll" [2]; (b) The canonical helix [3]; (c) The chiral SRR [4]; (d) The bi-layer "swastika" [5]; (e) Dual strips with tilted bridge [6]; (f) Bi-layer rosettes [7]

The idea of making use of helical inclusions in the pioneering work of Tretyakov *et.al.* [111] was further studied [3]. An isotropic chiral metamaterial composed of randomly distributed helical inclusions (shown in Fig. 4.2(b)) was theoretically modeled. The chirality of the proposed metamaterial can be very high. The possibilities of negative refraction and "perfect lensing" [29] were also discussed in this paper. In an isotropic strong chiral medium, the refractive index of one of the circularly polarized waves can be negative. With such a chiral medium slab, it is shown that the circularly polarized wave can be focused with subwavelength resolution [3,117], which works in the similar way as Pendry's "perfect lens" for linearly polarized waves [29]. Later on, the idea of building a bulk chiral metamaterial with a negative index of refraction, by manipulating the parameters of the helical inclusions, was discussed [118]. The refractive properties of uniaxially anisotropic chiral media composed of helices were studied theoretically [119]. The conditions to obtain negative refraction was shown to be easier in chiral metamaterials than in regular metamaterials.

Other than negative refraction, another interesting behavior in strong chiral medium is pointed out [120]. Due to the different refractive indices of LCP and RCP waves, the reflection at the interface between a chiral medium and a nonchiral medium is worth to study. Generally, for one circularly polarized wave, both RCP and LCP waves will be reflected back to the chiral medium. A particularly interesting case is the reflection of a circularly polarized wave at the interface between a strong chiral medium and a perfect electric conductor (PEC). It is shown that one of the reflected wave will be on the same side of the interface normal, or negatively reflected [120]. Based on this property, a circularly polarized wave can be partially focused inside the chiral medium when it is bounded with a PEC mirror.

The reflection between the boundary of vacuum and an isotropic chiral medium is studied theoretically [121]. If the parameters of the chiral medium can be designed such that the wave impedance and the wave vector of the medium are identical to vacuum, the chiral medium could be transparent to one of the circularly polarized waves, i.e., no reflection or refraction is expected at the boundary. In this case, the other circularly polarized wave can be mostly reflected. Based on this idea, a circular polarizing beam splitter is proposed [121].

As we discussed above, the conditions to get negative refraction in a chiral medium are: small ϵ and μ, large κ at resonance. Relatively high losses are associated with the strong resonances. New ideas have been proposed to get negative refraction in different ways. Qiu *et.al.* studied theoretically the wave propagating properties in gyrotropic chiral media, where both ϵ and μ are described by gyrotropic tensors and κ is described by a scalar [122]. Their study showed that negative refraction can be realized with fewer restrictions and all parameters in the ϵ and μ tensors, as well as κ, can be positive when negative refraction occurs. The same group also analyzed the behavior of another kind of chiral media, where the chirality parameter κ is describe by a tensor with non-zero off-diagonal elements while ϵ and μ are described by scalars [123]. The theoretical model showed that negative refraction can be achieved without the requirement of very strong κ due to the gyrotropic parameters.

So far, most of the studies on isotropic chiral metamaterials based on helical inclusions are theoretical. No experimental result on isotropic chiral metamaterials has been reported yet. This is partly due to the difficulty in the fabrication and homogenization of 3D structures.

4.4.2 Experimental realizations

On the other hand, researches on planar chiral metamaterials have also been reported by many groups, both in theories and experiments [5, 7, 124–128]. Planar structures are easier to fabricate than bulk media and there are very interesting behaviors and potential applications in planar structures, such as strong optical activity and circular dichroism in a thin film. Zheludev and coworkers at University of Southampton first reported the optical activity of a planar chiral structure with experiments done in optical regime [124]. The chiral sample is composed of a single layer of a two-dimensional square array of rosette-shaped wires. The patterns are closely arranged and there is coupling between neighboring patterns. A very large rotation of polarization azimuth (greater than 30°) is observed. The rotation is found to be associated with both the arrangement of the patterns and the chirality of the pattern itself.

Later on, the same group studied a bi-layer rosette-shaped structure (see Fig. 4.2(f)) in microwave regime [125]. The patterns are physically separated on each layer and the patterns

on the second layer are rotated by an angle, instead of identical to the first layer. This turned out to give an extremely strong rotation, which, in terms of rotary power per wavelength, is five orders of magnitude larger than a gyrotropic quartz crystal. More recently, this bi-layer structure was proved by experiments to have a negative index of refraction for one of the circularly polarized waves [7].

Meanwhile, the circular dichroism and polarization rotation properties of planar chiral structures, composed of variants of the rosettes, have also been studied by many other groups, both theoretically [126] and experimentally [5,126–128]. Fig. 4.2(d) shows the bi-layer "swastika" design used to realized strong circular dichroism [5]. More recently, negative refractive index of a planar chiral metamaterial, built with arrangements of dual strips connected by a tilted bridge (shown in Fig. 4.2(e)), was demonstrated by parameter retrieval in terahertz frequencies [6].

Actually, the structure on each layer of the bi-layer film does not even have to be chiral to achieve negative refraction. Zhou *et.al.* [8] recently demonstrated strong rotation of polarization azimuth and negative refraction on a bi-layer structures composed of non-chiral cross-wires.

The layout of the proposed structure is shown in Fig. 4.3. A 18×14 array cross-wires is patterned on a double side copper-clad FR-4 board. The transmission and reflection coefficients are measured in the same manner as the chiral SRR experiments. Due to the asymmetric geometry along the propagating direction, the transmission responses for RCP and LCP split into two curves. At the two resonance frequencies of 6.3 GHz and 7.3 GHz, the azimuth rotation and ellipticity reach their maximum values. In the region between two resonance peaks (around 6.9 GHz), which is also the region with low loss and nearly zero dichroism, rotation of polarization can achieve -50° with $\eta \approx 0$ [8].

The mechanism of the resonances for the bi-layer cross-wire pair design can be understood by studying the current density distribution as shown in and 4.4. At the magnetic resonance, the anti-parallel current exists on the top and bottom layer (Fig. 4.4(a)), which is an asymmetric resonance mode. In Fig. 4.4(b), parallel current flows on the two layers, which is a

symmetric resonance mode. The current distribution shows that the bi-layer structures can be regarded as a chiral version of the short wire pairs [37, 38, 129], which has the similar current distributions in the symmetric and asymmetric resonance modes.

The chirality of the design comes from the rotation of the second layer of the cross wires with respect to the first. With an appropriate twist angle, strong chirality can be obtained and the refractive index can go to negative for RCP wave at one resonance and for LCP wave at another resonance. When the twist angle is zero, there would be no chiral behavior, even though the resonances can still be seen [8].

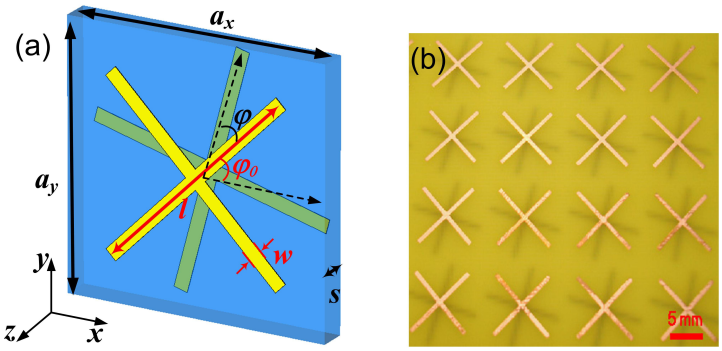

Figure 4.3 (a) Schematic representation of one unit cell of the cross-wire structure. (b) Photograph of one side of a fabricated microwave-scale cross-wire sample. The geometry parameters are given by $a_x = a_y = 15$mm, $l = 14$ mm, $w = 1$ mm, $s = 1.6$ mm, $\phi_0 = 45°$, $\phi = 30°$. (Adapted from Ref. [8])

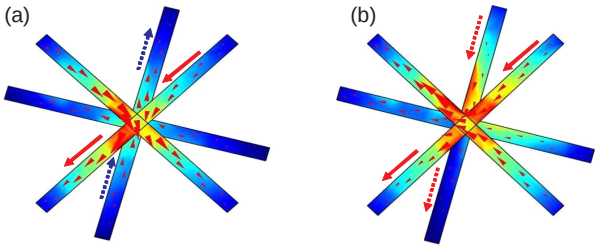

Figure 4.4 The simulated current density distribution for the right circularly polarized EM wave at 6.5 GHz (a) and for the left circularly polarized EM wave at 7.5 GHz (b). (Adapted from Ref. [8])

4.5 Nonplanar chiral metamaterial based on chiral SRRs

Although many proposed models for chiral metamaterials are three-dimensional (3D), most of the experimental results reported so far are planar structures (Fig. 4.2(d)-(f)). Planar structures are easier to fabricate and they have strong optical activity and circular dichroism. Bi-layer rosette-shaped [7, 125] and cross wires [8] structures were recently studied in the microwave regime. While the thicknesses of the planar chiral metamaterials in the wave propagation direction are much smaller than the working wavelengths, the size of the patterns in plane is usually comparable with half-wavelength [7,8]. Moreover, in effective medium theory, homogeneity of a metamaterial is assumed to calculate the macroscopic parameters. However, some of the proposed planar chiral metamaterials are not symmetric in the propagation direction [6]. This causes differences in transmission and reflection from opposite directions and ambiguity in the calculation of effective parameters. So these planar chiral metamaterials are not suitable to build 3D bulk chiral metamaterials.

In this section we demonstrate experimentally and numerically the negative refraction in a non-planar chiral metamaterials. We observe strong cross coupling between the magnetic and electric fields by the two coupled split-ring resonators (SRRs) on two sides of the substrates at the chiral resonance frequency. The negative refractive index of chiral metamaterials arise from this strong chirality. Compared with other planar chiral structures, our non-planar chiral metamaterialsis symmetric along the propagation direction and much smaller than the working wavelength in all dimensions. So it is a good candidate for isotropic 3D chiral metamaterials [130].

4.5.1 The chiral SRR design

The chiral structure of our studies is formed by two identical SRRs separated by a dielectric substrate and interconnected by vias, as shown in Fig. 4.5(a). The chiral SRRs are arranged in square lattices to form a 2D slab. Fig. 4.5(b) shows a unit cell of such a 2D array. In this arrangement, each of the chiral SRRs is shared by the two neighboring cells. When the structure is excited by external field, both magnetic dipole and electric dipole exist and they

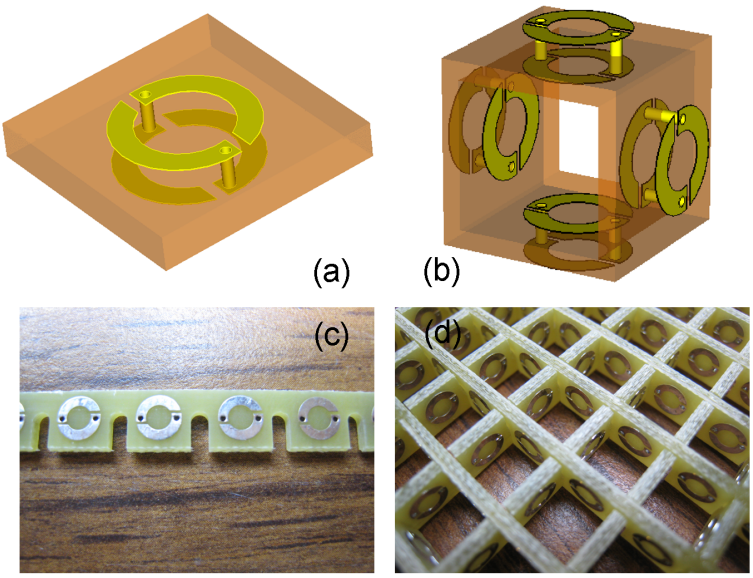

Figure 4.5 (a) The structure of the chiral SRR. (b) A unit cell of the 2D chiral metamaterial used in simulation. (c) The chiral SRRs are fabricated on PCBs and cut into strips (d) The strips are interlocked to form the chiral metamaterial slab.

are both parallel to the axis of the SRRs. While the induced current around in the SRRs gives the magnetic dipole, electric charges accumulate on the two SRRs with opposite signs, which introduce a strong electric field between the top and bottom SRRs and give the electric dipole in the same direction as the magnetic dipole(see Fig. 4.6). A electric dipole can excite a magnetic dipole in a similar way.

This chiral SRR design (shown in Fig. 4.2(c)) was proposed [4, 131, 132] to develop 3D isotropic chiral metamaterials [4]. By arranging the chiral SRRs in cubic (fcc) Bravais lattices, a bi-isotropic medium can be obtained. By calculating the susceptibility parameters, including the chiral parameter κ, by Lorentz local field theory, the medium is shown to provide negative refraction over a frequency band. We study a single layer of the CM made of chiral SRRs and demonstrate both numerically and experimentally the strong optical activity and circular dichroism, and negative refraction. This is an important step toward the design and characterizations of 3D isotropic chiral metamaterials.

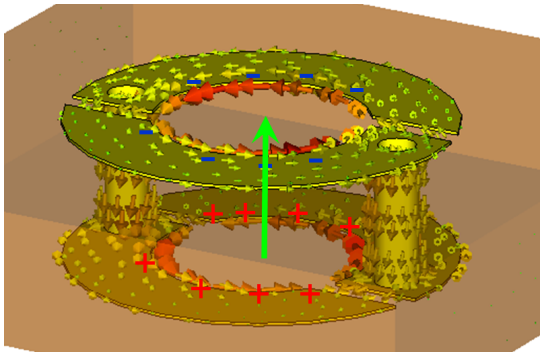

Figure 4.6 The surface current distribution of the SRR near resonance. The circulating current forms a magnetic dipole, causes the opposite charge accumulation on the bottom SRR (+) and the top SRR (-) and forms an extra electric dipole (see green straight arrow).

4.5.2 Experimental method

The chiral structures are fabricated on the two sides of FR-4 printed circuit boards (PCBs), with a relative dielectric constant of $\epsilon_r = 3.76$ with loss tangent 0.0186 and thickness of 1.6 mm. The metal structures are built on copper with a thickness of 36 μm. The SRRs are 2-gap split rings with an identical gap width of 0.3 mm. The inner radius of the rings is 1.25 mm and the outer radius is 2.25 mm. The SRRs on opposite sides of the board are connected by vias with a diameter of 0.5 mm. The distance between adjacent rings is 8 mm. The sample is fabricated by 50 strips with 26 cells each, which are then interlocked to form a slab of size 208 mm $\times$ 208 mm of the chiral metamaterial. A fabricated strip of SRRs is shown in Fig. 4.5(c) and the chiral metamaterial slab is shown in Fig. 4.5(d).

The transmission and reflection measurements are done with a vector network analyzer (Agilent E8364B) in our lab. A pair of standard gain horn antennas are used as transmitter and receiver, see Fig. 4.7. The signals from these horn antennas are linearly polarized, so the linear transmission coefficients, T_{xx}, T_{xy}, T_{yx} and T_{yy} are measured, where the first subscript indicates the transmitted field polarization ($x-$ or $y-$polarized) and the second subscript indicates the incident field polarization. The circular transmission coefficients, T_{++}, T_{-+}, T_{+-} and T_{--}, where the first subscript indicates the transmitted field polarization ($\pm$, RCP/LCP)

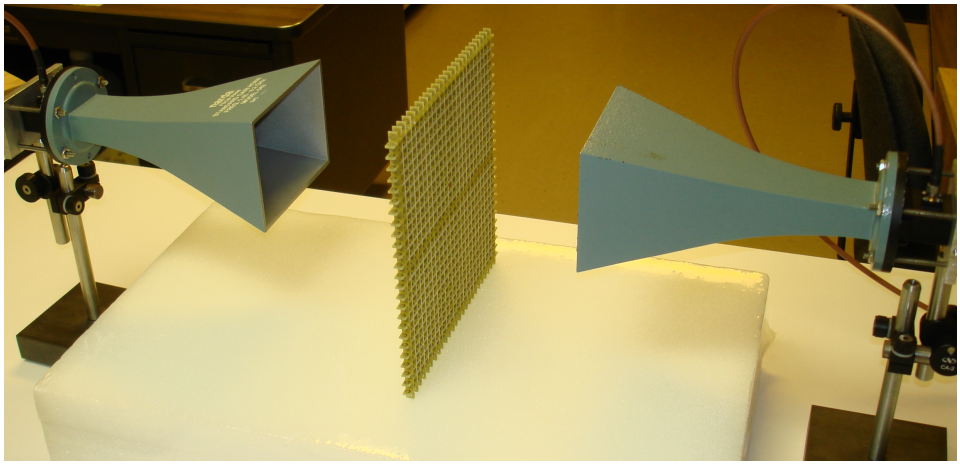

Figure 4.7 The transmission and reflection coefficients of the chiral metamaterial slab is measured by a pair of horn antennas served as transmitter and receiver. The cables on the horn antennas are connected to a vector network analyzer (not shown).

and the second subscript indicates the incident field polarization, are converted from the linear transmission coefficients using the following equation.

$$\begin{pmatrix} T_{++} & T_{+-} \\ T_{-+} & T_{--} \end{pmatrix}$$
$$= \frac{1}{2} \begin{pmatrix} (T_{xx} + T_{yy}) + i(T_{xy} - T_{yx}) & (T_{xx} - T_{yy}) - i(T_{xy} + T_{yx}) \\ (T_{xx} - T_{yy}) + i(T_{xy} + T_{yx}) & (T_{xx} + T_{yy}) - i(T_{xy} - T_{yx}) \end{pmatrix} \tag{4.19}$$

A similar expression exists for the circular reflection coefficients R_{++}, R_{-+}, R_{+-} and R_{--}.

4.5.3 Results and discussion

Fig. 4.8(a) and (b) shows the simulated and measured transmission coefficients T_{++} and T_{--}, as well as the reflection coefficients R_{+-} and R_{-+}, as a function of frequency. There is obvious difference (about 5 dB) in T_{++} and T_{--} around the resonance. The reflection coefficients $R_{+-} = R_{-+} = R$, since the impedances for RCP and LCP waves are identical. The cross coupling transmission T_{-+} and T_{+-} are negligible and they are not shown. While the simulation curves are smooth off the resonance, there are a lot of noise in the experimental curves. This is mainly due to the scattering from the surroundings and multiple reflections

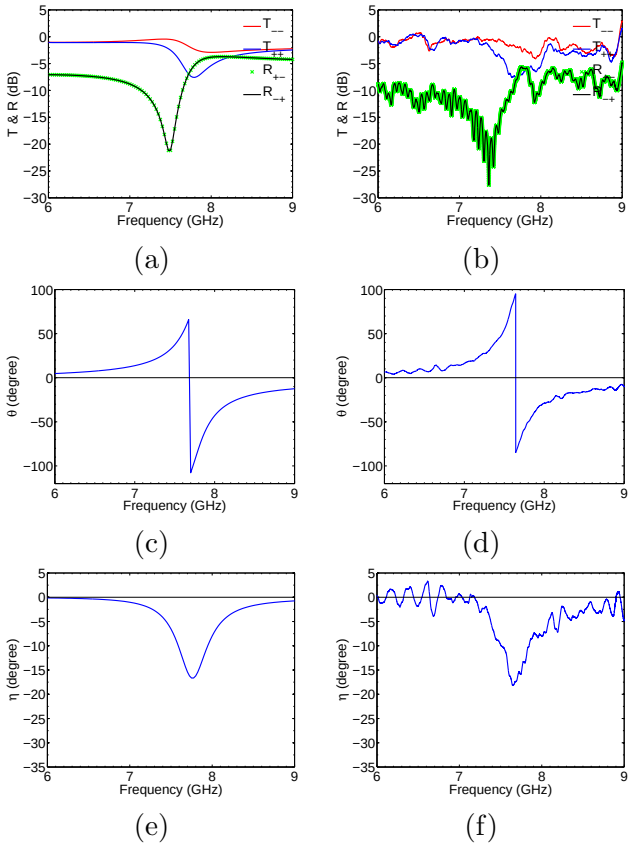

Figure 4.8 From top to bottom, the transmission and reflection amplitudes for LCP and RCP waves, the azimuth rotation angle for linearly polarized waves, and the ellipticity. Simulation results are shown on left and experiment results are shown on right.

between the horn antennas and the sample. Also, the resonance frequency in experiment is about 0.1 GHz lower than the resonance frequency in simulation. This is not surprising since the parameters, particularly the dielectric constant of the PCB, may not be accurate in our frequency range. The azimuth rotation θ, and the ellipticity η, are calculated based on the transmission data and presented in Fig. 4.8(c)-(f). At the resonance, the azimuth rotation reaches a maximum of around $-100°$. Meanwhile, the ellipticity is also the largest ($-17°$), meaning a linearly polarized wave is strongly distorted and becomes elliptical.

The retrieved effective parameters of the chiral metamaterial are shown in Fig. 4.9. We see that the effective index of refraction for RCP wave (Fig. 4.9(a) and (b)) shows strong response at the resonance and goes negative above the resonance while the index of refraction

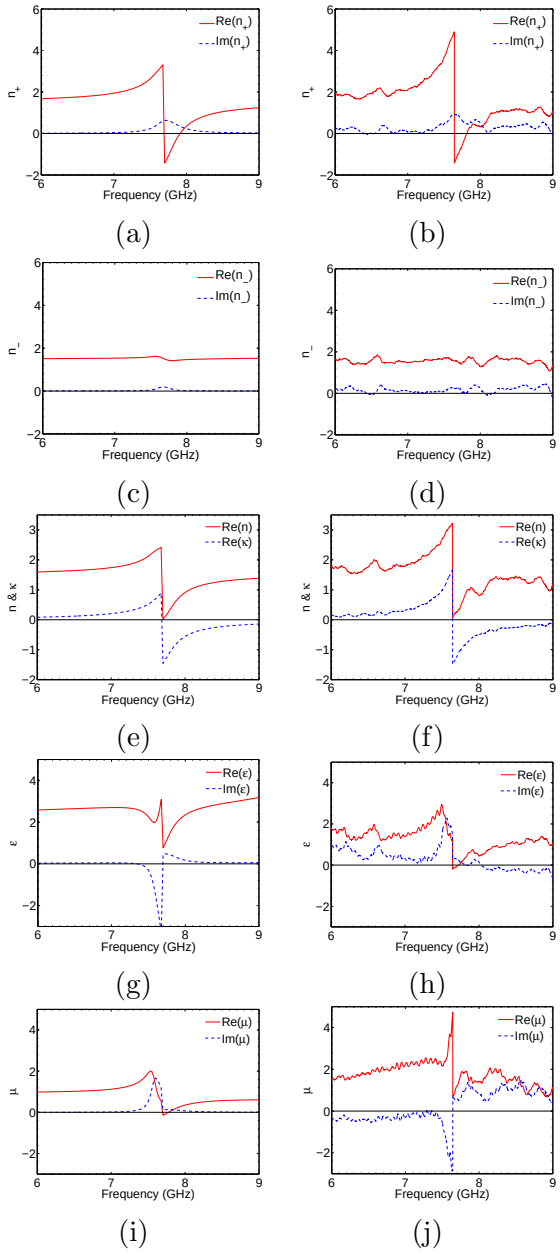

Figure 4.9 The retrieved effective parameters of the chiral metamaterial. The figures from top to bottom are the index of refraction for the two circularly polarized waves n_+ and n_-, the effective index of refraction n together with the chiral parameter κ, the effective relative permittivity ϵ and relative permeability μ. Simulation results are shown on left and experiment results are shown on right.

for LCP wave (Fig. 4.9(c) and (d)) changes only slightly and is positive in all the frequency range. The negative index here is due to a relatively strong chirality κ, and a small value of n at the resonance (Fig. 4.9(e) and (f)). Although there is some discrepancies in simulated and experimental ϵ and μ (Fig. 4.9(g)-(j)), it is obvious that, ϵ and μ are not both negative, which is the signature of conventional negative index metamaterials. The retrieval results show that the negative refraction comes from a strong chirality of the structure, instead of the double-negative (ϵ and μ) in conventional metamaterials. The negative index has a minimum of around 1.7 with a figure of merit about 2. The peak of the imaginary part of the index of refraction comes from the strong absorption in the PCB substrate at the resonance. The loss could be reduced significantly when a low-loss substrate can be used.

In summary, the electromagnetic properties of the non-planar chiral metamaterial composed of chiral SRRs have been studied. Very strong optical activity, as well as circular dichroism can be achieved with the metamaterial. Moreover, negative index of refraction is obtained by both numerical simulations and experimental measurement. A 3D bulk medium can be fabricated by stacking layers of this chiral metamaterial together. Eventually 3D isotropic chiral metamaterials, with negative refraction due to chirality, can be obtained.

4.6 A microwave absorber made from chiral metamaterial

4.6.1 Loss problem and metamaterial absorbers

Since most proposed metamaterials are metallic resonant structures and rely on strong resonances, losses are inevitable. The existence of losses deteriorates the performance of potential devices such as superlenses [29]. Different ways to reduce the losses have been studied, including the use of low-loss materials, the optimization of designs [133] and the use of gain materials to compensate losses [134].

Instead of trying to reduce the losses, very recently, ideas have been proposed to build resonant absorbers with metamaterials [135–138], as well as other metallic nanostructures [139]. The absorption is defined as $A(\omega) = 1 - R(\omega) - T(\omega)$, where $A(\omega)$, $R(\omega)$, and $T(\omega)$ are the absorption, the reflection, and the transmission as functions of frequency ω, respectively. It

is straightforward to get the two design principles to make the absorption as close to unity as possible: minimize $R(\omega)$ and minimize $T(\omega)$. To minimize the reflection, we can tune the parameters of the metamaterial to get the effective ϵ and μ matched so that the impedance of the metamaterial $z = \sqrt{\mu/\epsilon}$ is equal to one and matched to the free space. Thus, the reflection can in principle be eliminated. To minimize the transmission, the metamaterial needs to be designed so that the imaginary parts of ϵ and μ are as large as possible since they correspond to the loss in the metamaterial. Although it is difficult to get the transmission eliminated by one single layer of the metamaterial, there are ways to achieve unit absorption. The first is to use multiple layers of such metamaterial films to eliminate the transmission [135, 138]; the second is to use a ground plane to reflect the transmitted wave back [137, 139]. These two approaches have their advantages and disadvantages. The first approach can obtain in principle perfect absorption at the resonance peak, with the sacrifice of increasing thickness. The second approach can give a very thin absorber, but the absorption may not be perfect.

Most of the proposed metamaterial absorbers are composed of conducting electric resonators on two sides of a dielectric substrate [135, 136, 138]. The electric response can be obtained from the excitation of the electric resonators by the electric field, and the magnetic response is provided by the anti-parallel currents on the two sides of the substrate [40, 129]. These absorbers depend strongly on the polarization of the incident waves [135, 136] as well as the incident angle. They work only for one polarization at normal incidence and the absorption drops rapidly for off-normal-incidence cases. The absorber in Ref. [138], which is composed of paired metallic rods symmetric on two sides of a substrate, covers a wider angle but only works for one polarization. The design of periodic metallic strips with a ground plate [139] can have an absorption of over 80% at 70°, but is still limited to one particular polarization. In Ref. [137], the metamaterial absorber, composed of split-ring-shaped electric resonators, operates over a wide range of incidence angles for both transverse electric (TE) and transverse magnetic (TM) waves. However, the electric resonators in the absorber are not symmetric and still have azimuthal dependence.

4.6.2 The chiral metamaterial absorber

Here we propose a different type of resonant absorbers that are made of chiral metamaterials. The chiral metamaterial absorber is shown, by both numerical simulations and experimental measurements, to be angle and polarization independent. Near-perfect absorption can be achieved at the resonance. Moreover, the proposed absorber has a thickness of merely 1/5 of the working wavelength λ. Although the modeling and experiments are done in microwave frequencies, the absorber can be scaled to find applications at higher frequency regimes [140].

Similar to conventional metamaterials, chiral metamaterials require strong resonances to get a large κ, thus losses are also associated with chiral metamaterials. In microwave experiments, the major loss is shown to be a dielectric loss due to the lossy substrates used. The loss can be reduced significantly by using low-loss substrates. On the other hand, resonant absorbers can be made with chiral metamaterials.

The chiral metamaterial in this study is based on the chiral SRR structures [130]. The chiral metamaterial has been shown to have negative refraction due to strong chirality at the resonance frequency [130]. Meanwhile, significant loss is associated with the resonance, which, shown by numerical simulations, is mainly due to dielectric loss in the lossy FR-4 board. The loss can thus be reduced by choosing substrates with a smaller dissipation factor. On the other hand, a metamaterial absorber can be made out of the current structure.

A chiral metamaterial absorber can be build from the chiral metamaterial slab, backed with a ground copper plate, and covered with a dielectric plate, see Fig. 4.10. For normal incidence, the incident wave is rotated by an angle θ when it reaches the ground plane; when the wave is reflected back to the chiral metamaterial, it is rotated by the same angle θ, but in the opposite direction. Therefore, the polarization is preserved after the reflection, due to the reciprocity of the metamaterial. In the case of oblique incidence, part of the reflected wave is transformed. Simulations have shown that the polarization transformation is less than 3% an even the incident angle is 85° off normal.

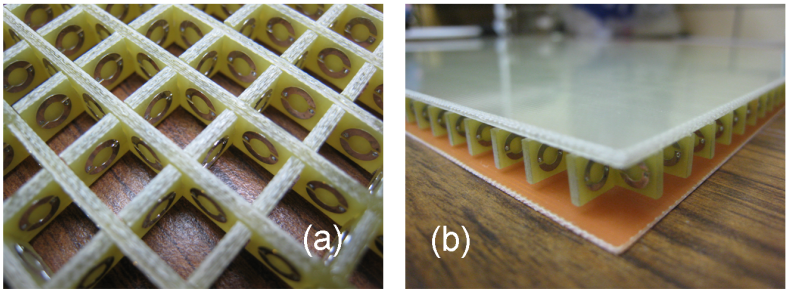

Figure 4.10 (a) The chiral metamaterial slab. (b) The fabricated microwave absorber.

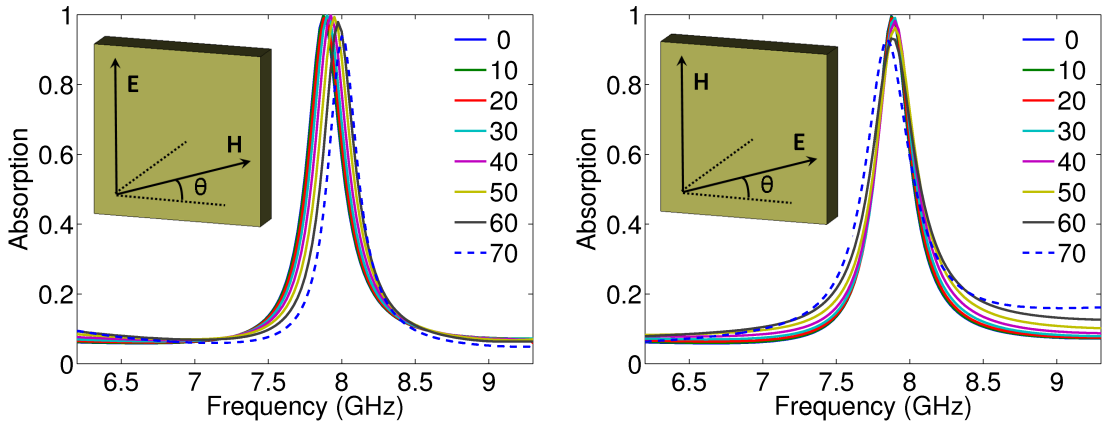

Figure 4.11 The simulation results of absorption at different angles θ for (a) TE polarization and (b) TM polarization. Insets illustrate the two polarizations and the angle θ.

4.6.3 Results and discussion

The numerical simulations are done in CST Microwave studio. With the help of unit-cell boundaries, an infinitely large slab of the absorber is simulated. With the ground plane in the back, the transmission is eliminated and the absorption is calculated by $A_E = 1 - R_{EE} - R_{HE}$ for TE polarization and $A_H = 1 - R_{HH} - R_{EH}$ for TM polarization, where the subscript E indicates TE polarization and H indicates TM polarization. The term R_{EE} means the reflection coefficient of a TE wave from an incident TE wave and R_{HE} means the reflection coefficient of a TM wave from an incident TE wave. The absorption is calculated for different incident angles, as shown in Fig. 4.11(a) for TE polarization and Fig. 4.11(b) for TM polarization. For TE polarization, the absorption is almost unity at normal incidence and remains above 98% until 60°. The peak absorption drops for large incident angles but is still above 90% even when the incidence angle is 70°. When taking into account the small shift in the center frequency (1.25% from 0° to 70°), the absorption at the peak frequency of normal-incidence case is still more than 40% (60%) at 70° (60°). For TM polarization, the absorption is above 90% for all incident angles and the center frequency shift is less than 1%. Moreover, since the metamaterial slab is uniaxial in plane, the absorber has no azimuthal dependence for either polarization. All these results show that the proposed design can be used as a near perfect absorber.

Experiments have also been done to test the absorption behavior of the fabricated sample. A vector network analyzer (Agilent E8364B) and a pair of standard gain horn antennas are used to measure the reflection coefficient from the sample. The EM wave from the horn antenna is linearly polarized. By changing the orientation and the angle of the antennas, the reflection coefficient for both TE and TM polarizations at different incident angles can be measured. The reflection from a metal plate without the absorber is used for normalization. The absorption is then calculated and shown in Figs. 4.12(a) and 4.12(b). The absorption peaks at resonance are smaller than the simulation results. This is partly due to the fact that the actual dissipation factor of the PC boards may be different from the one used in simulations. The fabrication imperfection contributes to the discrepancies as well. The measured absorption off resonance

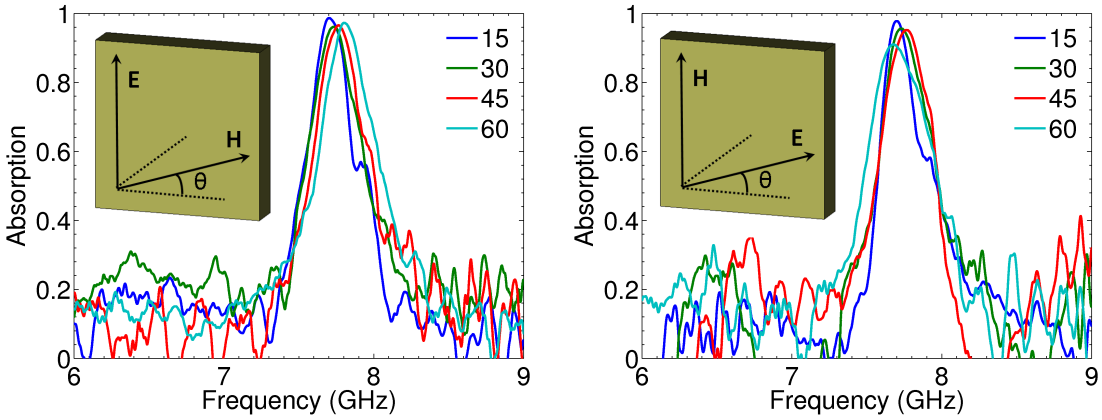

Figure 4.12 The experimental results of absorption at different angles θ for (a) TE polarization and (b) TM polarization. Insets illustrate the two polarizations and the angle θ.

is generally higher than the simulation results and has many small oscillations. This is caused by the scattering from imperfections in the fabricated structure and the scattering between the horn antennas due to their relatively large aperture. In spite of these discrepancies, the experimental measurements agree with the simulation results that high absorption can be obtained at the resonance for a wide range of incident angles for different polarizations. With these nice absorption properties, the proposed metamaterial absorber is still relatively thin, with a thickness of 1/5 of the working wavelength. The strong chirality of the metamaterial comes from the cross coupling between electric and magnetic field, as has been pointed out. Due to this cross-coupling effect and the nonplanar arrangement of the resonators, the resonance can be excited by different polarizations at a wide range of incident angles.

The idea to fabricate microwave absorbers with chiral media can be dated back to 1980s [141]. The interest is due to the extra macroscopic parameter κ other than ϵ and μ. The authors [141] believed that κ can give extra flexibility in the design of phase-matched microwave absorbers and thus provide improvement to the performance. A debate started soon after these publications, concerning whether κ can really affect the impedance and enhance the absorption [142, 143]. Meanwhile, there is not much experimental support for the superiority of chiral absorbers. A discussion at the conference Bianisotropics'97 concluded that chirality

does not lead to superior absorption [144]. Later experimental results with chiral and achiral resonant structures show that, resonance structures, no matter chiral or not, in a lossy host can significantly enhance the absorption at the resonance frequency and chirality does not play a role in the enhancement of absorption [144]. The superior absorption properties of our design are due to the very strong resonance that can be excited by both electric and magnetic fields, and the compact size of the resonators.

In summary, the absorption properties of a resonant absorber made from chiral metamaterials are studied. The absorber is shown, by both numerical simulations and experimental measurements, to be working for a very wide angle. The absorber is also independent of polarizations and azimuthal angles. Due to the compact size of the resonators, the proposed absorber has a very small thickness (about 1/5 of the center wavelength). All those features make the proposed design a perfect absorber. By scaling the parameters, the design in microwave can be applied to higher frequency regimes.

4.7 Conclusion

In conclusion, we have briefly reviewed the history of metamaterials, from theoretical proposals to experimental realizations in GHz, THz and optical regimes. While the conventional metamaterials require negative ϵ and μ simultaneously to achieve negative index of refraction, chiral metamaterials offer an alternative and simpler route. We have studied the wave propagation properties in chiral metamaterials and showed that negative index and consequently negative refraction can be realized in chiral metamaterials with a strong chirality while neither ϵ nor μ negative is required. We have developed a retrieval procedure, adopting uniaxial bi-isotropic model to calculate the effective parameters of the chiral metamaterials. We have reviewed the progresses in the chiral metamaterials field, both theoretically and experimentally. We have introduced our new designs, numerical calculations and experimental measurements of chiral metamaterials. We show that very strong chiral behaviors such as optical activity and circular dichroism can be observed. Negative refraction for circularly polarized waves can be obtained with various designs. Losses are associated with the highly resonant structures. We

have demonstrated with experimental studies that chiral metamaterials can be used to create resonant absorbers with very good performance.

CHAPTER 5. Conclusions

The research in photonic crystals and metamaterials communities is still growing rapidly and new phenomena are being discovered. These discoveries have potential applications in many areas from radio frequencies, THz to visible frequencies. This thesis describes my graduate studies in the field.

As the first part, surface modes and wave guiding properties of 2D photonic crystals are studied. With surface defects, a photonic crystal could support surface modes that are localized on the surface of the crystal, with mode frequencies within the band-gap. With line defects, a photonic crystal could allow the propagation of electromagnetic waves along the channels. Photonic crystals with different surface layers were designed to support surface modes. Attenuated total reflection technique was used to detect the surface modes. The surface mode dispersion was traced experimentally. Photonic crystal waveguides with different terminations were studied. It was shown that the waveguiding properties can be improved with the help of surface modes. Enhanced transmission and directed beaming from a photonic crystal waveguide of subwavelength aperture was demonstrated. The optical conductance of a photonic crystal waveguide was also studied experimentally. Due to the discrete waveguide modes that are allowed to propagate inside the waveguide, the optical conductance changes with the waveguide width in a staircase manner.

The last decade has seen great progress in metamaterial research. Metamaterials are generally composed of artificial structures with sizes one order smaller than the wavelength and can be approximated as effective media. Effective macroscopic parameters such as electric permittivity ϵ, magnetic permeability μ are used to characterize the wave propagation in metamaterials. The fundamental structures of the metamaterials affect strongly their macro-

scopic properties. By designing the fundamental structures of the metamaterials, the effective parameters can be tuned and different electromagnetic properties can be achieved.

One important aspect of metamaterial research is to get artificial magnetism. Metallic split-ring resonators (SRRs) and variants are widely used to build magnetic metamaterials with effective $\mu < 1$ or even $\mu < 0$. In the next part, varactor based nonlinear SRRs were built and modeled to study the nonlinearity in magnetic metamaterials. The nonlinear SRR has a typical SRR design and we have soldered in the gap of the SRR a commercial varactor diode. Dynamic tunability, hysteresis, and bistable behavior in nonlinear SRRs were demonstrated experimentally. Tunability of the resonance frequency was completed dynamically by increasing the incident power of the vector network analyzer. We have introduced different nonlinear designs and observed experimentally that the resonance frequency can decrease or increase by increasing the incident power. A theoretical model was given to explain the observed nonlinear effects. The mutual coupling between two SRRs at different input power levels were also studied. The magnetic response of a single SRR and the mutual coupling between SRRs are important in understanding and modeling nonlinear magnetic metamaterials.

Negative refractive index n is one of the major target in the research of metamaterials. Negative n can be obtained with a metamaterial with both ϵ and μ negative. As an alternative, negative index for one of the circularly polarized waves could be achieved with metamaterials having a strong chirality κ. A retrieval procedure, adopting uniaxial bi-isotropic model has been developed to calculate the effective parameters of the chiral metamaterials. Designs, numerical calculations and experimental measurements of chiral metamaterials were presented. Very strong chiral behaviors such as optical activity and circular dichroism can be observed. Negative index for circularly polarized waves can be obtained with various designs. Chiral SRR structures were studied in particular and negative index was achieved. It is also shown, with chiral SRR design, that chiral metamaterials can be used to create resonant absorbers with very good performance.

BIBLIOGRAPHY

[1] D. R. Smith, J. B. Pendry, and M. C. K. Wiltshire. Metamaterials and Negative Refractive Index. *Science*, 305(5685):788–792, 2004.

[2] J. B. Pendry. A Chiral Route to Negative Refraction. *Science*, 306(5700):1353–1355, 2004.

[3] S. Tretyakov, A. Sihvola, and L. Jylh. Backward-wave regime and negative refraction in chiral composites. *Photonics Nanostruct.: Fundam. Appl.*, 3(2-3):107 – 115, 2005.

[4] L. Jelinek, R. Marqués, F. Mesa, and J. D. Baena. Periodic arrangements of chiral scatterers providing negative refractive index bi-isotropic media. *Phys. Rev. B*, 77(20):205110, 2008.

[5] M. Decker, M. W. Klein, M. Wegener, and S. Linden. Circular dichroism of planar chiral magnetic metamaterials. *Opt. Lett.*, 32(7):856–858, 2007.

[6] S. Zhang, Y. Park, J. Li, X. Lu, W. Zhang, and X. Zhang. Negative refractive index in chiral metamaterials. *Phys. Rev. Lett.*, 102(2):023901, 2009.

[7] E. Plum, J. Zhou, J. Dong, V. A. Fedotov, T. Koschny, C. M. Soukoulis, and N. I. Zheludev. Metamaterial with negative index due to chirality. *Phys. Rev. B*, 79(3):035407, 2009.

[8] J. Zhou, J. Dong, B. Wang, T. Koschny, M. Kafesaki, and C. M. Soukoulis. Negative refractive index due to chirality. *Phys. Rev. B*, 79(12):121104, 2009.

[9] E. Yablonovitch. Inhibited spontaneous emission in solid-state physics and electronics. *Phys. Rev. Lett.*, 58(20):2059–2062, May 1987.

[10] S. John. Strong localization of photons in certain disordered dielectric superlattices. *Phys. Rev. Lett.*, 58(23):2486–2489, Jun 1987.

[11] K. M. Ho, C. T. Chan, and C. M. Soukoulis. Existence of a photonic gap in periodic dielectric structures. *Phys. Rev. Lett.*, 65(25):3152–3155, Dec 1990.

[12] E. Yablonovitch, T. J. Gmitter, and K. M. Leung. Photonic band structure: The face-centered-cubic case employing nonspherical atoms. *Phys. Rev. Lett.*, 67(17):2295–2298, Oct 1991.

[13] J. D. Joannopoulos, R. D. Meade, and J. N. Winn. *Photonic Crystals: Molding the Flow of Light*. Princeton University Press, 1995.

[14] K.M. Ho, C.T. Chan, C.M. Soukoulis, R. Biswas, and M. Sigalas. Photonic band gaps in three dimensions: New layer-by-layer periodic structures. *Solid State Commun.*, 89(5):413 – 416, 1994.

[15] C. M. Soukoulis, editor. *Photonic Band Gap Materials*. Springer, 1996.

[16] P. Russell. Photonic Crystal Fibers. *Science*, 299(5605):358–362, 2003.

[17] E. Cubukcu, K. Aydin, E. Ozbay, S. Foteinopoulou, and C. M. Soukoulis. Electromagnetic waves: Negative refraction by photonic crystals. *Nature*, 423:604–605, 2003.

[18] H. Kosaka, T. Kawashima, A. Tomita, M. Notomi, T. Tamamura, T. Sato, and S. Kawakami. Superprism phenomena in photonic crystals. *Phys. Rev. B*, 58(16):R10096–R10099, Oct 1998.

[19] C. M. Soukoulis, M. Kafesaki, and E. N Economou. Negative-index materials: New frontiers in optics. *Adv. Mat.*, 18:1941–1952, 2006.

[20] C. M. Soukoulis, S. Linden, and M. Wegener. PHYSICS: Negative Refractive Index at Optical Wavelengths. *Science*, 315(5808):47–49, 2007.

[21] J. B. Pendry, A. J. Holden, D. J. Robbins, and W.J. Stewart. Magnetism from conductors and enhanced nonlinear phenomena. *IEEE Trans. Microwave Theory Tech.*, 47:2075, Nov 1999.

[22] A. Alu, N. Engheta, A. Erentok, and R.W. Ziolkowski. Single-negative, double-negative, and low-index metamaterials and their electromagnetic applications. *IEEE Antennas and Propagation Magazine*, 49(1):23–36, 2007.

[23] V. G. Veselago. The electrodynamics of substances with simultaneously negative values of ϵ and μ. *Sov. Phys. Usp.*, 10:509–514, 1968.

[24] J. D. Jackson. *Classical electrodynamics*. Wiley; 3rd edition, 1998.

[25] R. Marqus, F. Martn, and M. Sorolla. *Metamaterials with Negative Parameters: Theory, Design and Microwave Applications*. Wiley, 2008.

[26] J B Pendry, A J Holden, D J Robbins, and W J Stewart. Low frequency plasmons in thin-wire structures. *J. Phys.: Condens. Matter*, 10(22):4785–4809, 1998.

[27] D. R. Smith, Willie J. Padilla, D. C. Vier, S. C. Nemat-Nasser, and S. Schultz. Composite medium with simultaneously negative permeability and permittivity. *Phys. Rev. Lett.*, 84(18):4184–4187, May 2000.

[28] R. A. Shelby, D. R. Smith, and S. Schultz. Experimental verification of a negative index of refraction. *Science*, 292(5514):77–79, 2001.

[29] J. B. Pendry. Negative refraction makes a perfect lens. *Phys. Rev. Lett.*, 85(18):3966–3969, Oct 2000.

[30] J. B. Pendry, D. Schurig, and D. R. Smith. Controlling Electromagnetic Fields. *Science*, 312(5781):1780–1782, 2006.

[31] D. Schurig, J. J. Mock, B. J. Justice, S. A. Cummer, J. B. Pendry, A. F. Starr, and D. R. Smith. Metamaterial Electromagnetic Cloak at Microwave Frequencies. *Science*, 314(5801):977–980, 2006.

[32] T. J. Yen, W. J. Padilla, N. Fang, D. C. Vier, D. R. Smith, J. B. Pendry, D. N. Basov, and X. Zhang. Terahertz Magnetic Response from Artificial Materials. *Science*, 303(5663):1494–1496, 2004.

[33] S. Linden, C. Enkrich, M. Wegener, J. Zhou, T. Koschny, and C. M. Soukoulis. Magnetic Response of Metamaterials at 100 Terahertz. *Science*, 306(5700):1351–1353, 2004.

[34] N. Katsarakis, G. Konstantinidis, A. Kostopoulos, R. S. Penciu, T. F. Gundogdu, M. Kafesaki, E. N. Economou, T. Koschny, and C. M. Soukoulis. Magnetic response of split-ring resonators in the far-infrared frequency regime. *Opt. Lett.*, 30(11):1348–1350, 2005.

[35] C. Enkrich, M. Wegener, S. Linden, S. Burger, L. Zschiedrich, F. Schmidt, J. F. Zhou, T. Koschny, and C. M. Soukoulis. Magnetic metamaterials at telecommunication and visible frequencies. *Phys. Rev. Lett.*, 95(20):203901, Nov 2005.

[36] S. Zhang, W. Fan, N. C. Panoiu, K. J. Malloy, R. M. Osgood, and S. R. J. Brueck. Experimental demonstration of near-infrared negative-index metamaterials. *Phys. Rev. Lett.*, 95(13):137404, 2005.

[37] G. Dolling, C. Enkrich, M. Wegener, J. F. Zhou, C. M. Soukoulis, and S. Linden. Cut-wire pairs and plate pairs as magnetic atoms for optical metamaterials. *Opt. Lett.*, 30(23):3198–3200, 2005.

[38] V. M. Shalaev, W. Cai, U. K. Chettiar, H Yuan, A. K. Sarychev, V. P. Drachev, and A. V. Kildishev. Negative index of refraction in optical metamaterials. *Opt. Lett.*, 30(24):3356–3358, 2005.

[39] G. Dolling, C. Enkrich, M. Wegener, C. M. Soukoulis, and S. Linden. Simultaneous Negative Phase and Group Velocity of Light in a Metamaterial. *Science*, 312(5775):892–894, 2006.

[40] G. Dolling, M. Wegener, C. M. Soukoulis, and S. Linden. Negative-index metamaterial at 780 nm wavelength. *Opt. Lett.*, 32(1):53–55, 2007.

[41] J. Valentine, S. Zhang, T. Zentgraf, E. Ulin-Avila, D. A. Genov, G. Bartal, and X. Zhang. Three-dimensional optical metamaterial with a negative refractive index. *Nature*, 455:376–379, 2008.

[42] I. V. Lindell, S. A. Tretyakov, K. I. Nikoskinen, and S. Ilvonen. BW media - media with negative parameters, capable of supporting backward waves. *Microwave Opt. Technol. Lett.*, 31:129–133, 2001.

[43] D. R. Smith and D. Schurig. Electromagnetic wave propagation in media with indefinite permittivity and permeability tensors. *Phys. Rev. Lett.*, 90(7):077405, Feb 2003.

[44] D. R. Smith, P. Kolinko, and D. Schurig. Negative refraction in indefinite media. *J. Opt. Soc. Am. B*, 21(5):1032–1043, 2004.

[45] R. Wangberg, J. Elser, E. E. Narimanov, and V. A. Podolskiy. Nonmagnetic nanocomposites for optical and infrared negative-refractive-index media. *J. Opt. Soc. Am. B*, 23(3):498–505, 2006.

[46] M. G. Silveirinha, P. A. Belov, and C. R. Simovski. Subwavelength imaging at infrared frequencies using an array of metallic nanorods. *Phys. Rev. B*, 75(3):035108, 2007.

[47] J. Yao, Z. Liu, Y. Liu, Y. Wang, C. Sun, G. Bartal, A. M. Stacy, and X. Zhang. Optical Negative Refraction in Bulk Metamaterials of Nanowires. *Science*, 321(5891):930–, 2008.

[48] A. A. Zharov, I. V. Shadrivov, and Y. S. Kivshar. Nonlinear properties of left-handed metamaterials. *Phys. Rev. Lett.*, 91(3):037401, Jul 2003.

[49] I. V. Shadrivov, A. A. Zharov, and Y. S. Kivshar. Second-harmonic generation in nonlinear left-handed metamaterials. *J. Opt. Soc. Am. B*, 23(3):529–534, 2006.

[50] N. Lazarides, M. Eleftheriou, and G. P. Tsironis. Discrete breathers in nonlinear magnetic metamaterials. *Phys. Rev. Lett.*, 97(15):157406, 2006.

[51] C. M. Soukoulis, editor. *Photonic Crystals and Light Localization in the 21st Century.* Springer, 2001.

[52] W. M. Robertson and M. S. May. Surface electromagnetic wave excitation on one-dimensional photonic band-gap arrays. *Appl. Phys. Lett.*, 74(13):1800–1802, 1999.

[53] J. M. Elson and P. Tran. Coupled-mode calculation with the r-matrix propagator for the dispersion of surface waves on a truncated photonic crystal. *Phys. Rev. B*, 54(3):1711–1715, Jul 1996.

[54] F. Ramos-Mendieta and P. Halevi. Surface electromagnetic waves in two-dimensional photonic crystals: Effect of the position of the surface plane. *Phys. Rev. B*, 59(23):15112–15120, Jun 1999.

[55] W. M. Robertson, G Arjavalingam, R. D. Meade, K. D. Brommer, A. M. Rappe, and J. D. Joannopoulos. Observation of surface photons on periodic dielectric arrays. *Opt. Lett.*, 18(7):528–530, 1993.

[56] Y. A. Vlasov, N. Moll, and S. J. McNab. Observation of surface states in a truncated photoniccrystal slab. *Opt. Lett.*, 29(18):2175–2177, 2004.

[57] R. Moussa, S. Foteinopoulou, Lei Zhang, G. Tuttle, K. Guven, E. Ozbay, and C. M. Soukoulis. Negative refraction and superlens behavior in a two-dimensional photonic crystal. *Phys. Rev. B*, 71(8):085106, 2005.

[58] P. Kramper, M. Agio, C. M. Soukoulis, A. Birner, F. Müller, R. B. Wehrspohn, U. Gösele, and V. Sandoghdar. Highly directional emission from photonic crystal waveguides of subwavelength width. *Phys. Rev. Lett.*, 92(11):113903, Mar 2004.

[59] E. Moreno, F. J. García-Vidal, and L. Martín-Moreno. Enhanced transmission and beaming of light via photonic crystal surface modes. *Phys. Rev. B*, 69(12):121402, Mar 2004.

[60] I. Bulu, H. Caglayan, and E. Ozbay. Beaming of light and enhanced transmission via surface modes of photonic crystals. *Opt. Lett.*, 30(22):3078–3080, 2005.

[61] K. M. Ho, C. T. Chan, and C. M. Soukoulis. Existence of a photonic gap in periodic dielectric structures. *Phys. Rev. Lett.*, 65(25):3152–3155, Dec 1990.

[62] F. Ramos-Mendieta and P. Halevi. Surface modes in a 2d array of square dielectric cylinders. *Solid State Commun.*, 100(5):311 – 314, 1996.

[63] B. Wang, W. Dai, A. Fang, L. Zhang, G. Tuttle, T. Koschny, and C. M. Soukoulis. Surface waves in photonic crystal slabs. *Phys. Rev B*, 74(19):195104, 2006.

[64] H. Raether. *Surface Plasmons on Smooth and Rough Surfaces and on Gratings*. Springer, 1988.

[65] R. Moussa, B. Wang, G. Tuttle, Th. Koschny, and C. M. Soukoulis. Effect of beaming and enhanced transmission in photonic crystals. *Phys. Rev. B*, 76(23):235417, 2007.

[66] E. Moreno, L. Martn-Moreno, and F.J. Garca-Vidal. Efficient coupling of light into and out of a photonic crystal waveguide via surface modes. *Photonics Nanostruct. Fundam. Appl.*, 2(2):97 – 102, 2004.

[67] Steven K. Morrison and Yuri S. Kivshar. Engineering of directional emission from photonic-crystal waveguides. *Appl. Phys. Lett.*, 86(8):081110, 2005.

[68] A. I. Rahachou and I. V. Zozoulenko. Light propagation in finite and infinite photonic crystals: The recursive green's function technique. *Phys. Rev. B*, 72(15):155117, Oct 2005.

[69] A. Mekis and J. D. Joannopoulos. Tapered couplers for efficient interfacing between dielectric and photonic crystal waveguides. *J. Lightwave Technol.*, 19(6):861, 2001.

[70] D. Tang, L. Chen, and W. Ding. Efficient beaming from photonic crystal waveguides via self-collimation effect. *Appl. Phys. Lett.*, 89(13):131120, 2006.

[71] J. Bauer and S. John. Molding light flow from photonic band gap circuits to microstructured fibers. *Appl. Phys. Lett.*, 90(26):261111, 2007.

[72] K. Guven and E. Ozbay. Directivity enhancement and deflection of the beam emitted from a photonic crystal waveguide via defect coupling. *Opt. Express*, 15(23):14973–14978, 2007.

[73] T. W. Ebbesen, H. J. Lezec, T. Thio H. F. Ghaemi1, and P. A. Wolff. Extraordinary optical transmission through sub-wavelength hole arrays. *Nature*, 391:667–669, 1998.

[74] L. Martín-Moreno, F. J. García-Vidal, H. J. Lezec, K. M. Pellerin, T. Thio, J. B. Pendry, and T. W. Ebbesen. Theory of extraordinary optical transmission through subwavelength hole arrays. *Phys. Rev. Lett.*, 86(6):1114–1117, Feb 2001.

[75] L. Martín-Moreno, F. J. García-Vidal, H. J. Lezec, A. Degiron, and T. W. Ebbesen. Theory of highly directional emission from a single subwavelength aperture surrounded by surface corrugations. *Phys. Rev. Lett.*, 90(16):167401, Apr 2003.

[76] H. J. Lezec, A. Degiron, E. Devaux, R. A. Linke, L. Martin-Moreno, F. J. Garcia-Vidal, and T. W. Ebbesen. Beaming Light from a Subwavelength Aperture. *Science*, 297(5582):820–822, 2002.

[77] R. Sambles. Photonics: More than transparent. *Nature*, 391:641–642, 1998.

[78] S. I. Bozhevolnyi, J. Erland, K. Leosson, P. M. W. Skovgaard, and J. M. Hvam. Waveguiding in surface plasmon polariton band gap structures. *Phys. Rev. Lett.*, 86(14):3008–3011, Apr 2001.

[79] C. Genet and T. W. Ebbesen. Light in tiny holes. *Nature*, 445:39–46, 2007.

[80] J. P. Berenger. A perfectly matched layer for the absorption of electromagnetic waves. *J. Comput. Phys.*, 114(2):185 – 200, 1994.

[81] J.-P. Berenger. Perfectly matched layer for the fdtd solution of wave-structure interaction problems. *IEEE Trans. Antennas Propag.*, 44(1):110–117, Jan 1996.

[82] W. Dai, B. Wang, Th. Koschny, and C. M. Soukoulis. Experimental verification of quantized conductance for microwave frequencies in photonic crystal waveguides. *Phys. Rev. B*, 78(7):073109, 2008.

[83] R. Landauer. Spatial variation of currents and fields due to localized scatterers in metallic conduction. *IBM, J. Res. Dev.*, 1(3):223, 1957.

[84] R. Landauer. Can a length of perfect conductor have a resistance? *Phys. Lett. A*, 85(2):91 – 93, 1981.

[85] E. N. Economou and C. M. Soukoulis. Static conductance and scaling theory of localization in one dimension. *Phys. Rev. Lett.*, 46(9):618–621, Mar 1981.

[86] R. Landauer. Spatial variation of currents and fields due to localized scatterers in metallic conduction. *IBM, J. Res. Dev.*, 32(3):306, 1988.

[87] A. D. Stone and A. Szafer. What is measured when you measure a resistance?the landauer formula revisited. *IBM, J. Res. Dev.*, 32(3):384, 1988.

[88] G. Timp, A. M. Chang, P. Mankiewich, R. Behringer, J. E. Cunningham, T. Y. Chang, and R. E. Howard. Quantum transport in an electron-wave guide. *Phys. Rev. Lett.*, 59(6):732–735, Aug 1987.

[89] B. J. van Wees, H. van Houten, C. W. J. Beenakker, J. G. Williamson, L. P. Kouwenhoven, D. van der Marel, and C. T. Foxon. Quantized conductance of point contacts in a two-dimensional electron gas. *Phys. Rev. Lett.*, 60(9):848–850, Feb 1988.

[90] B. J. van Wees, L. P. Kouwenhoven, E. M. M. Willems, C. J. P. M. Harmans, J. E. Mooij, H. van Houten, C. W. J. Beenakker, J. G. Williamson, and C. T. Foxon. Quantum ballistic and adiabatic electron transport studied with quantum point contacts. *Phys. Rev. B*, 43(15):12431–12453, May 1991.

[91] D. S. Fisher and P. A. Lee. Relation between conductivity and transmission matrix. *Phys. Rev. B*, 23(12):6851–6854, Jun 1981.

[92] M. Büttiker, Y. Imry, R. Landauer, and S. Pinhas. Generalized many-channel conductance formula with application to small rings. *Phys. Rev. B*, 31(10):6207–6215, May 1985.

[93] E. A. Montie, E. C. Cosman, G. W. 't Hooft, M. B. van der Mark, and C. W. J. Beenakker. Observation of the optical analogue of quantized conductance of a point contact. *Nature*, 350:594–595, 1991.

[94] S. Albaladejo, J. J. Sáenz, M. Lester, L. S. Froufe-Pérez, and A. García-Martín. Optical conductance of waveguides built into finite photonic crystals. *Appl. Phys. Lett.*, 91(6):061107, 2007.

[95] L. C. Botten, A. A. Asatryan, N. A. Nicorovici, R. C. McPhedran, and C. Martijn de Sterke. Generalisation of the transfer matrix formulation of the theory of electron and photon conductance. *Physica B: Condens. Matter*, 394(2):320 – 324, 2007.

[96] I. V. Shadrivov, S. K. Morrison, and Y. S. Kivshar. Tunable split-ring resonators for nonlinear negative-index metamaterials. *Opt. Express*, 14(20):9344–9349, 2006.

[97] D. A. Powell, I. V. Shadrivov, Y. S. Kivshar, and M. V. Gorkunov. Self-tuning mechanisms of nonlinear split-ring resonators. *Appl. Phys. Lett.*, 91(14):144107, 2007.

[98] GIL I., BONACHE J., GARCIA-GARCIA J., and MARTIN F. Tunable metamaterial transmission lines based on varactor-loaded split-ring resonators. *IEEE Trans. Microwave Theory Tech.*, 54(11):2665–2674, 2007.

[99] D. A. Powell, I. V. Shadrivov, and Y. S. Kivshar. Multistability in nonlinear left-handed transmission lines. *Appl. Phys. Lett.*, 92(26):264104, 2008.

[100] E. Ozbay, K. Aydin, S. Butun, K. Kolodziejak, and D. Pawlak. Ferroelectric based tuneable srr based metamaterial for microwave applications. *Microwave Conference, 2007. European*, pages 497–499, Oct. 2007.

[101] A. Degiron, J. J. Mock, and D. R. Smith. Modulating and tuning the response of metamaterials at the unit cell level. *Opt. Express*, 15(3):1115–1127, 2007.

[102] L. Kang, Q. Zhao, H. Zhao, and J. Zhou. Magnetically tunable negative permeability metamaterial composed by split ring resonators and ferrite rods. *Opt. Express*, 16(12):8825–8834, 2008.

[103] D. Wang, L. Ran, H. Chen, M. Mu, J. A. Kong, and B. Wu. Active left-handed material collaborated with microwave varactors. *Appl. Phys. Lett.*, 91(16):164101, 2007.

[104] J. Carbonell, V. E. Boria, and D. Lippens. Nonlinear effects in split ring resonators loaded with heterostructure barrier varactors. *Microwave Opt. Technology Lett.*, 50(2):474–479, 2007.

[105] K. Aydin and E. Ozbay. Capacitor-loaded split ring resonators as tunable metamaterial components. *J. Appl. Phys.*, 101(2):024911, 2007.

[106] L. D. Landau and E. M. Lifshitz. *Course of Theoretical Physics: Mechanics*. Butterworth-Heinemann; 3rd edition, 1982.

[107] I. V. Lindell, A. H. Sihvola, S. A. Tretyakov, and A. J. Viitanen. *Electromagnetic Waves in Chiral and Bi-isotropic Media*. Artech House, 1994.

[108] J. Applequist. Optical activity: Biots bequest. *American Scientist*, 75(1):58–68, 1987.

[109] L. D. Barron. *Molecular Light Scattering and Optical Activity*. Cambridge, 1982.

[110] A. Serdyukov, I. Semchenko, S. Tretyakov, and A. Sihvola. *Electromagnetics of Bi-anisotropic Materials: Theory and Applications*. Gordon and Breach Science, 2001.

[111] S. Tretyakov, I. Nefedov, A. Sihvola, S. Maslovski, and C. Simovski. Waves and energy in chiral nihility. *J. Electromagn. Waves Appl.*, 17(5):695–706, 2003.

[112] D. R. Smith, S. Schultz, P. Markoš, and C. M. Soukoulis. Determination of effective permittivity and permeability of metamaterials from reflection and transmission coefficients. *Phys. Rev. B*, 65(19):195104, Apr 2002.

[113] D. R. Smith, D. C. Vier, T. Koschny, and C. M. Soukoulis. Electromagnetic parameter retrieval from inhomogeneous metamaterials. *Phys. Rev. E*, 71(3):036617, 2005.

[114] T. Koschny, P. Markoš, E. N. Economou, D. R. Smith, D. C. Vier, and C. M. Soukoulis. Impact of inherent periodic structure on effective medium description of left-handed and related metamaterials. *Phys. Rev. B*, 71(24):245105, Jun 2005.

[115] D. Kwon, D. H. Werner, A. V. Kildishev, and V. M. Shalaev. Material parameter retrieval procedure for general bi-isotropic metamaterials and its application to optical chiral negative-index metamaterial design. *Opt. Express*, 16(16):11822–11829, 2008.

[116] M C K Wiltshire, J B Pendry, and J V Hajnal. Chiral swiss rolls show a negative refractive index. *J. Phys.: Condens. Matter*, 21(29):292201 (5pp), 2009.

[117] C. Monzon and D. W. Forester. Negative refraction and focusing of circularly polarized waves in optically active media. *Phys. Rev. Lett.*, 95(12):123904, 2005.

[118] Semchenko, I. V., Khakhomov, S. A., and Tretyakov, S. A. Chiral metamaterial with unit negative refraction index. *Eur. Phys. J. Appl. Phys.*, 46:20607, 2008.

[119] Q. Cheng and T. J. Cui. Negative refractions in uniaxially anisotropic chiral media. *Phy. Rev. B*, 73(11):113104, 2006.

[120] C. Zhang and T. J. Cui. Negative reflections of electromagnetic waves in a strong chiral medium. *Appl. Phys. Lett.*, 91(19):194101, 2007.

[121] Y. Tamayama, T. Nakanishi, K. Sugiyama, and M. Kitano. An invisible medium for circularly polarized electromagnetic waves. *Opt. Express*, 16(25):20869–20875, 2008.

[122] C. Qiu, H. Yao, L. Li, S. Zouhdi, and T. Yeo. Backward waves in magnetoelectrically chiral media: Propagation, impedance, and negative refraction. *Phys. Rev. B*, 75(15):155120, 2007.

[123] C. Qiu, H. Yao, L. Li, S. Zouhdi, and T. Yeo. Routes to left-handed materials by magnetoelectric couplings. *Phys. Rev. B*, 75(24):245214, 2007.

[124] A. Papakostas, A. Potts, D. M. Bagnall, S. L. Prosvirnin, H. J. Coles, and N. I. Zheludev. Optical manifestations of planar chirality. *Phys. Rev. Lett.*, 90(10):107404, 2003.

[125] A. V. Rogacheva, V. A. Fedotov, A. S. Schwanecke, and N. I. Zheludev. Giant gyrotropy due to electromagnetic-field coupling in a bilayered chiral structure. *Phys. Rev. Lett.*, 97(17):177401, 2006.

[126] B. Bai, Y. Svirko, J. Turunen, and T. Vallius. Optical activity in planar chiral metamaterials: Theoretical study. *Phys. Rev. A*, 76(2):023811, 2007.

[127] M. Kuwata-Gonokami, N. Saito, Y. Ino, M. Kauranen, K. Jefimovs, T. Vallius, J. Turunen, and Y. Svirko. Giant optical activity in quasi-two-dimensional planar nanostructures. *Phys. Rev. Lett.*, 95(22):227401, 2005.

[128] D. Kwon, P. L. Werner, and D. H. Werner. Optical planar chiral metamaterial designs for strong circular dichroism and polarization rotation. *Opt. Express*, 16(16):11802–11807, 2008.

[129] J. Zhou, L. Zhang, G. Tuttle, T. Koschny, and C. M. Soukoulis. Negative index materials using simple short wire pairs. *Phys. Rev. B*, 73(4):041101, 2006.

[130] B. Wang, J. Zhou, T. Koschny, and C. M. Soukoulis. Nonplanar chiral metamaterials with negative index. *Appl. Phys. Lett.*, 94(15):151112, 2009.

[131] J. D. Baena, L. Jelinek, and R. Marqués. Towards a systematic design of isotropic bulk magnetic metamaterials using the cubic point groups of symmetry. *Phys. Rev B*, 76(24):245115, 2007.

[132] R. Marqués, L. Jelinek, and F. Mesa. Negative refraction from balanced quasi-planar chiral inclusions. *Microwave Opt. Technology Lett.*, 49(10):2606–2609, 2007.

[133] J. Zhou, T. Koschny, and C. M. Soukoulis. An efficient way to reduce losses of left-handed metamaterials. *Opt. Express*, 16(15):11147–11152, 2008.

[134] M. Wegener, J. L. García-Pomar, C. M. Soukoulis, N. Meinzer, M. Ruther, and S. Linden. Toy model for plasmonic metamaterial resonances coupled to two-level system gain. *Opt. Express*, 16(24):19785–19798, 2008.

[135] N. I. Landy, S. Sajuyigbe, J. J. Mock, D. R. Smith, and W. J. Padilla. Perfect metamaterial absorber. *Phys. Rev. Lett.*, 100(20):207402, 2008.

[136] H. Tao, N. I. Landy, C. M. Bingham, X. Zhang, R. D. Averitt, and W. J. Padilla. A metamaterial absorber for the terahertz regime: design, fabrication and characterization. *Opt. Express*, 16(10):7181–7188, 2008.

[137] H. Tao, C. M. Bingham, A. C. Strikwerda, D. Pilon, D. Shrekenhamer, N. I. Landy, K. Fan, X. Zhang, W. J. Padilla, and R. D. Averitt. Highly flexible wide angle of incidence terahertz metamaterial absorber: Design, fabrication, and characterization. *Phys. Rev. B*, 78(24):241103, 2008.

[138] Y. Avitzour, Y. A. Urzhumov, and G. Shvets. Wide-angle infrared absorber based on a negative-index plasmonic metamaterial. *Phys. Rev. B*, 79(4):045131, 2009.

[139] M. Diem, T. Koschny, and C. M. Soukoulis. Wide-angle perfect absorber/thermal emitter in the terahertz regime. *Phys. Rev. B*, 79(3):033101, 2009.

[140] B. Wang, T. Koschny, and C. M. Soukoulis. Wide-angle and polarization-independent chiral metamaterial absorber. *Phys. Rev. B*, 80(3):033108, 2009.

[141] D. L. Jaggard and N. Engheta. Chiralsorb as an invisible medium. *Electronics Lett.*, 25:173, 1989.

[142] J. Monzon. Comment on "chiralsorb as an invisible medium". *Electronics Lett.*, 25:1060, 1989.

[143] C. F. Bohren, R. Luebbers, H. S. Langdon, and F. Hunsberger. Microwave absorbing chiral composites: Is chirality essential or accidental? *Appl. Opt.*, 31(30):6403, 1992.

[144] J. H. Cloete, M. Bingle, and D. B. Davidson. The role of chirality and resonance in synthetic microwave absorbers. *Int. J. Electron. Commun.*, 55(4):233, 2001.